이학박사학위논문

Interannual Variability of Sea Level and Decadal Change of Meridional Overturning Circulation in the East Sea

동해 해수면의 경년 변동성과 자오면 순환의 십여 년 변화

2020년 8월

서울대학교 대학원
지구환경과학부
한 명 희

A Dissertation for the degree of Ph.D.

Interannual Variability of Sea Level and Decadal Change of Meridional Overturning Circulation in the East Sea

August 2020

School of Earth and Environmental Sciences
The Graduate School
Seoul National University

MyeongHee Han

Interannual Variability of Sea Level and Decadal Change of Meridional Overturning Circulation in the East Sea

지도교수 조 양 기

이 논문을 이학박사 학위논문으로 제출함
2020년 8월

서울대학교 대학원
지구환경과학부
한 명 희

한명희의 이학박사 학위논문을 인준함
2020년 8월

위 원 장 ______ 남 성 현 ______ (인)
부위원장 ______ 조 양 기 ______ (인)
위 원 ______ 나 한 나 ______ (인)
위 원 ______ 강 현 우 ______ (인)
위 원 ______ 박 재 훈 ______ (인)

Interannual Variability of Sea Level and Decadal Change of Meridional Overturning Circulation in the East Sea

A

Ph.D. Dissertation

by

MyeongHee Han

Supervisor: Prof. Yang-Ki Cho

Dissertation Committee:

SungHyun Nam
Committee Chairman
Seoul National University

Yang-Ki Cho
Seoul National University

Hanna Na
Seoul National University

Hyoun-Woo Kang
Korea Institute of Ocean
Science and Technology

Jae-Hun Park
Inha University

August 2020

Abstract

Interannual Variability of Sea Level and Decadal Change of Meridional Overturning Circulation in the East Sea

MyeongHee Han
School of Earth and Environmental Sciences
The Graduate School
Seoul National University

The interannual variability of sea level and decadal change of meridional overturning circulation (MOC) were investigated using satellite altimetry, tide-gauge, and reanalysis data in the East Sea (ES; also referred to as Sea of Japan). There has been growing concern about interannual fluctuations of sea levels to countries around the ES due to the accelerating sea level rise by global warming. Monthly mean sea level is at its maximum and many typhoons pass the ES in summer (August). Meanwhile, the wind stress and the interannual variability of sea level are the highest in winter (November and December).

The MOC plays a vital role in distributing heat, freshwater, and dissolved matter in semienclosed deep marginal seas such as the ES. However, few studies on the ES MOC have been done until now. The objective of this study is to understand the ES MOC with external atmospheric and internal oceanic processes along with interannual sea level variations.

Monthly mean sea levels from tide-gauge observation had annual maxima in the summer (August). The rising rate of the summer (August) ES sea level from satellite altimetry data was larger than that of annual sea level for 26 years (1993-2018) in the ES. The interannual variation of sea levels was dominated by the Ekman transport in the south of the ES which was caused by the atmospheric pressure gradient between Kuroshio Extension (KE) and around Taiwan. The sea level in the ES was higher when the north-northeastward Ekman transport and the atmospheric pressure gradient were strong in the south of the ES, and it was lower when they were weak. The summer sea level in the ES could be estimated using summer ES sea level index which was the difference of atmospheric pressure anomalies between KE and around Taiwan.

The monthly mean wind stress from reanalysis data in the ES had its maximum in December and sea level anomaly from satellite altimetry data in the winter (November and December) had its maximum in 2016 and minimum in 2017 for 26 years (1993-2018). The sea level in the ES could be explained by horizontal water convergence and divergence due to monsoonal wind-induced Ekman transport in the winter. In high sea level years, there were decreased outflow volume transport in the northeast ES and increased inflow volume transport in the southern ES due to increased south-westward Ekman transport linked to enhanced south-eastward wind stress in the southern Okhotsk Sea. In low sea level years, there were increased outflow volume transport in the northeast ES and decreased inflow volume transport in the southern ES due to increased south-westward Ekman transport linked to enhanced south-eastward wind stress in the southern ES. The winter sea level in the ES also could be estimated using winter ES sea level index which was the difference of atmospheric pressure anomalies between the Soya Strait and east of Taiwan because Ekman transport was changed by atmospheric pressure gradient.

There were significant decadal changes in the strength and structure of the ES MOC for 20 years (1993–2012) from two counter-rotating overturning cells in late 1990s to one full-depth anti-cyclonic overturning cell in 2000s in HYCOM reanalysis data. These ES MOC changes made northward shift of southward volume transport in the intermediate layer and southward shift of northward volume transport in the deep abyssal layer from the late 1990s to the 2000s. Two overturning cells were made by shallow convection (subduction) in the northwest ES due to colder sea surface temperature in the late 1990s and one overturning cell was made by deep convection in the farther northwest ES with saltier SSS in the 2000s. The atmospheric buoyancy (heat and freshwater) flux and Ekman transport by atmospheric momentum flux made these shallow and deep convections in the northwest ES along with northward surface flow in the southern ES and westward ocean recirculation in the northern ES.

This study revealed that the interannual variability of sea level and the decadal change of MOC were largely controlled by Ekman transport and atmospheric and oceanic processes in the ES, respectively. Further investigations on the relation between the interannual variability of the ES sea level and the decadal change of the ES MOC are necessary for better understanding of the circulation change in the ES, which might suggest implication for ocean response to climate change as a miniature ocean.

Keyword: East Sea, sea level, ES MOC, Ekman transport, atmospheric pressure gradient, air-sea interaction, interannual variability, decadal change

Student Number : 2001-30274

Table of Contents

List of Figures

List of Tables

1. Introduction

1.1 Background

The East Sea (ES, also referred to as Sea of Japan) is surrounded by Korea, Russia, and Japan and is connected to the East China Sea (ECS), Okhotsk Sea (OS), and the Pacific through narrow straits (Figure 1.1). The surface circulation in the ES is characterized by inflow from the ECS to the ES through the Korea Strait (KS), and outflow from the ES to the Pacific and the OS through the Tsugaru Strait (TS) and Soya Strait (SS), respectively. The deep circulation in the ES is cyclonic in the Ulleung Basin (UB), Japan Basin (JB), and Yamato Basin (YB) (Figure 1.2). The mean wind over the ES in August and December is southerly (Figure 1.3a) and northwesterly (Figure 1.3b). There are several interesting physical characteristics and features to explore and study in the ES such as sea level, circulation, sea surface temperature (SST), sea surface salinity (SSS), surface wave and current, and tide. In this study, interannual variability of sea level and decadal change of meridional overturning circulation (MOC) which have not been revealed, were selected among them.

In contrast to global sea level, the sea level in a marginal sea changes according to the diverse processes such as horizontal mass and volume exchanges, evaporation, precipitation, thermosteric and halosteric effects of sea water properties (Mangiarotti and Lyard, 2008; Pinardi et al., 2014).

The sea level rise and its fluctuation in the ES should be monitored to reduce damages by coastal flooding. Studying on the sea level change and its causes are important not only to people but also to the policy makers in many countries (Noone et al., 2013). The sea level from tide-gauge has a maximum in summer

(August) but its standard deviation from satellite observation has a maximum in winter (November and December). Tropical cyclones, typhoons, pass the ES frequently in the ES and induce high sea level in summer (August). The monthly mean wind stress, which can raise the sea level in the ES, is maximum in winter (December) (Figure 1.3b). The correlations between monthly sea level anomaly in the ES and wind stress anomaly around the ES were significant in summer (August) and winter (November and December). Thus, the effects of the wind stress and atmospheric pressure on the sea level variations in summer (August) and winter (November and December) were studied to reveal the relation between them.

Global MOC, which can be defined by zonally and vertically integrated meridional flows in the ocean, carries an extremely large amount of heat from low- to high-latitude regions, contributing to the overall climate of the Earth (Wunsch, 2002; Stouffer et al., 2006). In contrast to the increased interest in the Atlantic MOC, the Pacific MOC has not attracted significant attention, as it features from near-unventilated surface waters to a deep and abyssal layer, e.g., low dissolved oxygen at 1,000 m (Talley et al., 2006). However, previous studies have suggested that the ventilation is very active in the ES, which yield the highest deep dissolved oxygen in the Pacific, including the South Pacific (e.g., Kim et al., 2004; Talley et al., 2006; Yoon et al., 2018). Also, there were few studies about the ES MOC compared to many studies about surface and intermediate layer circulations in the ES. Thus, the ES MOC to understand the change of the horizontal and vertical circulations should be studied.

In chapters 2 and 3, the dynamics of sea level changes caused by atmospheric pressure and wind stress are investigated in summer and winter, respectively. In chapter 4, the mechanism of ES MOC with boundary conditions driven by atmospheric and oceanic processes is studied. Discussion is in chapter 5, and summary and conclusion follow in chapter 6.

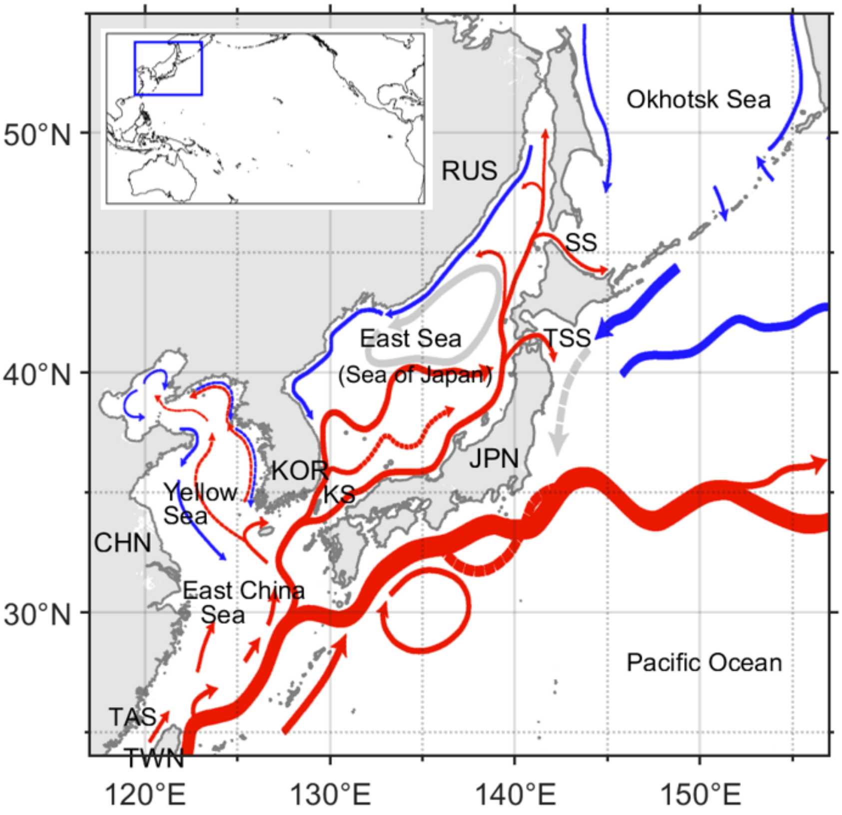

Figure 1.1 Schematics of the regional circulation patterns, with major surface (red or blue) and intermediate (gray) currents transporting warm (red) and cold (blue) waters in the northeast Asian marginal seas or northwest Pacific Ocean (available from http://www.khoa.go.kr). The stronger currents are shown with thicker arrows, while continuous and continual currents are indicated by solid and dashed arrows, respectively. KOR, RUS, CHN, TWN, and JPN are the abbreviations for Korea, Russia, China, Taiwan, and Japan, respectively. KS, TAS, TSS, and SS are the Korea/Tsushima Strait, Taiwan Strait, Tsugaru Strait, and Soya Straits, respectively.

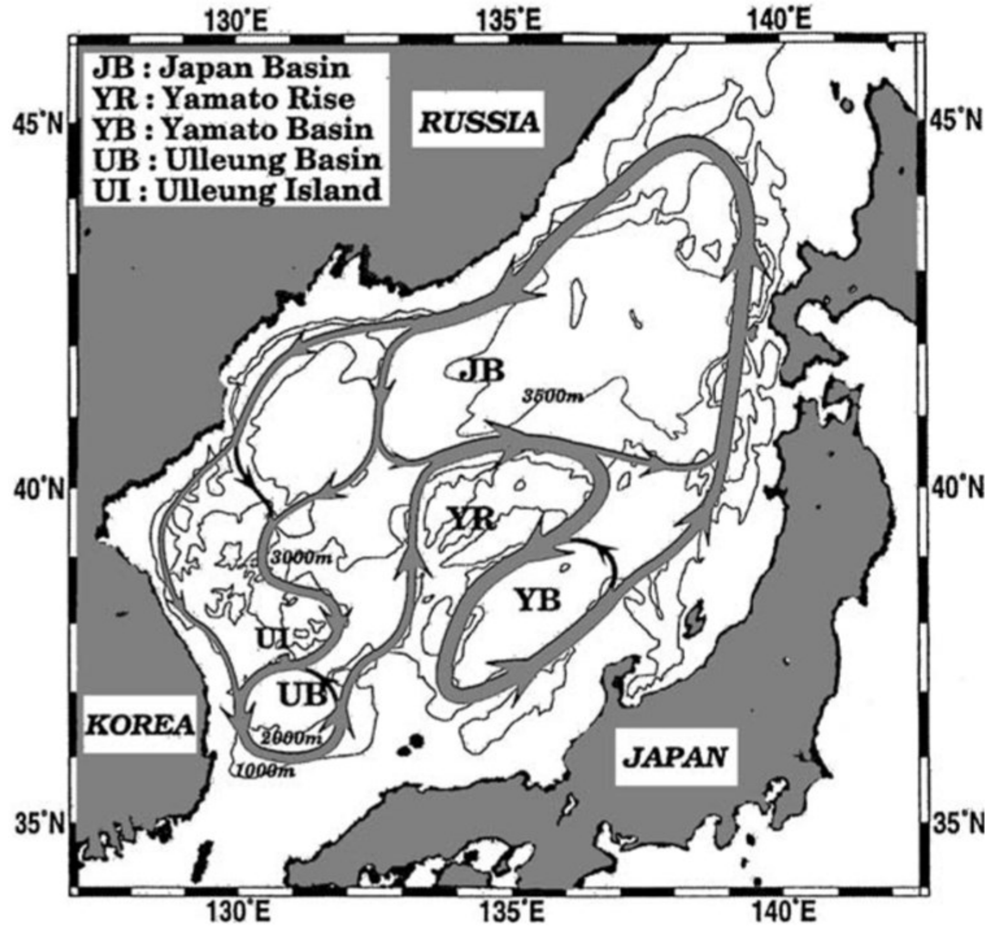

Figure 1.2 Schematics of the abyssal circulation in the ES deduced from the distribution of the mean flow vectors (Figure 12 of Senjyu et al. (2005)).

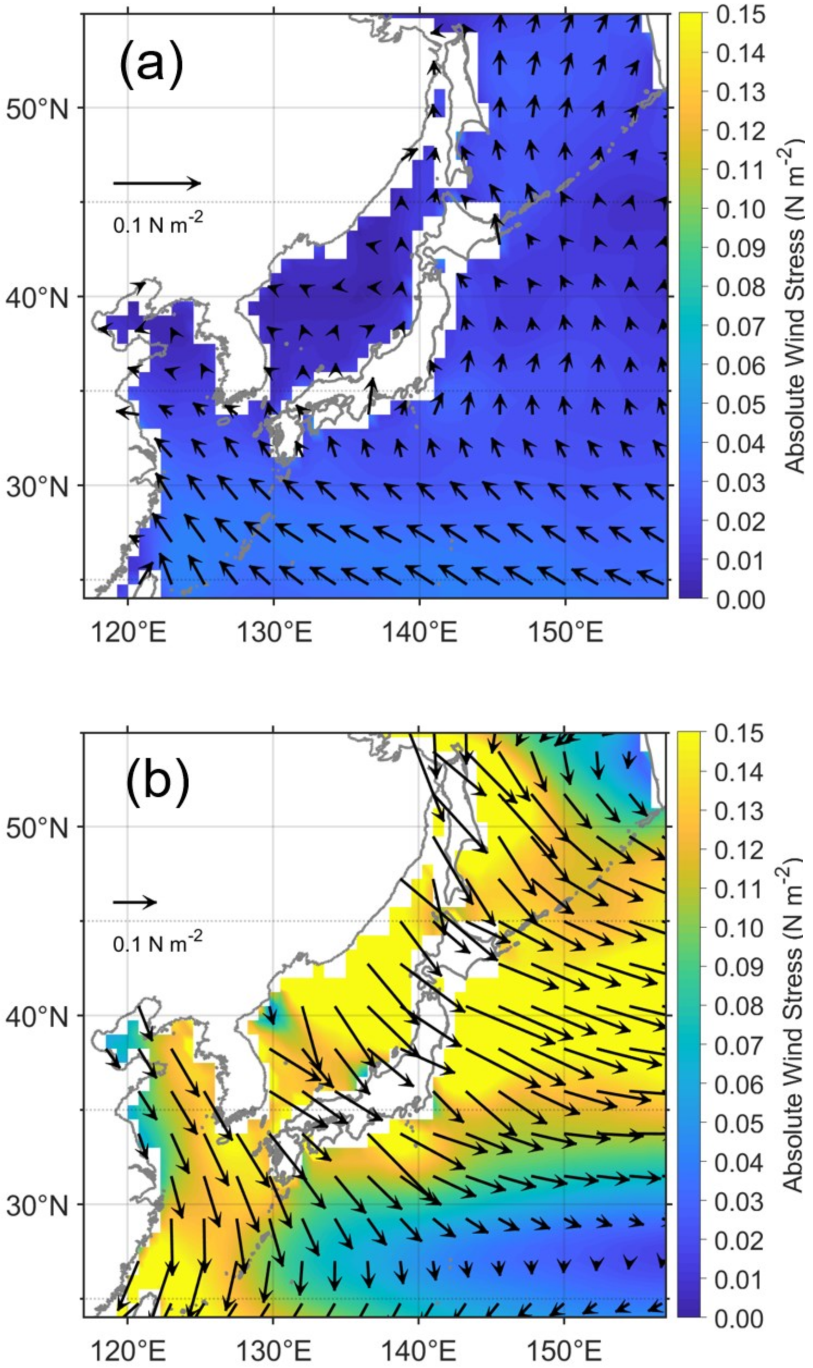

Figure 1.3 Mean surface wind stress (black vector) with absolute surface wind stress (color) in (a) August and (b) December from 1993 to 2018 (ECMWF). Coastlines are drawn in gray. Note that vector sizes in (a) and (b) are different and color scales are same.

2.1 Purpose of this study

The purpose of this study is to investigate the interannual variability of sea level changes in the ES according to surface wind stress and mean sea level atmospheric pressure in summer and winter, and the decadal change of ES MOC driven by oceanic process and atmospheric heat, freshwater, buoyancy, and momentum fluxes in the ES.

2. Summer sea level

2.1. introduction

The water exchanges between the ES and the Pacific Ocean are forced by atmospheric disturbances and are constrained by bathymetric features like narrow and shallow KS, TS, and SS (Figure 1.1 and Figure 2.1), whereas the sea level in the ES can be rather homogeneous via rapidly propagating barotropic waves (Lyu et al., 2002; Nam et al., 2004; Lyu and Kim, 2005). The volume transport through the KS is highly correlated with atmospheric pressure, along-strait wind stress, and sea level differences between the Pacific Ocean and ES for periods longer than 100 days (Lyu and Kim, 2005). Choi et al. (2009) examined the relationship between the zonal wind stresses in the south-western ES and the meridional migration of a sub-polar front within the ES; surface wind stress has also been suggested by other studies as one of the most important contributors to sea level changes in marginal seas (Zuo et al., 2012; Zhang et al., 2014; Yu et al., 2019). The interannual variations of volume transport through the SS were reportedly linked to the surface wind stresses along the east coast of Sakhalin (Ohshima et al., 2017).

Sea levels observed at tidal stations in the ES have a large seasonal variation and maximum in summer (August), averaged from 1993 to 2018 (Figure 2.2). The rising rate of summer (August) ES sea level from satellite altimetry data from 1993 to 2018 (4.5 mm/year, black dotted line in Figure 2.3) is larger than those of annual ES sea level (3.7 mm/year, red dashed line in Figure 2.3) and annual global sea level (3.4 mm/year, Baude et al. (2019)). Moreover, the effect of typhoons, which induce high sea levels and frequently pass through the ES in summer, needs to be studied. The sea level maxima and their interannual variations in summer need to be understood so that issues such as coastal flooding, saltwater intrusion, and habitat destruction, can be prepared beforehand (Noone et al., 2013). Sea level changes in the ES have been reported, mainly with tide-gauge and altimetry measurements (Marcos et al., 2012), but the causes and dynamics of summer sea level changes in the ES have not been studied.

In chapter 2, the mechanism of the interannual ES sea level variability caused by atmospheric pressure and wind stress in summer is investigated. The data and methods are presented in Section 2.2, and the results and discussion are described in Sections 2.3 and 2.4, respectively. Conclusions are in Section 2.5.

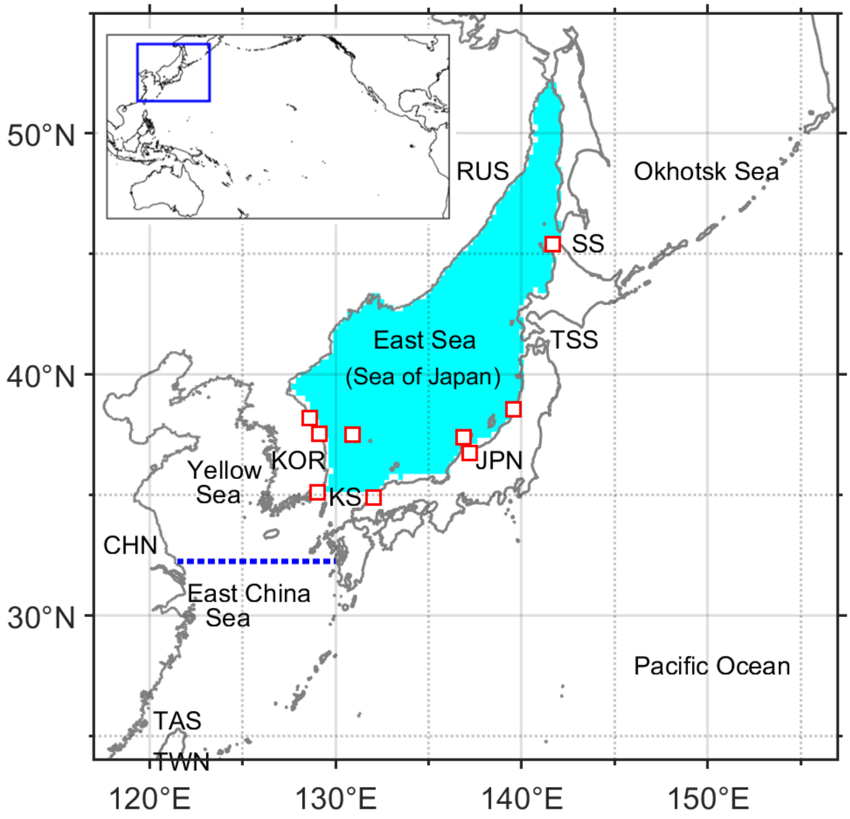

Figure 2.1 Domain of the northwest Pacific Ocean. The East Sea (ES) and locations of nine tide-gauge stations are indicated by cyan color and red open squares (available from https://www.psmsl.org). KOR, CHN, RUS, JPN, and TWN are the abbreviations of Korea, China, Russia, Japan, and Taiwan, respectively, and KS, TAS, TSS, and SS are the Korea/Tsushima Strait, Taiwan Strait, Tsugaru Strait, and Soya Strait, respectively. A zonal line from the east coast of China to the west coast of Japan along 32.25°N is indicated by blue dotted line.

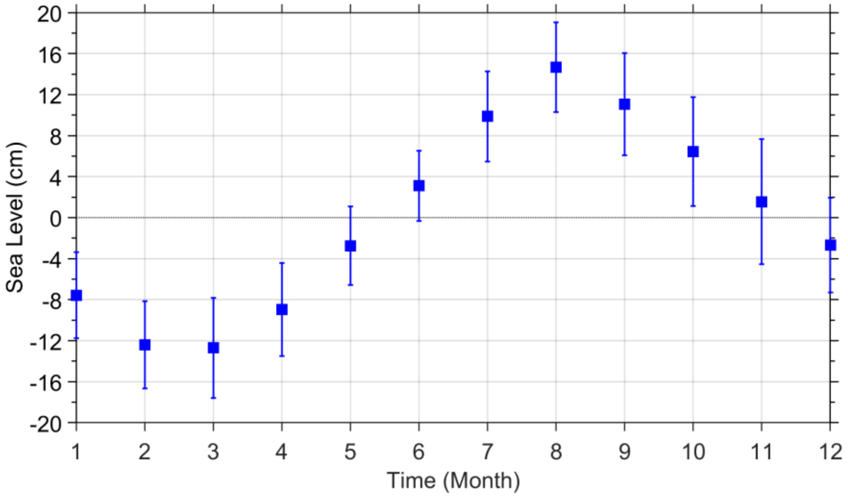

Figure 2.2 De-trended climatology (blue filled squares) of the ES sea levels estimated from nine tide-gauge (Figure 2.1) observations for 26 years (1993–2018).

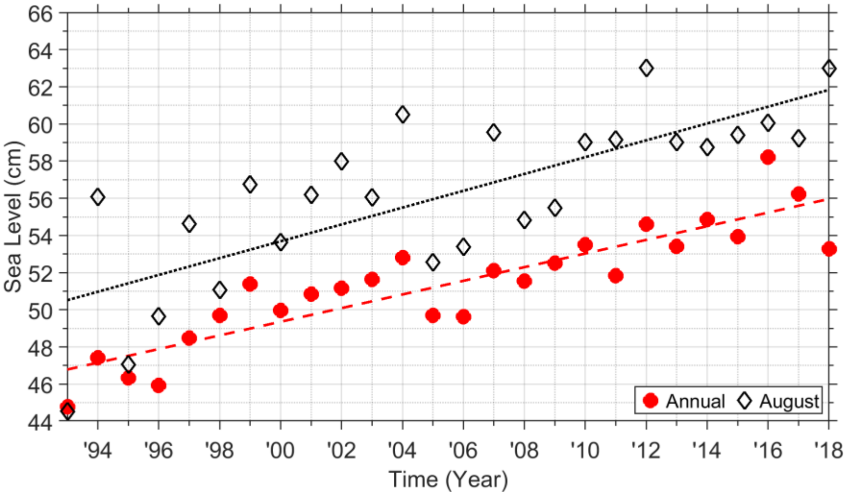

Figure 2.3 Time series of annual (red filled circles) and summer (August, black open diamonds) ES sea levels estimated from satellite altimetry for 26 years (1993–2018).

2.2. Data and Methods

Time series of monthly mean sea levels were made in summer in the ES (cyan in Figure 2.1), which were analyzed for 26 years (1993–2018) for this study. These monthly data were from the daily absolute dynamic topography (ADT) data which were provided by the Copernicus Marine Environment Monitoring Service (CMEMS) and they were gridded with a horizontal resolution of 0.25° from all satellite altimeter missions (Jason-3, Sentinel-3A, HY-2A, Saral/AltiKa, Cryosat-2, Jason-2, Jason-1, TOPEX/Poseidon, ENVISAT, GFO, and ERS1/2). ADT was computed as the sum of sea level anomaly and the mean dynamic topography (MDT, mean sea level driven by thermodynamic processes in the ocean; Rio et al., 2011; CNES-CLS18, 2020). The MDT used in this ADT product is the 1/8° resolution MDT from the Centre National d'Etudes Spatiales-Collect Localisation Satellites 2018 produced using altimetric mean sea surface, (e.g., (Pujol et al., 2018)), Gravity field and steady-state Ocean Circulation Explorer (GOCE) geoid model (Mayer-Guerr and GOCO_Team, 2015; Fecher et al., 2017), and an extended dataset of in situ observations (Park et al., 2019). The level four of ADT data (e.g. dt_global_allsat_phy_l4_20180831_20190101.nc) were downloaded by ftp from the Copernicus CMEMS website (CMEMS_FTP, 2020; Taburet and Pujol, 2020). More information regarding ADT is available at the website for the Copernicus Marine Environment Monitoring Service (CMEMS_portal, 2020). In the ES, there are negligible errors in tidal correction because of the weak (~5 cm) tides, while those for atmospheric correction are up to 10 cm for non-isostatic sea level responses to atmospheric pressure at a period of ~3 days (Lyu et al., 2002; Nam et al., 2004; Lyu and Kim, 2005). Errors for atmospheric correction are also negligible if sea level data are monthly averaged.

There is another satellite observation such as two-sat-merged data and it was compared with all-sat-merged data. Rising rates of monthly sea levels from all-sat-merged and two-sat-merged data are 3.891 mm/year (black diamonds in Figure 2.4) and 3.784 mm/year (red circles in Figure 2.4) from 1993 to 2018, respectively. The mean and standard deviation of monthly sea levels from all-sat-merged and two-sat-merged data are 0.514 ± 0.067 m and 0.518 ± 0.067 m, respectively, yielding a significantly high (1.00, p-value = 0) cross-correlation coefficient. The difference (all-sat-merged and two-sat-merged data) had a time mean and standard deviation of −0.004 and 0.002 m, small enough compared with all-sat-merged and two-sat-merged data, indicating that there was little difference between all-sat-merged and two-sat-merged, and all-sat-merged data would be used from now on.

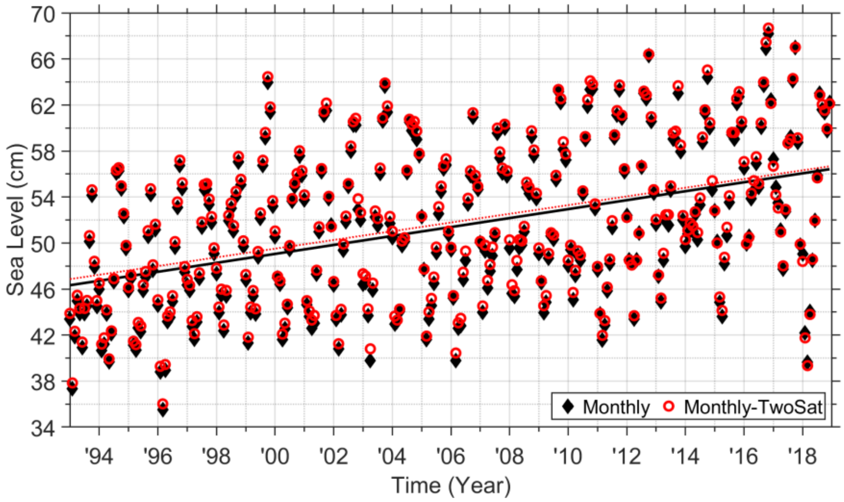

Figure 2.4 Time series of monthly ES sea levels estimated from all-sat (black diamonds) and two-sat (red circles) merged satellite altimetry for 26 years (1993–2018). The black solid and red dotted lines are the trends of monthly ES sea levels estimated from all-sat and two-sat, respectively.

Monthly mean sea level data, at nine tide-gauge stations (red open squares in Figure 2.1), from 1993 to 2018 were provided by the Permanent Service for Mean Sea level (PSMSL) (Holgate et al., 2013; PSMSL, 2020). The sea level data were from stations in Korea (four stations: BUSAN, MUKHO, SOKCHO, and ULLEUNG) and Japan (five stations: HAMADA II, WAJIMA, TOYAMA, NEZUGASEKI, and WAKKANAI). The tide-gauge observations were for validating the satellite data only and the tide-gauge stations only where the vertical displacement of tide-gauge was less than 1.8 cm were selected.

Daily mean sea level atmospheric pressure and wind stress data from the European Centre for Medium-Range Weather Forecasts (ECMWF) interim reanalysis (ERA-Interim) were used for me to form monthly mean gridded sea level atmospheric pressure and wind stress, with a horizontal resolution of 0.75° for 26 years from 1993 to 2018 in the northwest Pacific Ocean (100–180°E, 0–63°N).

The linear trend over the time period (26 years) was removed to investigate the interannual variation. Ekman transport, per unit width, within the surface Ekman layer (VT_{Ekman}, $\mathrm{m^2\ s^{-1}}$) was calculated using Equation (1) :

$$VT_{Ekman} = \int_{D_{Ekman}}^{0} u_{Ekman}\ dz = \int_{D_{Ekman}}^{0} \frac{1}{f\rho}\frac{\partial\tau}{\partial z}dz = \frac{1}{f\rho}\left[\ \tau\ \right]_{D_{Ekman}}^{0}$$

$$= \frac{1}{f\rho}\left\{\ \tau\ (z=0) - \tau\ (z=D_{Ekman})\ \right\} = \frac{\tau\ (z=0)}{f\rho}. \qquad (1)$$

Here, u_{Ekman}, D_{Ekman}, f (= 2Ωsinφ), Ω (≈ 7.2921×10^{-5}), φ, ρ, z, and τ denote the Ekman velocity ($\mathrm{m\ s^{-1}}$), Ekman depth (m), Coriolis parameter ($\mathrm{rad\ s^{-1}}$), rotation rate of the Earth ($\mathrm{rad\ s^{-1}}$), latitude, density of sea water (≈ 1,025 $\mathrm{kg\ m^{-3}}$), depth (m), and wind stress ($\mathrm{N\ m^{-2}}$), respectively.

Sea level changes by Ekman transport (SLC_{Ekman}, m) at each data grid were calculated using Equation (2):

$$SLC_{Ekman} = \mathit{\Delta} VT_{Ekman} \times \frac{LT}{A}. \qquad (2)$$

Here, $\mathit{\Delta} VT_{Ekman}$, L, T, and A denote net incoming Ekman transport, per unit width, within the surface Ekman layer, grid width (0.75°, ECMWF), time (one month in the case of monthly mean ECMWF), and grid area (0.75×0.75°, ECMWF), respectively.

2.3. Results

2.3.1. Long-term trend of sea levels in summer

Mean seasonal variation of nine tide-gauge observations averaged from 1993 to 2018 was examined to check annual variations of actual sea level. Maximum and minimum sea levels were +14.7 cm in summer (August) and -12.7 cm in March, respectively (Figure 2.2). Rising rates of sea levels in summer (August) from satellite altimetry (4.5281 mm/year, black dotted line in Figure 2.3) and tide-gauge observations (4.5279 mm/year, not shown) from 1993 to 2018 were compared. Sea level data from satellite altimetry and from tide-gauge observations, which were independent of each other, had strong positive correlation with coefficients of 0.89 (summer (August), p-value < 0.01) and 0.95 (annual, p-value < 0.01), respectively (not shown). Only satellite altimetry data as sea levels would be used hereafter.

2.3.2. Interannual variation of sea level anomalies

The interannual variations of the summer ES Sea level Anomalies (SESA) were classified as years of relatively high (positive anomalies above +2 cm) and low (negative anomalies below -2 cm) sea levels; Period H (1994, 1999, 2002, 2004, 2007, 2012, and 2018) and Period L (1993, 1995, 1996, 1998, 2005, 2006, and 2008), respectively (Figure 2.5). Selected threshold of 2 cm was the accuracy of TOPEX/Poseidon’s radar altimeter (Cheney et al., 1994). The surface wind stress and sea level atmospheric pressure, between two periods, were analyzed to figure out positive (increasing) and negative (decreasing) effects of atmospheric conditions on SESA.

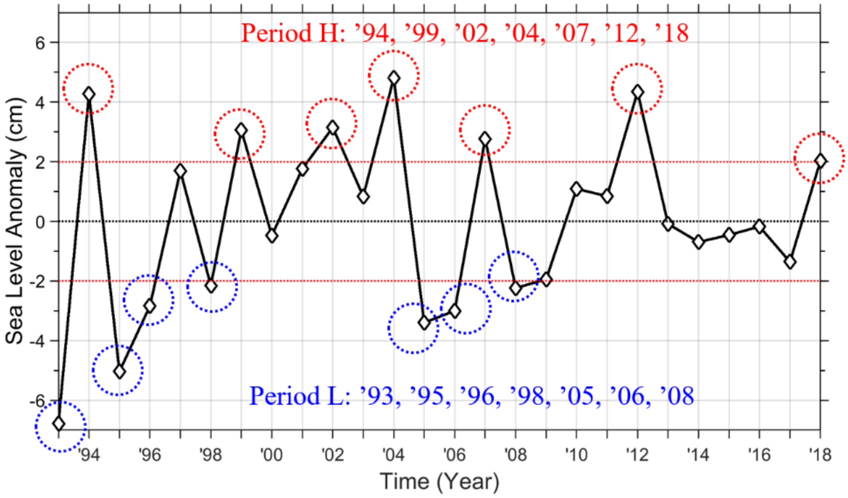

Figure 2.5 Time series of the de-trended summer mean sea level anomalies averaged over the ES from 1993 to 2018. Seven year high (higher than 2 cm) or low (lower than -2 cm) August sea level anomalies are denoted as Period H (1994, 1999, 2002, 2004, 2007, 2012, and 2018) or Period L (1993, 1995, 1996, 1998, 2005, 2006, and 2008) with red and blue circles, respectively.

2.3.3. Ekman transport and sea level anomaly

The ECS is the main path for the Taiwan and Tsushima Warm Currents which are the primary seawater advection sources to the ES (Isobe, 1999). The meridional Ekman transport anomaly in the ECS (from the east coast of China to the west coast of Japan along 32.25°N, a blue dotted line in Figure 2.1) was calculated to examine the relationship between wind stress anomaly in the ECS and SESA. The correlation between meridional Ekman transport anomaly along 32.25°N in summer and SESA, from 1993 to 2018, was significant (correlation coefficient 0.59 with p-value < 0.01, Figure 2.6). Thus, Ekman transport by wind stress in the ECS and sea level in the ES were closely related in summer.

There were strong (weak) west-northwestward wind stresses in the south of the ES for Period H (Period L) around 136°E and 28°N (140°E and 29°N) (Figure 2.7). Ekman transport can be calculated by using Equation (1). More (less) north-northeastward Ekman transport by strong (weak) west-northwestward wind stress brings more (less) seawater from the northwest Pacific Ocean to the ES in Period H (Period L). Sea level anomalies due to the net Ekman transport anomaly were calculated based on Equation (2). Convergence (divergence) of the Ekman transport anomaly in the ES results in a positive (negative) SESA for Period H (Period L) as shown in Figure 2.8a (Figure 2.8b) and it is similar to the observations from the satellite in Figure 2.8c (Figure 2.8d). The positive (negative) result in the ES was due to the north-northeastward (south-southwestward) Ekman transport anomaly caused by wind stress, in the south of the ES, for Period H (Period L) in Figure 2.7. Even though the sea level changes and anomalies of the entire ES were not positive (negative) for Period H (Period L), the averaged sea level anomalies in the ES were positive (negative) (Figure 2.8).

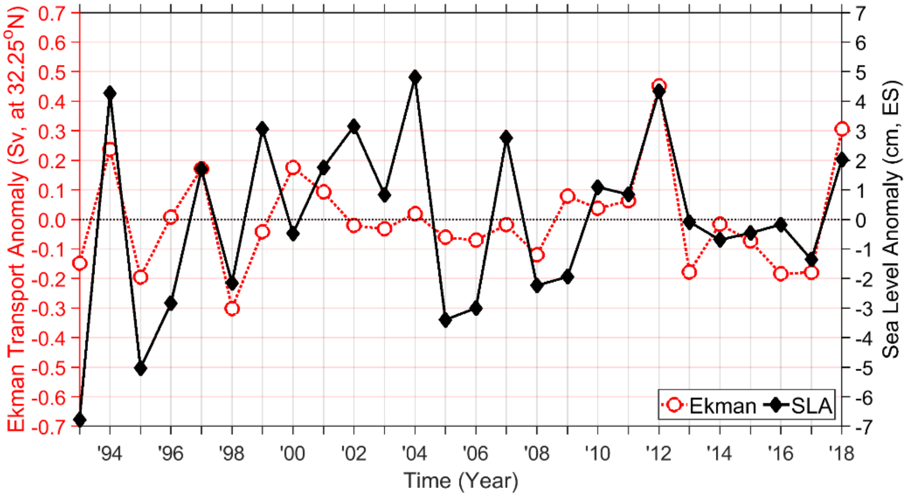

Figure 2.6 Timeseries of meridional Ekman transport anomaly at 32.35°N and sea level anomaly in the ES in summer (1993-2018). The correlation coefficient is 0.59 (p-value < 0.01)

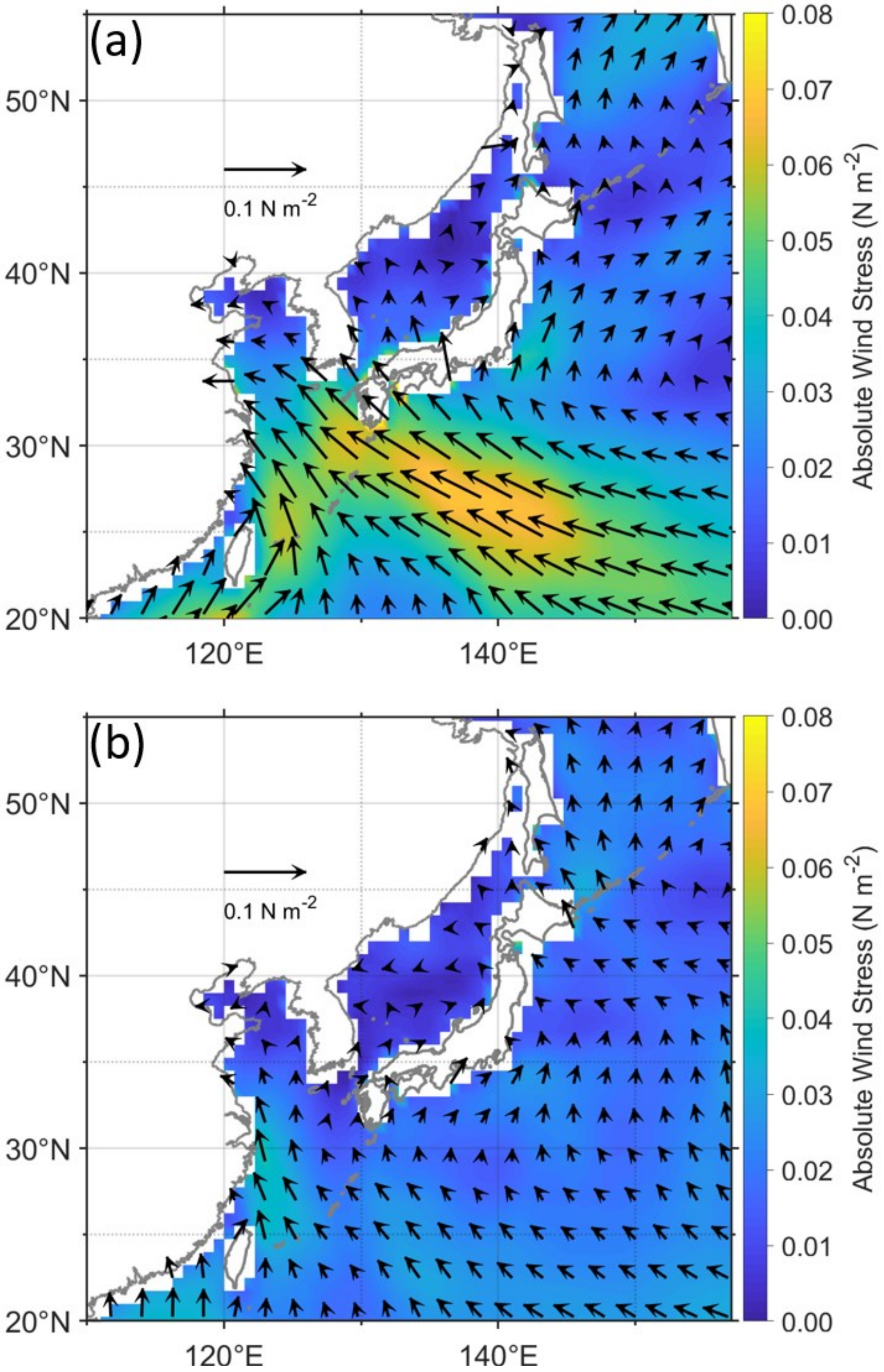

Figure 2.7 Surface wind stress (black vector) with absolute surface wind stress (color) in summer averaged for Periods (a) H and (b) L. There are strong (weak) west-northwestward wind stresses around 136°E and 28°N (140°E and 29°N) in the south of the ES for Period H (Period L). Coastlines are drawn in gray.

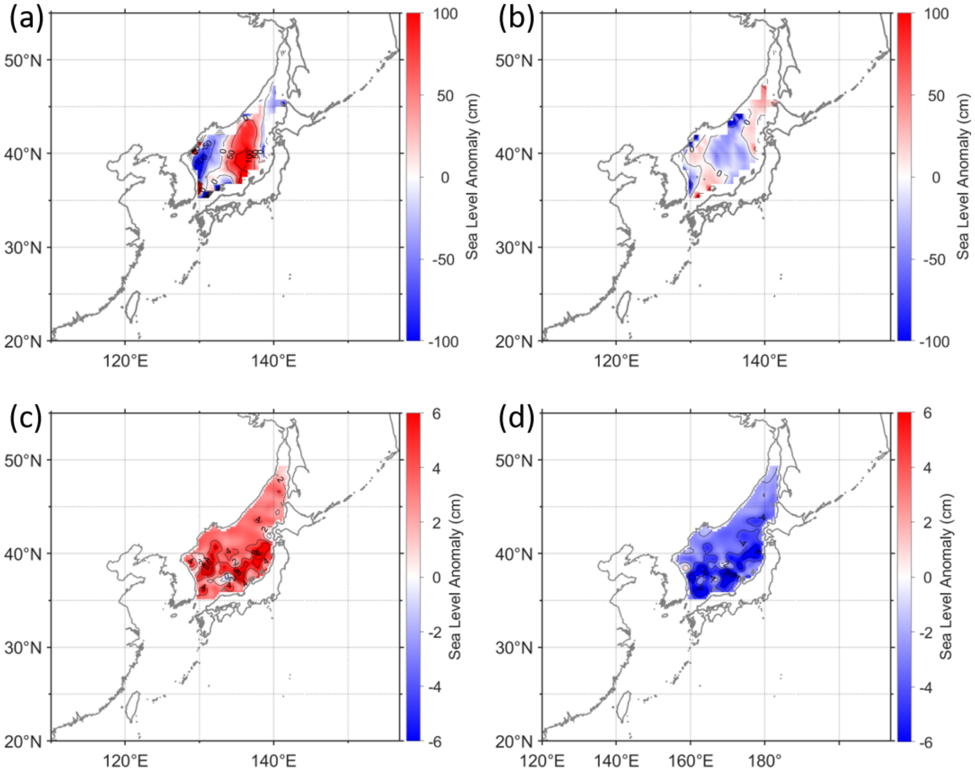

Figure 2.8 Sea level anomaly by net incoming Ekman transport anomaly, calculated by Equation (2), in summer averaged for Periods (a) H and (b) L. The ES sea level changes derived from satellite altimetry observations during Periods (c) H and (d) L.

2.3.4. Atmospheric pressure distribution

Sea levels in Period H (Period L) have large (small) atmospheric pressure gradients with areas of high pressure in Kuroshio Extension (KE) and low pressure around Taiwan in Figure 2.10. Large (small) atmospheric pressure gradients resulted in strong (weak) west-northwestward wind stresses. West-northwestward wind stresses cause north-northwestward Ekman transport from the northwest Pacific Ocean into the ES as shown in Figure 2.8.

Atmospheric pressure anomalies were computed to examine atmospheric contribution to SESA. In Period H (Period L), there were positive and negative (negative and positive) atmospheric pressure anomalies in KE and around Taiwan, respectively in Figure 2.11. This atmospheric pressure anomaly distribution in Period H (Period L) made the west-northwestward (east-southeastward) wind stress anomaly in the south of the ES. Based on these findings, it could be concluded that atmospheric pressure anomalies, positive (negative) in the KE and negative (positive) around Taiwan, caused positive (negative) SESA in Period H (Period L). When the period changes from Period H to Period L (from Period L to Period H), the effect of wind stress on SESA changes from positive to negative (from negative to positive) owing to the changes of atmospheric pressure anomalies.

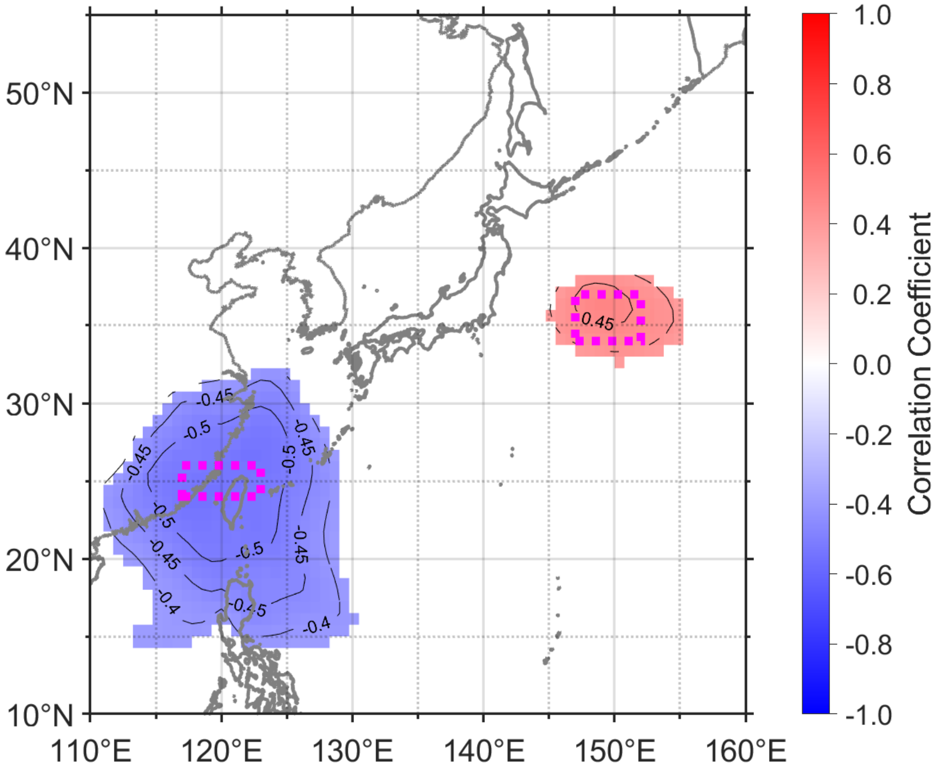

Figure 2.9 Correlation map of the summer ES sea level anomaly with the mean sea level atmospheric pressure anomaly from 1993 to 2018. The contour interval is 0.05 and confidence level of the correlation coefficient less than 95% were discarded. A positive correlation means that a high (low) ES sea level occurs with a high (low) atmospheric pressure anomaly. Here, the areas showing the maximum positive (KE) and minimum negative (around Taiwan) correlation coefficients are marked with magenta dotted boxes.

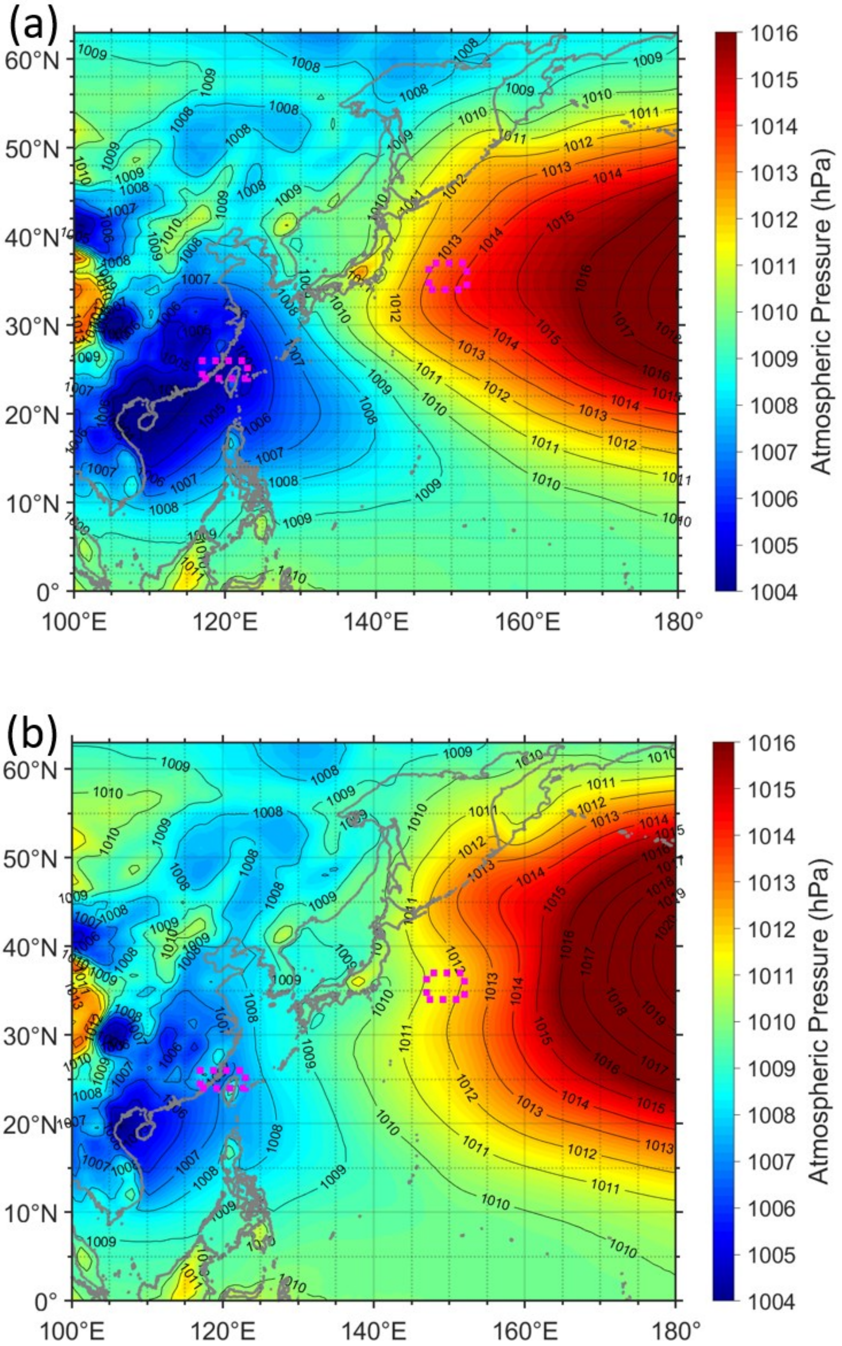

Figure 2.10 Mean sea level atmospheric pressures in summer averaged for the (a) Period H and (b) Period L in the northwest Pacific Ocean (contour interval: 1 hPa, ECMWF). The areas defining the summer ES sea level index (SESI) are denoted by magenta dotted boxes. Coastlines are drawn in gray.

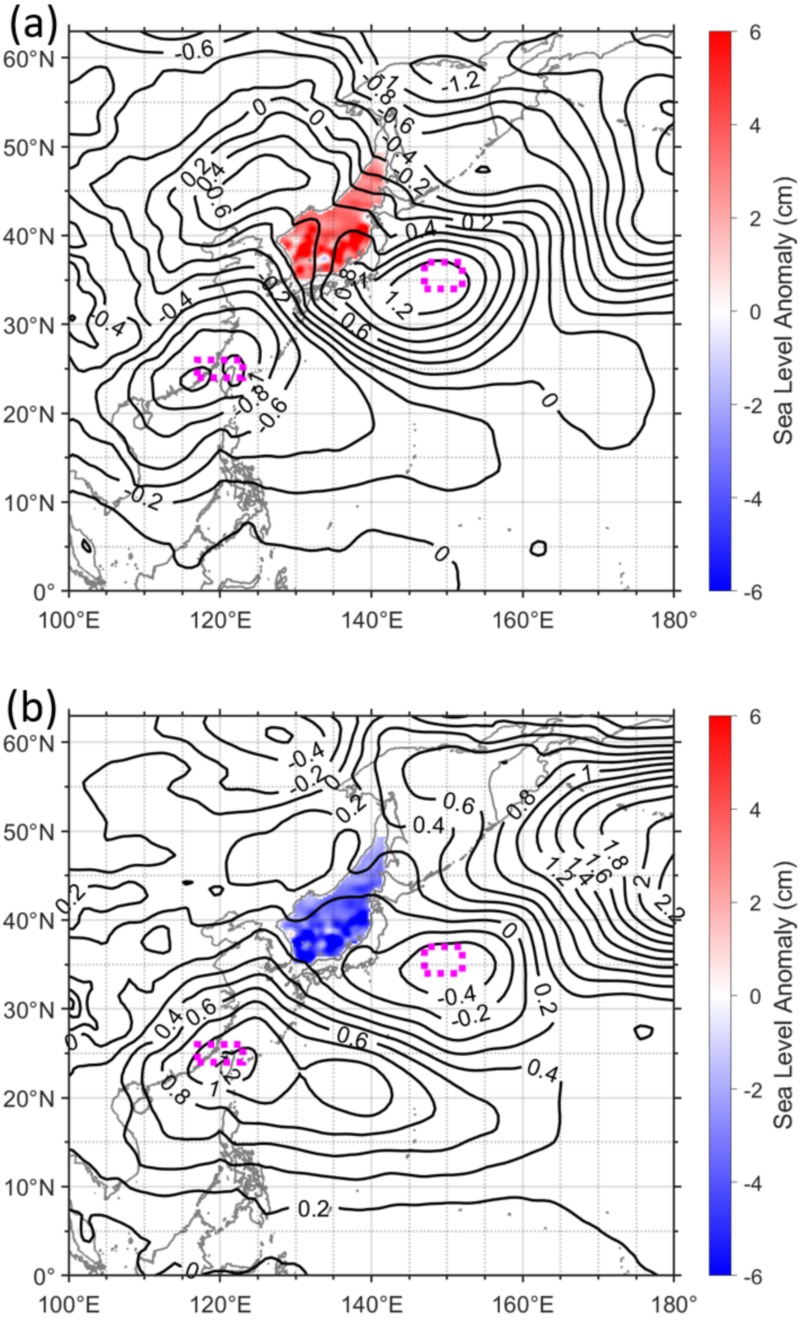

Figure 2.11 Mean sea level atmospheric pressure anomalies in summer averaged for the (a) Period H and (b) Period L in the northwest Pacific Ocean (contour interval: 0.2 hPa, ECMWF). The SESA are superimposed with a color scale (red: positive, blue: negative) and the areas defining the SESI are denoted by magenta dotted boxes. Coastlines are drawn in gray.

2.4. Discussion

In a marginal sea, surface wind stress has been considered as one of the most important factors to change sea level and the sea level variation by wind has been previously investigated (Choi et al., 2009; Liu et al., 2010; Zuo et al., 2012; Zhang et al., 2014; Li et al., 2016; Yu et al., 2019). Monthly mean sea levels in the ES had an annual maximum in summer between the years of 1993 and 2018. Even though there were other causes for sea level variability such as surface net heat flux, air and sea surface temperatures, and geostrophic advection (Amiruddin et al., 2015), the correlations of SESA with wind stress and atmospheric pressure distribution were significant.

It was found that summer sea level in the ES could be controlled by the wind stress, especially in the entrance of currents in the ES, due to atmospheric pressure disturbances. Thus, SESA can be estimated with atmospheric pressure distribution in the vicinity of the ES. If summer ES sea level index (SESI) was defined as the difference of atmospheric pressure anomalies between the KE (147.75–151.50 °E, 34.50–36.75 °N) and around Taiwan (117.75–122.25 °E, 24.75–25.50 °N) (KE minus Taiwan, magenta dotted boxes in Figure 2.10 and Figure 2.11)), the correlation coefficient between SESI and SESA was 0.70 (p-value < 0.01) (Figure 2.12). SESI as a local index was compared with other climate indices. The climate indices which were used in this study were the Aleutian Low Pressure Index (ALPI), Artic Oscillation Index (AOI), East Asian Summer Monsoon Index (EASMI), North Pacific Gyre Oscillation (NPGO), North Pacific Index (NPI), Oceanic Niño Index (ONI), Pacific Decadal Oscillation (PDO), and Siberian High Index (SHI) from 1993 to 2018. The ALPI was only compared with SESI for the years between 1993 to 2015. There was a significant correlation between SESA and

EASMI which was normalized wind vector difference between January and August at 850 hPa in the east Asian monsoon domain (110–140 °E, 10–40 °N) (Li and Zeng, 2002). Its correlation coefficient is 0.53 (p-value: 0.01) (Figure 2.12). However, correlations of SESA with other climate indices (ALPI, AOI, NPI, ONI, PDO, SHI) were not significant except NPGO (0.40, p-value: 0.05). SESI was better than EASMI in estimating SESA even though the ES sea level changes in summer were highly correlated to the East Asian Summer Monsoon. The relationship between SESI and SESA (correlation coefficient, 0.70 with p-value < 0.01) can be expressed using Equation (3):

$$\mathrm{SESA}\ \ (\mathrm{cm}) = 0.83 \times \mathrm{SESI}\ \ (\mathrm{hPa}) \tag{3}$$

Neither SESI nor EASMI agree well with the SESA from 2001 to 2002, when the high and low atmospheric pressure moved farther eastward in 2001, and there were strong wind stress and atmospheric pressure around the KS, not between KE and around Taiwan in 2002 (not shown), implying other causes of changing the ES sea level during those years. Although there were onshore and offshore current changes according to annual changes of summer wind stress in the ES, the changes of current were not consistent in Periods H or L, and their effects in the ES could not change SESA. There were more typhoons in August which passed through the ES for Period H than Period L. This might be because of atmospheric pressure distribution, and its cause and effect needed to be investigated more in the near future.

Although the wind-induced Ekman transports within the semi-enclosed deep basins in the ES played a key mechanism for the interannual variability of SESA, another mechanism for this variability could be considered. A warming process due to increased surface net heat flux (mean: ~326 W m^{-2}) from the atmosphere to the ocean was less than 0.2 % in Period H compared to that in Period L. The sea level increase due to 0.2% surface net heat flux increase raised the steric sea level by O(10^{-5} m) at the most. Thus, the effect of surface net heat flux between Periods H and L was ignored. Another warming process due to 3 % or 8 % decreased sea surface wind speed via increased heat gain from the atmosphere in the ES might raise the steric (thermosteric) sea level during Periods H or L compared to 26-year mean, respectively if temperature and humidity differences between the atmosphere and the ocean, and coefficients of the turbulent heat flux formula were same. However, this possibility was ruled out based on ~158 W m^{-2} of the mean summer turbulent (sensible and latent) heat flux from the ocean to the atmosphere from ECMWF in the ES. Sea surface warming corresponding to the weaker wind speed raise the steric sea level by O(10^{-3} m) at the most, was one order of magnitude smaller than those induced by the anomalous Ekman transports O(10^{-2} m) as the anomalous heat gain via ~8 to 13 W m^{-2} of less turbulent heat flux from the ocean to the atmosphere corresponding to negative anomaly in wind speed. These would warm the surface water by 0.01–0.03 °C from 23.09 °C to 23.10–23.12 °C in the ES (if mean summer SST in the ES from 1995 to 2017 in World Ocean Atlas 2018 (WOA18) was 23.09 °C and the turbulent heat flux affects from the surface to lower thermocline around 250 m), yielding sea level rise of ~0.001 m at the most. Freshwater exchange between atmosphere and ocean can affect also the steric (halosteric) sea level, but it was even smaller by a factor of 0.1 than the thermosteric sea level change in the region (Munk, 2003; Kang et al., 2005). Therefore, this possibility was ruled out as well from the key mechanism for the interannual variability of summer mean sea level in the ES.

The typhoons which passed between KS and Taiwan in summer were counted because the atmospheric pressure distribution might affect the path of typhoon for Periods H or L, respectively. Average number of typhoons were 3.3 and 1.1 for Periods H and L, respectively. The correlation coefficients between typhoon numbers passed between the KS and Taiwan, and sea level anomaly in the ES in summer was 0.51 (p-value < 0.01). Thus, there were more typhoons in summer which passed the south of the ES for Period H than Period L. The effect of typhoon on the sea level between two periods should be investigated more in the future.

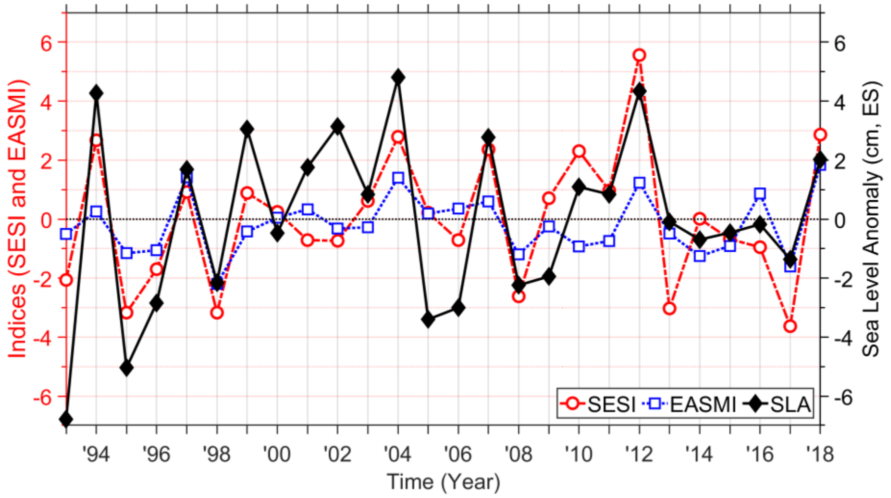

Figure 2.12 Time series of the SESI (red dashed line with open circles), the EASMI (blue dotted line with open squares), and the SESA (black solid line with filled in diamonds) in August from 1993 to 2018. Correlation coefficients of SESA with SESI and EASMI are 0.70 (p-value < 0.01) and 0.53 (p-value = 0.01), respectively.

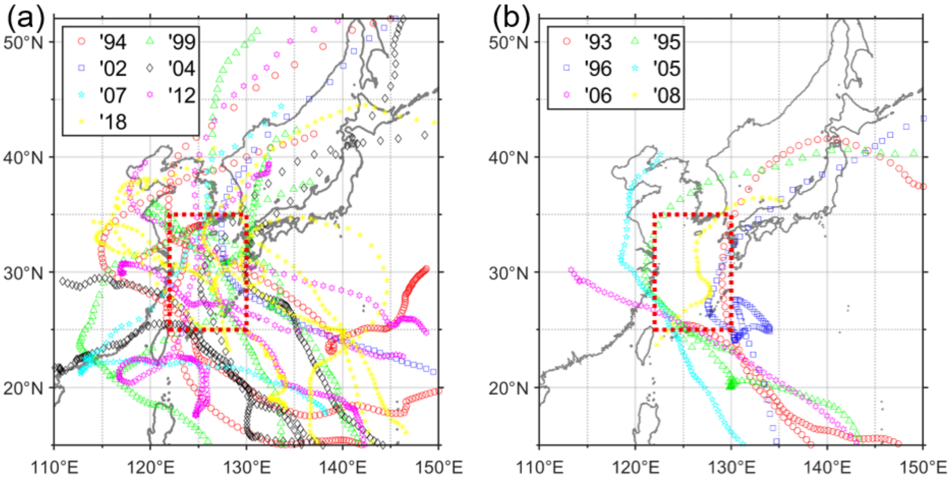

Figure 2.13 Typhoons passed between the KS and Taiwan (red dotted box) for Periods (a) H and (b)L.

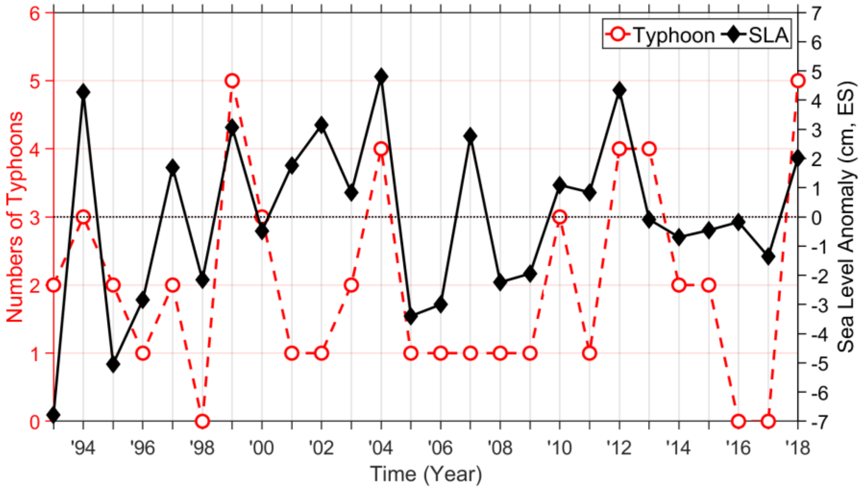

Figure 2.14 Time series of typhoon numbers passed between the KS and Taiwan (red circle), and sea level anoamly in the ES (black diamonds) in summer. Correlation coefficient of them is 0.51 (p-value < 0.01).

2.5. Conclusions

Sea levels from tide-gauge observations in the ES, between 1993 and 2018, reached annual maximums in summer and sea levels from satellite observations showed remarkable interannual variations. The rising rate of summer sea level from satellite altimetry data was larger than that of annual mean in the ES which itself was larger than that of global mean sea level. Interannual variation of sea levels in the ES in summer was dominated by the atmospheric pressure gradients between KE and around Taiwan. In Period H (Period L), the SESA became positive (negative) due to the large (small) atmospheric pressure gradients between KE and around Taiwan in the south of the ES (Figure 2.15).

SESA was mainly determined by atmospheric pressure and wind stress in the south of the ES, and could be estimated by SESI. Local atmospheric forcing might have a greater influence on sea levels than remote ones. SESI was more influential than other climate indices, including EASMI and NPGO, on the SESA. Other non-steric and steric effects on sea level anomalies in summer should be considered to accurately estimate SESA in the future. Our results spotlight the significant effect of local atmospheric pressure distribution and wind stress, on sea levels, in the vicinity of marginal seas. This effect can be used to estimate sea levels with atmospheric pressure anomaly differences.

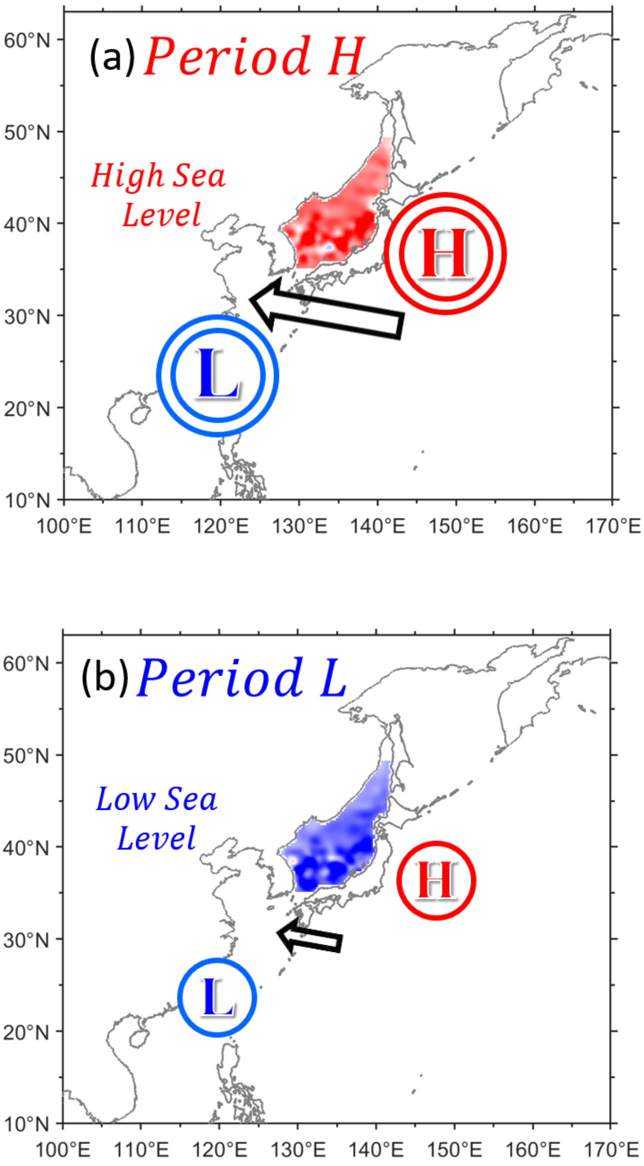

Figure 2.15 Schematic diagrams accounting for the SESA. (a) Strong west-northwestward wind stress (longer black arrow) is a result of large atmospheric pressure gradients (double circled red and blue H and L, respectively) in the northwest Pacific Ocean. Strong wind stress enhances Ekman transport from the Pacific into the ES by Ekman transport, which results in high sea levels in the ES (red) during Period H. (b) Weak wind stress (shorter black arrow) is a result of small atmospheric pressure gradients (single circled red and blue H and L, respectively). Weak wind stress decreases Ekman transport, which results in low sea level in the ES (blue) during Period L. Coastlines are drawn in gray.

3. Winter sea level

3.1. Introduction

Although there have been many studies on the sea level variability at a specific area in the ES, interannual variations of the winter ES mean sea level over the whole area have not been investigated.

The standard deviation of sea level from satellite altimetry observation shows a maximum in winter. The monthly mean wind stress, which can pile up and raise the sea level, and vice versa in the ES, is also maximum in winter. Moreover, the correlations between monthly sea level anomaly in the ES and wind stress anomaly around the ES were significant in winter. Thus, a study on the effects of the wind stress and atmospheric pressure on the sea level variations in winter is necessary.

Although there were extensive previous studies on the sea level variability at or within specific parts of the ES, interannual variations of the winter ES mean sea level over the whole ES have not been investigated yet. In this study, it was attempted to address the effect of the wind stresses and atmospheric pressure disturbances on the interannual ES sea level variability. This study focuses on the winter (November and December; ND) period in which the interannual spread is relatively large and the monthly mean wind stress has a maximum value.

In chapter 3, it was tried to understand the mechanism of the interannual ES sea level variability caused by atmospheric pressure and wind stress in winter. The data and methods are presented in Section 3.2, and the results and discussion are described in Sections 3.3 and 3.4, respectively. Conclusions are in Section 3.5.

3.2. Data and Methods

Monthly mean time series of the sea level in the ES (cyan shaded area in Figure 2.1) from 1993 to 2018 were produced using daily ADT provided by the Copernicus Marine Environment Monitoring Service (CMEMS, 2020a) same as section 2.2. Separately, annual mean time series of the sea level in the ES from 1993 to 2018 were constructed from observations at nine tide gauge stations (red open squares in Figure 2.1) provided by the PSMSL same as section 2.2. Daily mean surface atmospheric pressures and wind stress data obtained from the ECMWF ERA-Interim were used in this study to construct monthly mean time series of gridded wind stresses and atmospheric pressures from 1993 to 2018 with a horizontal resolution of 0.75° in the area covering the ES (117°E–157°E, 24°N–55°N).

Satellite and ECMWF data were processed to remove the linear trend over the total period (26 years) and extract annual or winter (ND) mean values averaged over the ES area or at each grid. Then, composite analyses using anomalously high or low winter sea level data, correlation analyses, multiple regression analyses, and Ekman dynamics that account for wind-driven upper ocean convergence and divergence were applied to address the dominant processes underlying the interannual variability of the winter ES sea level. Known climate indices were used to compare the estimative ability of the winter ES sea level.

3.3. Results

3.3.1. ES mean sea level variations

Two independent annual mean sea level observations, one from satellite altimetry and the other from tide gauge stations, showed a consistent long-term trend and interannual variations in the ES mean sea level, despite missing samples from tide gauge stations in the northern ES. Rates of long-term sea level rise estimated from the ADT of satellite altimetry (CMEMS, 2020b) and tide gauge observations were 3.672 (dotted red lines in Figure 3.1a) and 2.973 mm/year (not shown), respectively, yielding a difference of an order of 0.7 mm/year or less because of some missing tide-gauge data in 2018. Even though there were many potential sources of error in both datasets (e.g. altimetry data corrections considering regional specifications and limited coverage and uneven distributions of tide gauge data sampling with no correction for non-isostatic sea level responses to atmospheric pressure loading within the semi-enclosed marginal sea, e.g., (Lyu et al., 2002; Nam et al., 2004; Lyu and Kim, 2005)), the annual mean sea levels derived from these two independent sets of observation agreed well, with a significantly high correlation coefficient (0.93). Thus, only satellite observation data as sea levels would be used from now on.

The winter (ND) mean sea level from satellite observation also showed a comparable rising sea level rate (4.227 mm/year) but has a significantly large spread from the annual mean, allowing for strong interannual variability (black diamonds in Figure 3.1a). For example, the winter mean sea level in the ES, after being de-trended, is 5 cm higher in 2016 and 6 cm lower in 2017 than the baseline sea level (expected from the long-term rate, black dotted line in Figure 3.1a); such spreads were particularly large in winter (November and December) compared to spreads in other months (Figure 3.1b).

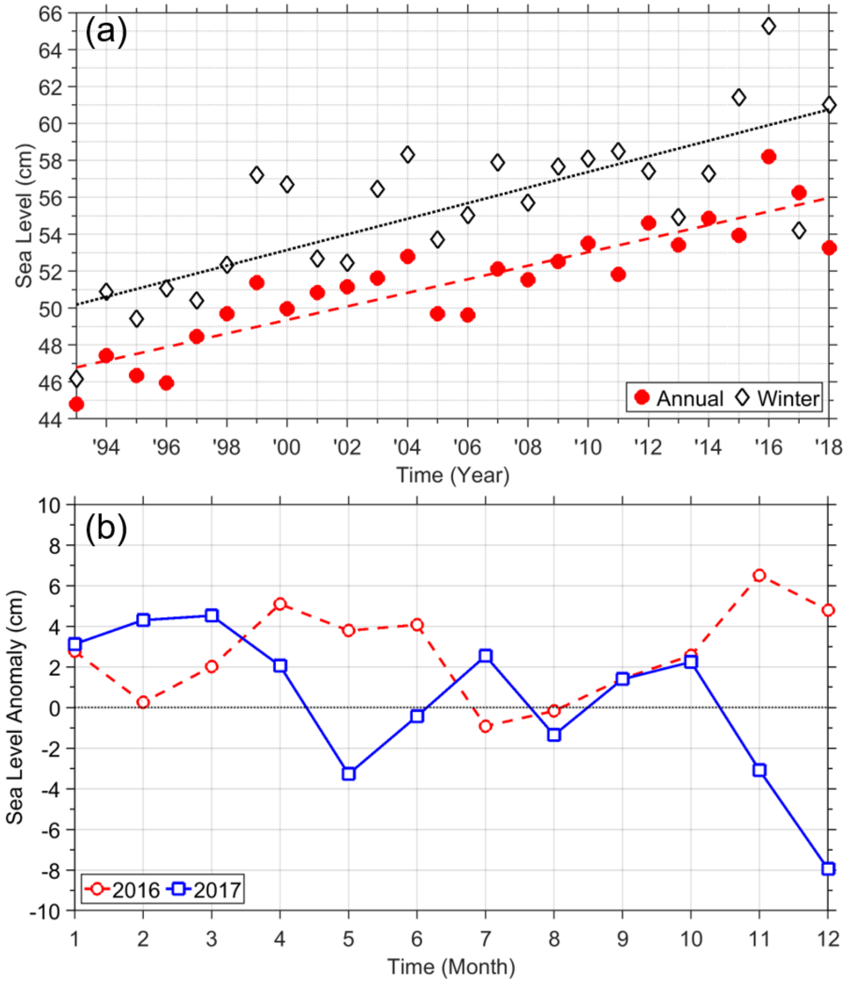

Figure 3.1 (a) Annual (red filled circles) and winter (black open diamonds) mean sea levels and trends of satellite altimetry data from 1993 to 2018 in the ES. (b) Monthly mean sea levels in 2016 (open red circle) and 2017 (open blue square).

3.3.2. Local winds during periods of high vs. low sea levels

The interannual variations of the winter ES sea level anomaly (WESA) were analyzed to identify seven years of relatively high (positive anomalies above +1.5 cm) and low (negative anomalies below -1.5 cm) sea levels in Period H (1999, 2000, 2003, 2004, 2007, 2015, and 2016) and Period L (1993, 1995, 1997, 2002, 2005, 2013, and 2017), respectively (Figure 3.2). Then, the atmospheric pressure fields and associated wind stresses during the two periods were compared to qualitatively account for the high and low winter sea levels in the ES. In the ES, which is influenced by the east Asian winter monsoon, a north-westerly wind prevails in the winter with an enhanced atmospheric pressure gradient between the Siberian High and the Aleutian Low (Figure 3.3), as has been reported in previous studies (Jhun and Lee, 2004). During Period H, the Aleutian Low retreats north-eastward, and the north-westerly monsoonal wind exerting south-eastward wind stress at the sea surface is stronger in the southern OS than in the southern ES (Figure 3.3a). The Ekman dynamics suggest south-westward Ekman transport within the surface Ekman layer induced by the south-eastward wind stress, which causes blocking of the outflow transport from the ES to the Pacific (and OS) through the TS and SS and results in water pile-up or horizontal convergence within the ES (Figure 1.1 and Figure 3.3a).

In contrast, during Period L, the Aleutian Low expands south-westward, and a north-westerly monsoonal wind exerting south-eastward wind stress at the sea surface is stronger in the southern ES than in the southern OS (Figure 3.3b). The Ekman dynamics again suggest south-westward Ekman transport within the surface Ekman layer induced by the south-eastward wind stress. In this case, this would cause the blocking of the inflow transport from the Pacific to the ECS shelf and from the Yellow and East China Seas (YECS) to the ES through the KS, resulting in horizontal divergence within the ES (Figure 1.1 and Figure 3.3b). Note that outflow transport from the ES to the Pacific (and also OS) would not be blocked in this case because the south-eastward wind stress is much weaker in the southern OS during Period L than during Period H (Figure 3.3b).

Although a north-westerly wind prevails in the OS, ES, and YECS, the atmospheric pressure gradient between the Siberian High and Aleutian Low was noticeable during the winter monsoon, as previously reported (Jhun and Lee, 2004) and confirmed herein from the mean fields over the total period (Figure 3.4a). Thus, significant interannual variations in the local atmospheric pressure disturbance and the wind field influence the interannual variability of the winter ES sea level via Ekman dynamics. Westward and south-eastward wind stress anomalies in the southern ES and OS, respectively, enhance the inflow transport into the ES and reduce the outflow transport into the Pacific more during Period H than during Period L (Figure 3.4b).

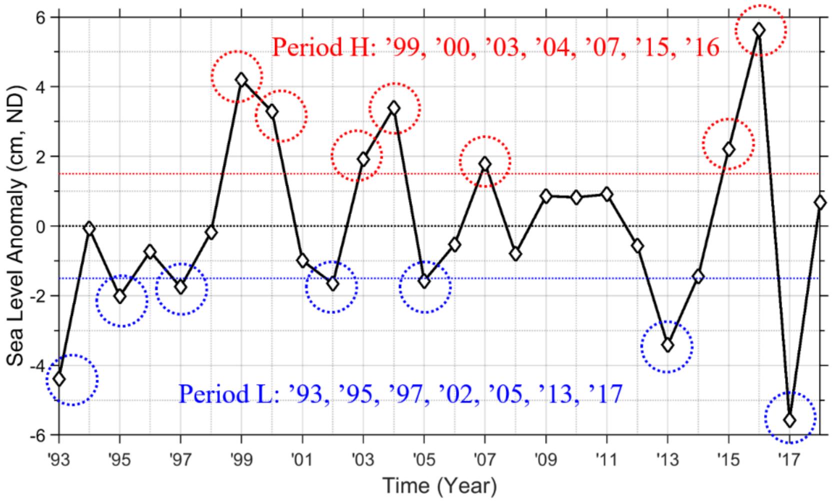

Figure 3.2 Time series of the de-trended winter (November and December) mean sea level anomalies averaged over the ES from 1993 to 2018, in which seven year high (higher than 1.5 cm) and low (lower than 1.5 cm) winter sea level anomalies are denoted as Period H (1999, 2000, 2003, 2004, 2007, 2015, and 2016) or Period L (1993, 1995, 1997, 2002, 2005, 2013, and 2017) with red and blue circles, respectively.

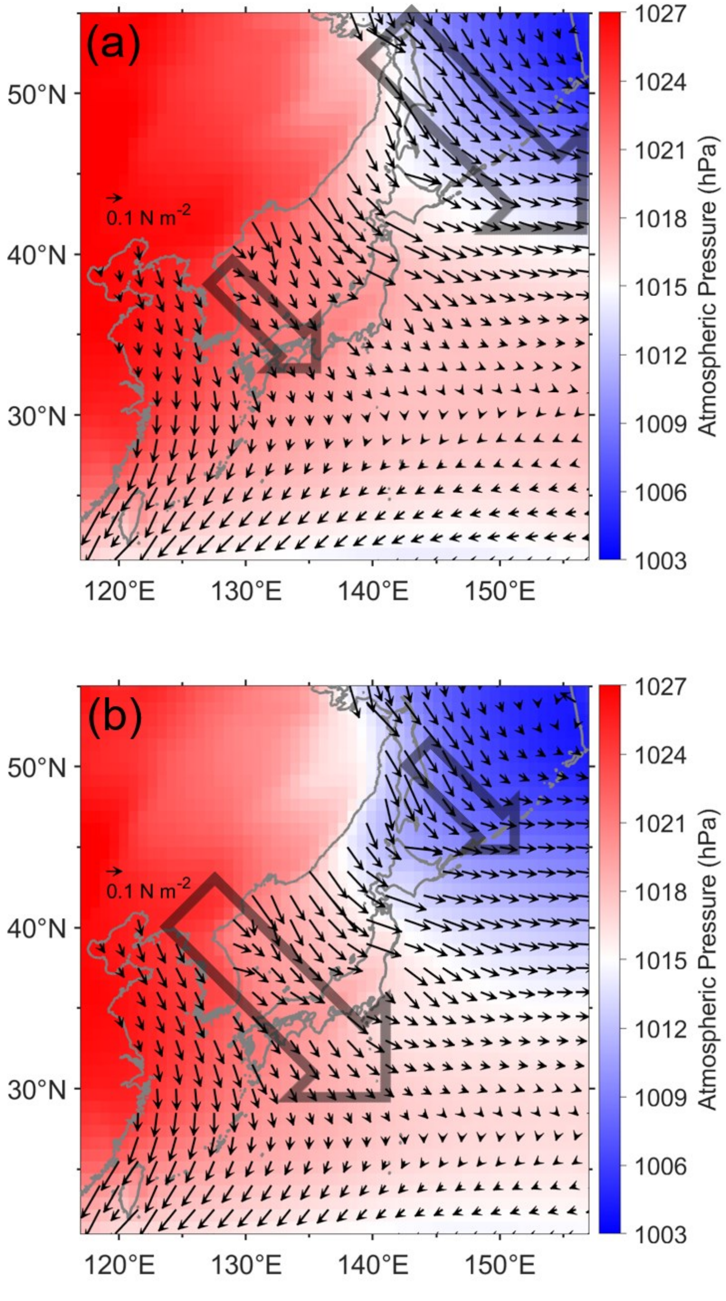

Figure 3.3 Composite maps of winter mean atmospheric pressure at sea level (hPa), surface wind stress (N m^{-2}, small arrows), and north-westerly monsoonal winds exerting south-eastward wind stress on the sea surface (large open arrows) for Periods (a) H and (b) L.

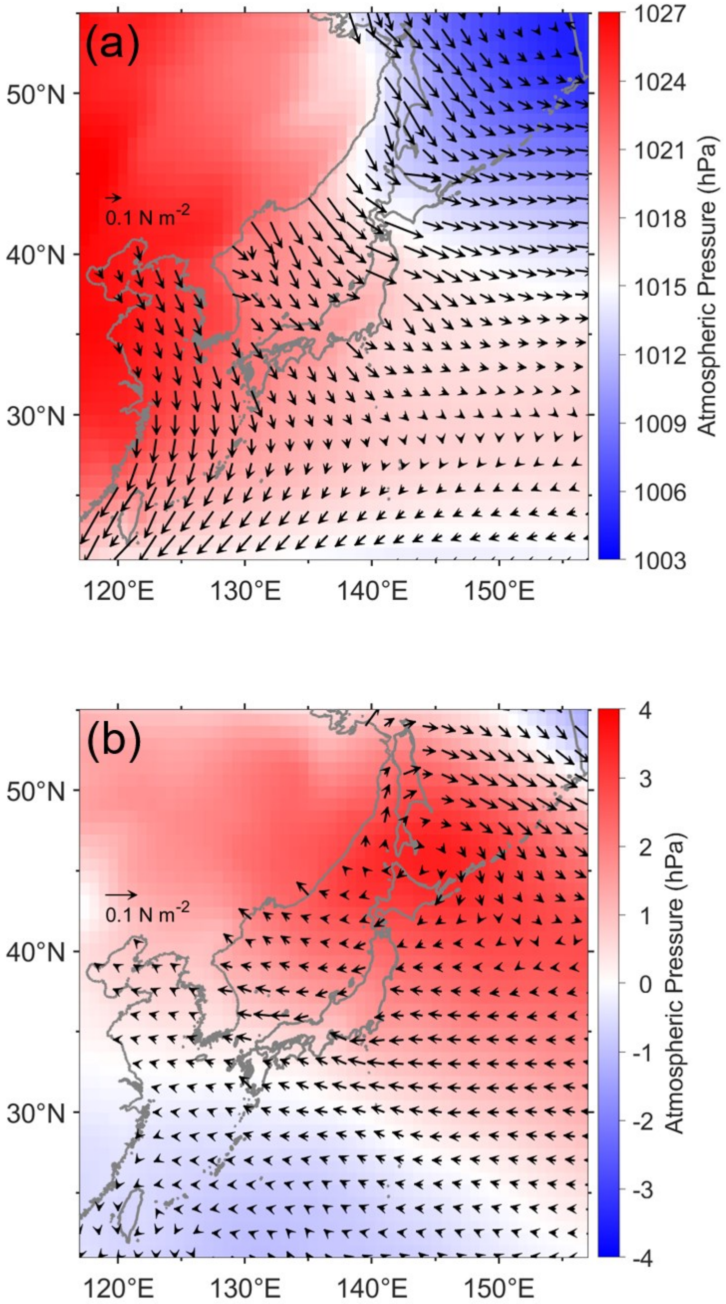

Figure 3.4 Composite maps of winter mean atmospheric pressure at sea level (hPa) and wind stress (N m^{-2}, small arrows) (a) for the total period of 26 years (1993–2018) and (b) the difference between Periods H and L (Period H shown in Figure 3.3a minus Period L shown in Figure 3.3b).

3.3.3. Wind-induced sea level anomalies

To quantitatively examine the effects of local wind forcing on the winter ES sea level variability, areas of strong interannual south-eastward wind stress (τ_{SE}) variability that correlate highly with sea level anomalies were identified as WA (128.5–134.2°E, 35.0–40.0°N) and WB (146.0–153.0°E, 46.5–51.5°N) within the ES and OS, based on a correlation map between τ_{SE} and sea level anomalies (Figure 3.5). The correlation map of τ_{SE} with the sea level anomaly indicates positive (negative) values at WB (WA) in the southern OS (ES), demonstrating that high ES sea level occurs with increased (decreased) south-eastward wind stress at WB (WA) in the southern OS (ES) (Figure 3.5).

The increased (decreased) τ_{SE} in the WB (WA) by +0.036 $\mathrm{N\ m^{-2}}$ (-0.018 $\mathrm{N\ m^{-2}}$) from 0.058 to 0.094 $\mathrm{N\ m^{-2}}$ (from 0.054 to 0.036 $\mathrm{N\ m^{-2}}$) during Period H and the decreased (increased) τ_{SE} in WB (WA) by -0.018 $\mathrm{N\ m^{-2}}$ (+0.016 $\mathrm{N\ m^{-2}}$) from 0.058 to 0.040 $\mathrm{N\ m^{-2}}$ (from 0.054 to 0.070 $\mathrm{N\ m^{-2}}$) during Period L can be used to estimate changes in the south-westward Ekman transport per unit length within the surface Ekman layer ($VT_{Ekman_{SW}}$, $m^2\ s^{-1}$) using Equation (1).

The resulting south-westward Ekman transport anomalies per unit length were +0.322 (-0.192) $\mathrm{m^2\ s^{-1}}$ in the WB (WA) during Period H and -0.153 (+0.180) $\mathrm{m^2\ s^{-1}}$ in the WB (WA) during Period L. During Period H, therefore, the horizontal water convergence within ES due to decreased outflow and increased inflow transports (0.192 and 0.322 $\mathrm{m^2\ s^{-1}}$, respectively) reaches 0.514 $\mathrm{m^2\ s^{-1}}$ (= 0.192 + 0.322), which corresponds to O(0.01 Sv, $1\ \mathrm{Sv} = 10^6\ \mathrm{m^3\ s^{-1}}$) over a horizontal distance of O(10 km). For example, for given scales of the horizontal fetch distance of O(10^4 m), volume transport inducing this horizontal convergence across the fetch scale would be 5140 $\mathrm{m}^3\ \mathrm{s}^{-1}$ (= 0.514 $\mathrm{m}^2\ \mathrm{s}^{-1}$ ×10^4 m). This volume transport into the ES, integrated over a time scale of one month (= 2.6 × 10^6 s) and divided by the area of the ES (= 1.0 × 10^{12} m^2), yields a sea level rise of ~1 cm (=5140 $\mathrm{m}^3\ \mathrm{s}^{-1}$ × 2.6 × 10^6 s / (1.0 × 10^{12} m^2) = 0.0134 m ≈ 0.01 m). Similarly, the horizontal water divergence within the ES due to increased outflow and decreased inflow transports (0.180 and 0.153 $\mathrm{m}^2\ \mathrm{s}^{-1}$ respectively) was estimated to be 0.333 $\mathrm{m}^2\ \mathrm{s}^{-1}$ (= 0.180 + 0.153), which corresponds to O(0.01 Sv) over the same horizontal fetch distance of O(10 km), lowering the ES sea level by O(0.01 m) or ~1 cm in a month, e.g., –0.333 $\mathrm{m}^2\ \mathrm{s}^{-1}$×$10^4$ m × 2.6 × 10^6 s / (1.0 × 10^{12} m^2) = –0.0087 (m) ≈ –0.01 m.

Likewise, using Equation (2), sea level anomalies induced by the horizontal convergence or divergence of wind-driven net incoming Ekman transport (Figure 3.6a, b) can be compared to the ES sea level derived from the satellite altimetry (Figure 3.6c, d). The positive (negative) result in the ES was due to the south-westward Ekman transport anomaly caused by wind stress in the southern OS (ES) for Period H (Period L) in Figure 3.3. Even though the sea level anomalies of the entire ES were not positive (negative) for Period H (Period L), the averaged sea level anomalies in the ES were positive (negative) (Figure 3.6).

A multiple linear regression of wind-stress anomalies in the WA and WB on the ES sea level anomaly was used to investigate its estimative ability with the following results:

$$SLA_{ES} = -0.410\ \tau_{WA} + 0.108\ \tau_{WB}. \tag{4}$$

Here, SLA_{ES} was the WESA (m), and τ_{WA} and τ_{WB} were the south-eastward wind-stress anomalies averaged over WA and WB ($\mathrm{N\ m^{-2}}$), respectively. The results of this multiple linear regression analysis yield a significant correlation coefficient of 0.56 ($p < 0.01$), suggesting that the interannual SLA_{ES} variability can be reasonably estimated by τ_{WA} and τ_{WB} (Figure 3.7). The magnitude of the coefficient of τ_{WA} (0.410) was approximately four times larger than that of τ_{WB} (0.108), and the standard deviation of τ_{WB} was double that of τ_{WA}, indicating doubled sensitivity of SLA_{ES} to τ_{WA} compared to τ_{WB} for normalized wind-stress anomalies.

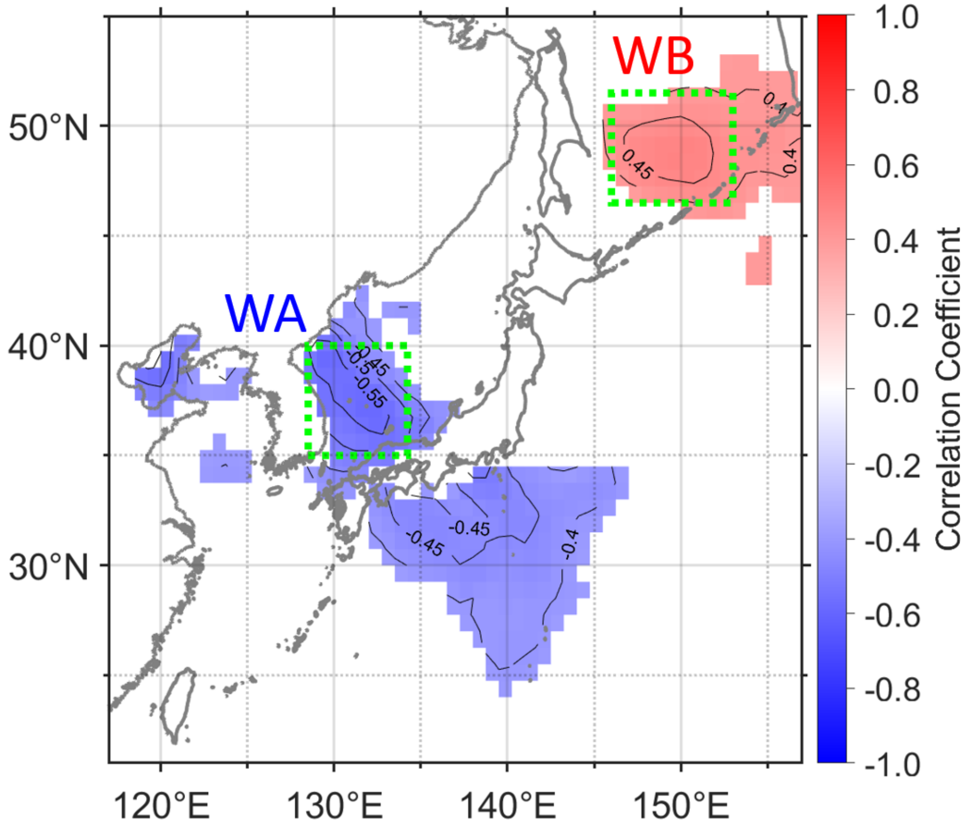

Figure 3.5 Correlation map between the WESA and the surface wind-stress anomaly in the southeast(+)-northwest(-) direction from 1993 to 2018 in the northwest Pacific Ocean. The contour interval is 0.05 and confidence levels of correlation coefficients less than 95% were discarded. A positive correlation means that a high (low) ES sea level occurs with a strong south-eastward (north-westward) wind stress anomaly. Here, the areas showing the maximum positive (WB) and minimum negative (WA) correlation coefficients are marked with green dotted boxes.

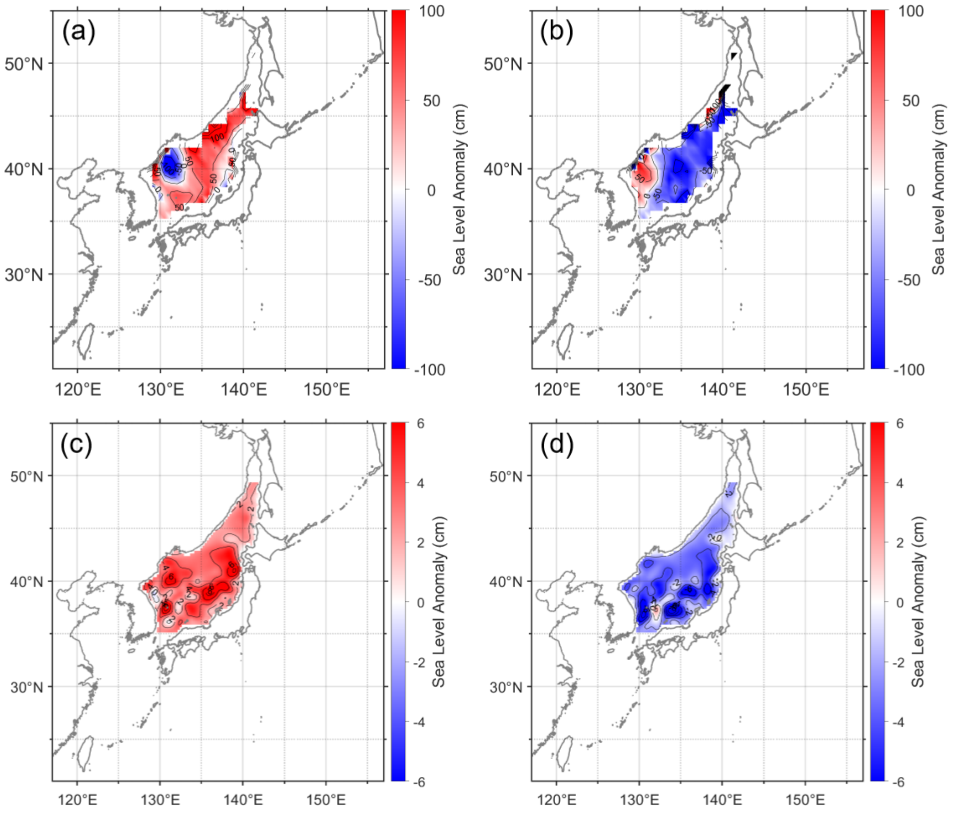

Figure 3.6 Sea level anomaly induced by horizontal convergence (red) or divergence (blue) of wind-driven net incoming Ekman transport anomaly during Periods (a) H and (b) L. The ES sea level distribution derived from satellite altimetry observations during (c) Period H and (d) Period L.

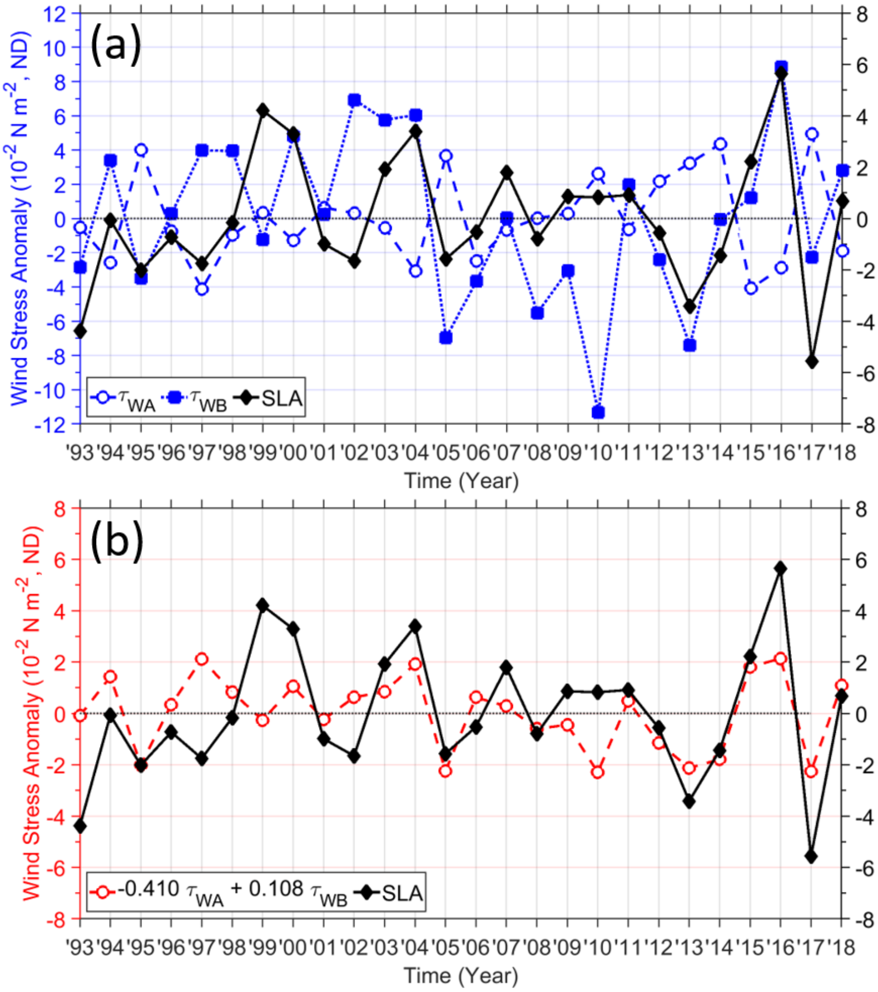

Figure 3.7 Time series of (a) south-eastward wind stress anomalies in the WA (blue open circles and dashed line, left y-axis) and WB (blue filled squares and dotted line, left y-axis), (b) multiple linear regression results from south-eastward wind stress anomalies in the WA and WB on the ES sea level anomalies (red open circles and dashed line, left y-axis), and (a, b) WESA observed from satellite altimetry (black filled diamonds and solid line, right y-axis) from 1993 to 2018. The correlation coefficient between multiple linear regression result and WESA is 0.56 with $p < 0.01$.

3.3.4. Atmospheric pressure disturbances and the winter ES sea level index (WESI)

The interannual τ_{WA} and τ_{WB} variations were linked to atmospheric pressure disturbances, such as the location of a strong atmospheric pressure gradient between the Siberian High and Aleutian Low (Figure 3.9). During Period H (Period L), a strong pressure gradient with an enhanced north-westerly wind is located northeast of the SS and in the southern OS (in the vicinity of the KS and the southern ES) (Figure 3.9a, b), yielding higher (lower) than normal atmospheric pressures around the SS (e.g. magenta dotted box in Figure 3.9c, d). Thus, a new index called the winter ES sea level index (WESI) was defined herein as the difference of atmospheric pressure anomalies in hPa averaged over the area around the SS (140.0–144.0°E, 46.0–48.0°N) minus east of Taiwan (ET; 127.5–131.5°E, 22.0–25.0°N) where the local atmospheric pressure anomalies reach their maximum and minimum (Period H), and minimum and maximum (Period L) values, respectively. The WESI is significantly correlated with SLA_{ES} (correlation coefficient: 0.58, p-value < 0.01) (Figure 3.10), demonstrating a better estimative ability than those of wind stress anomalies (τ_{WA} and τ_{WB}) or other climate indices that represent remote forcing. These climate indices were the East Asian Winter Monsoon Index (EAWMI), Oceanic Niño Index (ONI), North Pacific Gyre Oscillation (NPGO), Artic Oscillation Index (AOI), Aleutian Low-Pressure Index (ALPI), Pacific Decadal Oscillation (PDO), North Pacific Index (NPI), and Siberian High Index (SHI), and their correlations with SLA_{ES} were insignificant.

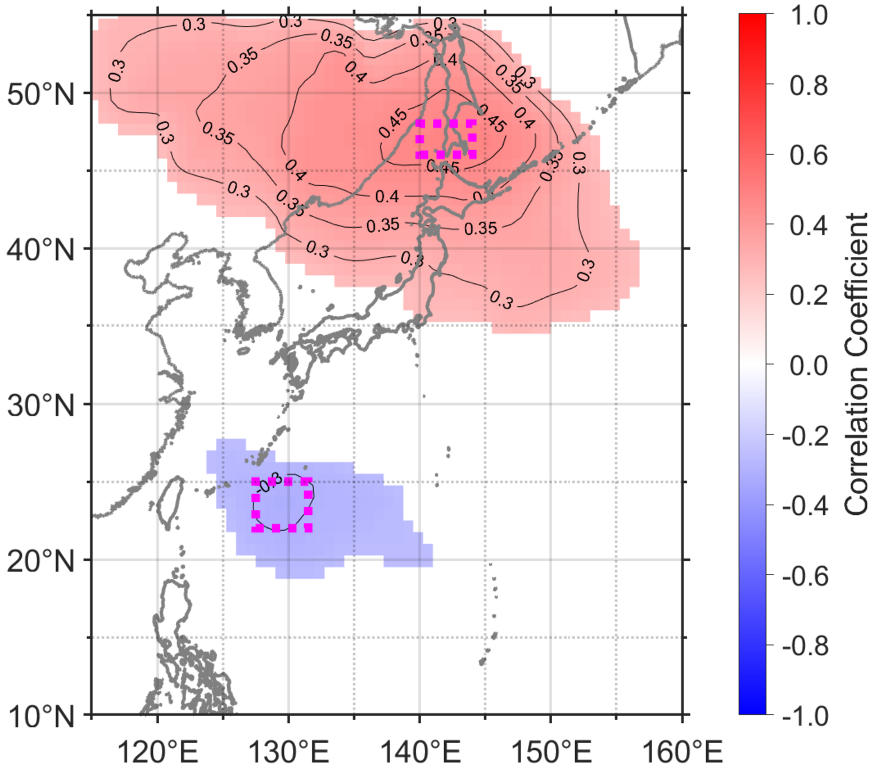

Figure 3.8 Correlation map of the WESA with the mean sea level atmospheric pressure anomaly from 1993 to 2018. The contour interval is 0.05 and the confidence level of correlation coefficients less than 80% were discarded. A positive correlation means that a high (low) ES sea level occurs with a high (low) atmospheric pressure anomaly. Here, the areas showing the positive maximum (SS) and negative minimum (east of Taiwan) correlation coefficients are marked with magenta dotted boxes.

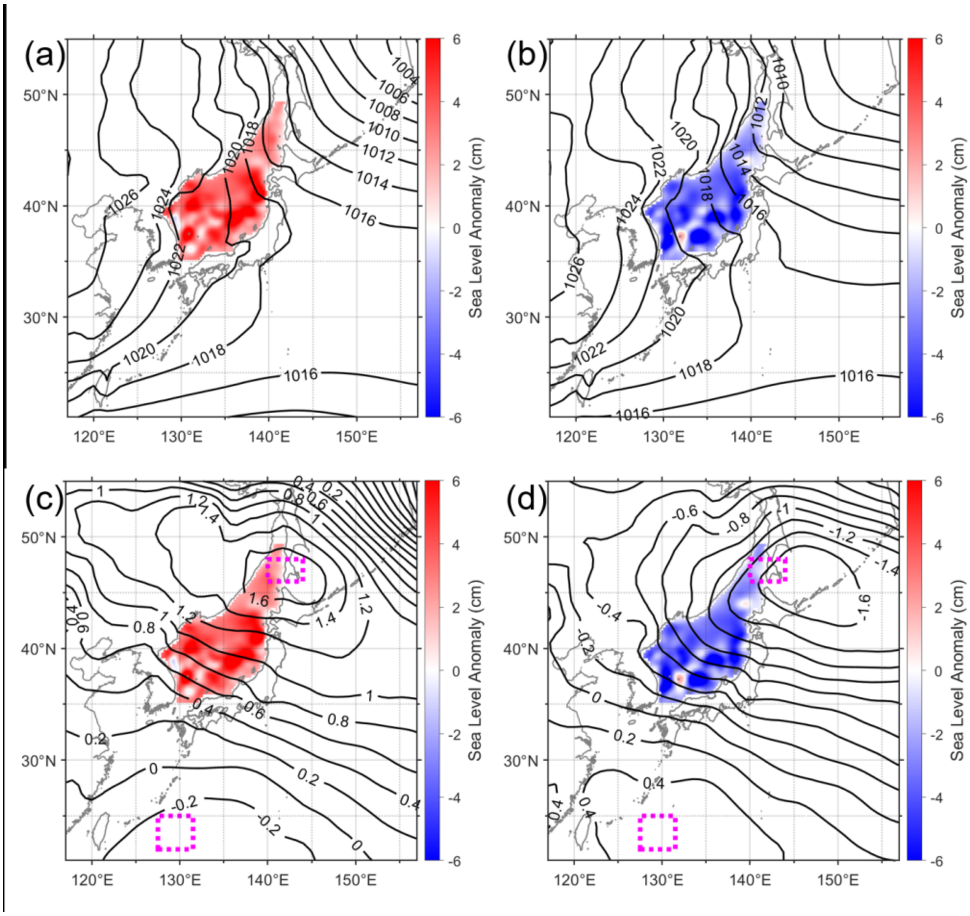

Figure 3.9 (a, b) Winter atmospheric pressure field at sea level (black contours) and (c, d) atmospheric pressure anomalies (black contours) during the (a, c) Period H and (b, d) Period L. Here, winter ES sea level anomalies are superimposed using a color scale (red: positive, blue: negative), and the area defining the winter ES sea level index is indicated with a magenta dotted boxes.

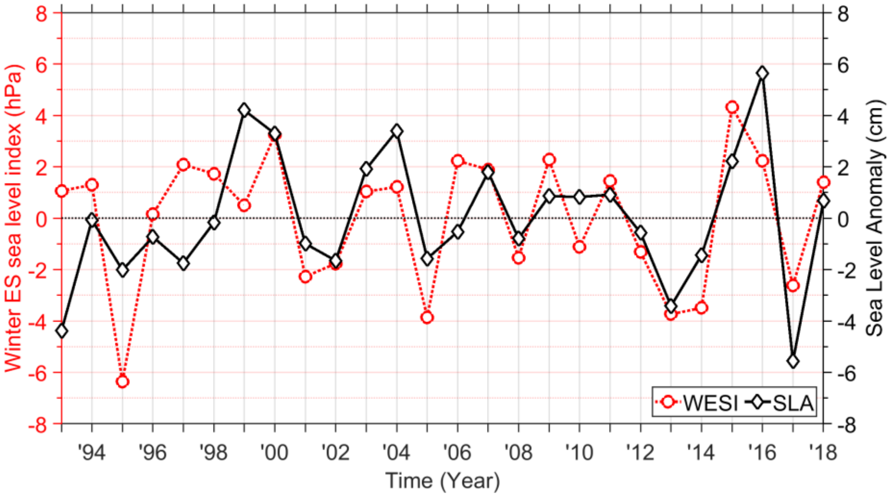

Figure 3.10 Time series of winter ES sea level index (WESI, red dotted line) and WESA (black solid line) from 1993 to 2018. Correlation coefficient is 0.58 with $p < 0.01$.

3.4. Discussion

The results of the interannual variability of the winter ES sea level induced by local wind stress forcing, especially in the exit of currents in the ES, linked to atmospheric pressure disturbances presented in this study were consistent with the results of previous studies in several aspects. Surface wind stress has been suggested as one of the most important contributors to sea level changes in marginal seas (Zuo et al., 2012; Zhang et al., 2014; Yu et al., 2019), and sea level changes induced by zonal wind stresses linked to meridional migration of the sub-polar front in the ES have been reported previously (Choi et al., 2009). For low-frequency (e.g. periods longer than 100 days) forcing, the sea level change outside the ES constrains water exchange across the straits, implying that ES basin-scale oscillations can be extended outside the ES. This study confirms this possibility, revealing basin-scale oscillations in the ES. The rapidly propagating barotropic waves homogenize the sea level across the ES, particularly for low-frequency (including interannual) timescales.

Although this study demonstrates the critical role of the south-eastward wind stress in the interannual variability of WESA via horizontal water convergence and divergence, the thermosteric and halosteric effects of properties of sea water transported into/out of the ES have not been considered. As the water carried by inflow transport into the ES across the ECS shelf and the KS was warmer and saltier than that carried by outflow transport out of the ES across the TS and SS, increased inflow transport would increase sea level more than the decreased outflow transport would for the same volume convergence. Future studies need to address the thermosteric and halosteric effects of sea water properties, along with wind-driven Ekman transport.

A better estimative ability for interannual winter ES variability is obtained by using the WESI (Figure 3.10) or by multiple linear regression of wind-stress anomalies in WA and WB (Figure 3.7) rather than from the estimates made using climate indices (remote forcing). The local atmospheric pressure disturbance that is proxied well by the Ekman transport associated with wind stress anomalies, is maximized in the areas around the SS and east of Taiwan (magenta dotted box in Figure 3.9c, d). This reflects the importance of wind-driven horizontal transport (Ekman transport) on low-frequency (interannual) sea level oscillations in lieu of atmospheric pressure loading, in contrast to the critical role of non-isostatic sea level responses to atmospheric pressure in the ES for high-frequency sea level oscillations (Lyu et al., 2002; Nam et al., 2004; Lyu and Kim, 2005; Chang et al., 2016). Neither WESI nor multiple linear regression of wind stress anomalies agree well with the winter ES sea levels from 1997 to 1999, when conventional or eastern Pacific-type El Niño (1997–1998) and La Niña (1998–2000) events occurred, implying certain roles of remote forcing via atmospheric teleconnections in changing the ES sea level during those years (Figure 3.7b and Figure 3.10). This was particularly true considering the footprint of the El Niño Southern Oscillation on the YECS (Thompson et al., 2017; Kim et al., 2018). Also, there were onshore and offshore current changes in winter according to annual changes of winter wind stress in the ES. The changes of current were not consistent in Periods H and L, and their effects could not change WESA.

Although the wind-induced Ekman transports within the semi-enclosed deep basins in the ES play a key mechanism for the interannual variability of WESA, another mechanism for this variability can be considered. A cooling process due to 4% increased surface net heat flux into the atmosphere in the ES may lower the steric (thermosteric) sea level during Period L compared to Period H. However, this possibility was ruled out based on ~619 W m^{-2} of the mean surface net heat flux (into the atmosphere) from ECMWF in winter in the ES. Sea surface cooling corresponding to the more heat loss into the atmosphere lower the steric sea level by O(10^{-3} m) at the most, one order of magnitude smaller than those induced by the anomalous Ekman transports O(10^{-2} m) as the anomalous heat loss via ~25 W m^{-2} of more surface net heat flux would cool the surface water by 0.06 °C from 11.63 °C to 11.57 °C in the region (mean winter SST in the ES from 1995 to 2017 in WOA18 if the turbulent heat flux affect from the surface to lower thermocline around 250 m), yielding sea level drop of ~0.003 m at the most.

Another cooling process due to 17% increased sea surface wind speed via increased heat loss into the atmosphere in the ES may lower the steric (thermosteric) sea level during Period L compared to Period H if temperature and humidity differences between the atmosphere and the ocean, and coefficients of the turbulent heat flux formula were same. However, this possibility was ruled out based on ~631 W m^{-2} of the mean turbulent (sensible and latent) heat flux from ECMWF in winter in the ES. Sea surface cooling corresponding to the stronger wind speed lower the steric sea level by O(10^{-2} m) at the most, similar order of magnitude to those induced by the anomalous Ekman transports O(10^{-2} m) as the anomalous heat loss via ~107 W m^{-2} of more turbulent heat flux corresponding to positive anomaly in wind speed would cool the surface water by 0.3 °C from 11.6 °C to 11.3 °C in the region (mean winter SST in the ES from 1995 to 2017 in WOA18 if the turbulent heat flux affect from the surface to lower thermocline around 250 m), yielding sea level drop of ~0.01 m at the most. Freshwater exchange between atmosphere and ocean can affect also the steric (halosteric) sea level, but it was even smaller by a factor of 0.1 than the thermosteric sea level change in the region (Munk, 2003; Kang et al., 2005). Therefore, it was needed to include this thermosteric possibility as a key mechanism for the interannual variability of winter mean sea level in the ES in the near future.

3.5. Conclusions

In this chapter, it was presented that interannual variations of winter sea levels averaged in the ES for 26 years (1993–2018) which were successfully explained by horizontal water convergence and divergence due to monsoonal wind-induced Ekman transport. Composite analyses with two contrasting periods of high (Period H) and low (Period L) winter ES sea level anomalies and correlation analyses with spatial patterns of south-eastward wind stress anomalies between the two marginal seas, ES and OS, and atmospheric pressure anomaly differences between the SS and east of Taiwan were conducted to reveal that the winter ES sea level rises (drops) with water convergence (divergence) with stronger south-eastward wind stress in the southern OS (ES) than in the southern ES (OS) during Period H (Period L). The Ekman dynamics suggest that the decreased outflow transport from the ES to the Pacific and OS through the TS and SS (decreased inflow transport into the ES through the KS) and increased inflow transport from the Pacific to the ES (increased outflow transport from the ES to the Pacific and OS) due to increased south-westward Ekman transport linked to enhanced south-eastward wind stress in the southern OS (southern ES) played a key role. Our results highlight the important roles of local wind forcing and Ekman dynamics in changing the winter sea level variability in the ES, providing a better estimative ability with atmospheric pressure anomalies proxied via WESI (correlation coefficient: 0.58 with $p < 0.01$) or multiple regression wind stress anomalies, rather than by remote forcing (climate indices).

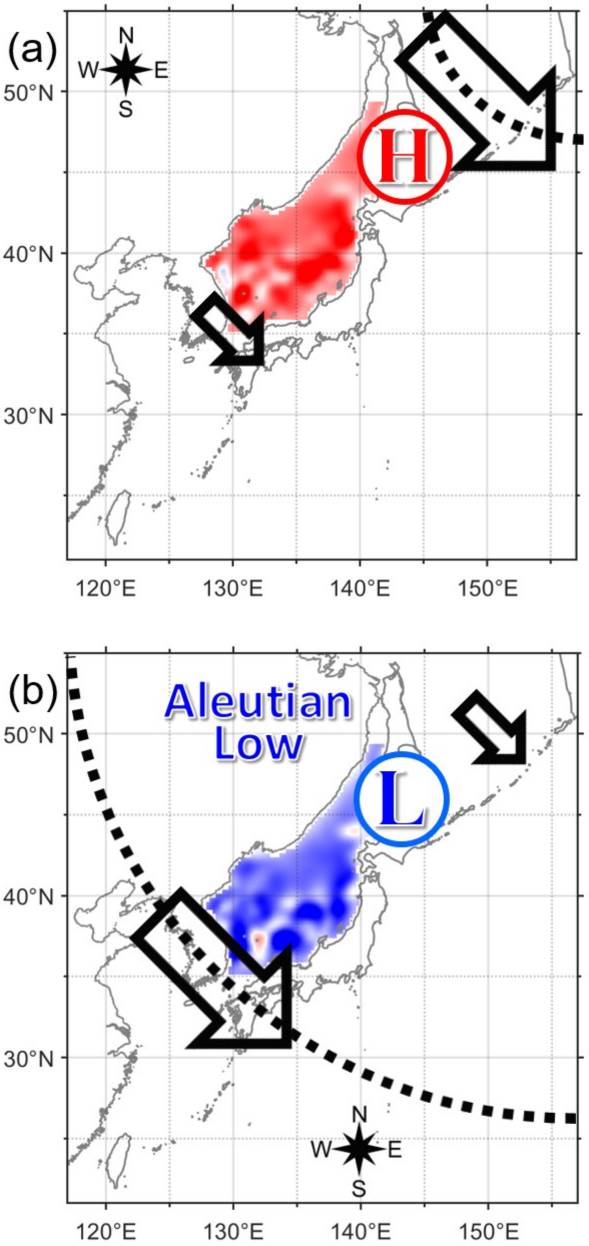

Figure 3.11 Schematic diagrams accounting for the winter ES sea level anomalies. (a) A stronger winter monsoon with north-westerly wind or south-eastward wind stress (bigger black arrow) and associated atmospheric pressure gradients (black dotted lines) in the southern Okhotsk Sea; e.g. the north-eastward retreat of the Aleutian Low blocks outflow transport from the ES into the Pacific and OS by Ekman dynamics to yield a higher (red) ES sea level during Period H. (b) In contrast, a stronger winter monsoon in the southern ES blocks inflow transport from the Pacific to the ES to yield a lower (blue) ES sea level during Period L.

4. East Sea meridional overturning circulation

4.1. Introduction

The ES is a small, semi-enclosed deep basin (> 3,000 m) consisting of three basins, namely the UB, JB, and YB in the northwest Pacific (Figure 4.1). The severe ventilation in this almost isolated deep basin and its temporal changes are correlated with the variability in the intensity and structure of its own MOC (hereafter referred to as the ES MOC). Furthermore, the ES MOC and its variability make critical contributions to the regional climate and ecosystem variability through the distribution of heat, buoyancy, and dissolved matter, and have implications for the global MOC as a “miniature ocean” (Ichiye, 1984; Kim et al., 2002; Talley et al., 2003). However, the ES MOC and its variability remain largely unexplored, with only a small number of previous studies having addressed the formation and characteristics of deep water and both intermediate and deep circulations in the ES, and even fewer having investigated the ES MOC.

The overall structures and characteristics of the ES water masses and their changes have been observed and investigated over many decades (e.g., Miyazaki, 1953; Moriyasu, 1972; Kim and Chung, 1984; Kim and Kim, 1999; Kim et al., 2004; Talley et al., 2006; Chang et al., 2016; Yoon et al., 2018). The ES has an inlet and outlet system in which the inflow transports warm and saline water, named the Tsushima Warm Water (TWW), into the sea through the KS. This is generally balanced by outflows through the TS and SS (Figure 4.1). Therefore, upper circulation patterns are generated by this system (Cho et al., 2009). In the western ES, the East Sea Intermediate Water (ESIW) or North Korea Cold Water (NKCW), characterized by a vertical salinity minimum (Kim and Chung, 1984; Kim and Kim, 1999; Kim et al., 2004; Talley et al., 2006; Chang et al., 2016; Nam et al., 2016), has been found at an intermediate layer, e.g., depth of a couple to a few hundred meters, as confirmed by hydrographic observations. Below the ESIW, three deep-water masses have been identified from hydrographic observations, particularly in the northern JB according to, e.g., Kim et al. (2004). A distinct deep salinity minimum located at approximately 1,500 m divides the Central Water (CW) above and the Deep Water (DW) below the layer. The abyssal layer is occupied by the Bottom Water (BW), identified by a vertically homogeneous layer (Kim et al., 2004; Talley et al., 2006; Chang et al., 2016; Yoon et al., 2018).

The properties, formations, volumes, and spatial distributions of these water masses demonstrate strong temporal variability on decadal, interannual, and annual time scales. In detail, 1) the ESIW forms every winter as a mixed layer water, subducted in the northwestern ES (area A in Figure 4.1) and transported toward the KS by the southward-flowing North Korea Cold Current (NKCC) (Cho and Kim, 1998; Kim and Kim, 1999; Yoshikawa et al., 1999; Yun et al., 2004; Kim et al., 2006; Min and Kim, 2006; Park and Lim, 2017); 2) decadal changes in the dense CW, DW, and BW formations occur via open-ocean convection and deep-slope convection in response to convective mixing, saline water transport, freshwater loss to atmosphere (evaporation minus precipitation), and sea ice formation that yield brine rejection (Noh and Jang, 1999; Kang et al., 2003; Talley et al., 2003; Kim et al., 2004; Cui and Senjyu, 2010; Yoon et al., 2018); and 3) decadal and interannual variability of the ESIW properties are apparent, associated with the Arctic Oscillation (AO), wintertime air–sea heat exchanges in the northern ES, and circulation in the southwestern ES (Cui and Senjyu, 2010; Tanaka, 2014; Nam et al., 2016). However, surprisingly few studies have addressed the ES MOC, and only a seasonal reversal of deep overturning circulation associated with wind-driven Ekman pumping and geothermal effects on 40-year mean ES MOC were suggested by numerical models (Yoshikawa et al., 1999; Park et al., 2013). Decadal changes in the ES MOC have not been examined, either from observations or by numerical modeling.

In chapter 4, it was attempted to address the mean structure and intensity of the ES MOC and its temporal changes, with emphasis on the decadal change, identified from relatively well-validated global reanalysis products in comparison with in-situ observations of the ES. The data and methods are described in Section 4.2, and the results and discussion are presented in Sections 4.3 and 4.4, respectively. The summary and conclusion are given in Section 4.5.

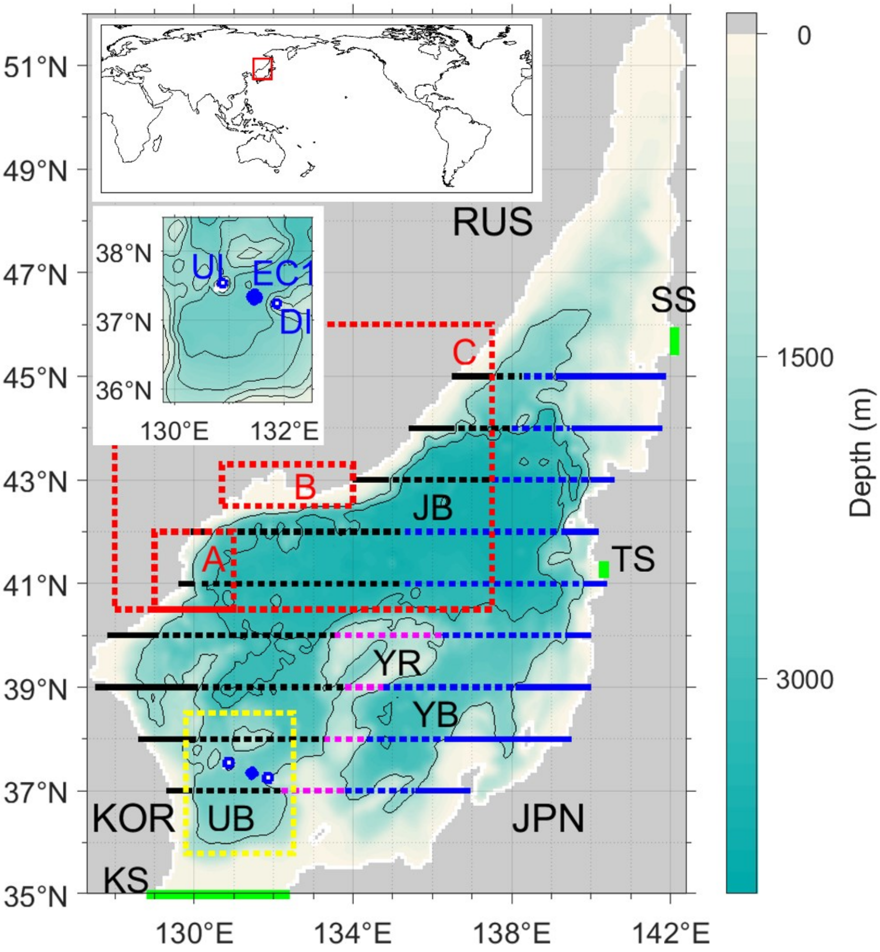

Figure 4.1 Bathymetry of the ES with color scale on right (contour interval: 1,500 m). KOR, JPN, and RUS denote Korea, Japan, and Russia, respectively, and UB, YB, YR, and JB indicate the Ulleung Basin, Yamato Basin, Yamato Ridge, and Japan Basin, respectively. KS, TS, and SS indicated by green lines represent the Korea/Tsushima Strait, Tsugaru Strait, and Soya Straits, respectively. Three selected areas, area A (129.0–131.0°E and 40.5–42.0°N), area B (130.7–134.0°E and 42.5–43.3°N), and area C (128.0–137.5°E and 40.5–46.0°N) are marked with red dashed boxes. The zonal sections at 37–45°N are separated into four or five subsections: western boundaries shallower than 1,500 m depth (black solid lines), western troughs deeper than 1,500 m (black dashed lines), middle ridges shallower than 1,500 m (magenta dashed lines), eastern troughs deeper than 1,500 m (blue dashed lines), and eastern boundaries shallower than 1,500 m (blue solid lines). The red rectangle in the upper world map denotes the study area. The UB area marked with a yellow dashed box is zoomed-in in the upper left corner with bathymetry (contour interval: 500 m), and the names of islands and mooring (UI: Ulleung Island, EC1: East Sea Current Measurement 1 mooring, DI: Dok Island).

4.2. Data and Methods

4.2.1. Data sources

The Hybrid Coordinate Ocean Model (HYCOM) global reanalysis product (GLBb0.08), with Navy Coupled Ocean Data Assimilation (NCODA), has a horizontal resolution of 0.08° and employs a hybrid coordinate in which three vertical coordinates, namely, isobars (pressure), isopycnals (density), and sigma levels (terrain) are used simultaneously. In this study, the monthly mean original data on temperature, salinity, density, and horizontal current given by the HYCOM products in the ES were analysed (Figure 4.1) for the period 1993–2012. To estimate surface fluxes of heat, freshwater, buoyancy, and momentum (Ekman transport), the monthly mean data of the surface shortwave and longwave radiations, sensible and latent heat fluxes, evaporation, precipitation, and wind stress from the Modern-Era Retrospective analysis for Research and Applications, Version 2 (MERRA-2) were used.

To validate the HYCOM data, three types of in-situ observational data collected for the target period 1993–2012, namely, 1) ferry-mounted acoustic Doppler current profiler (ADCP) data collected across the KS between Busan, Korea, and Fukuoka, Japan; 2) serial hydrographic data collected bimonthly off the east coast of Korea; 3) deep current-meter data collected by the East Sea Current Measurement 1 (EC1 mooring) located at 131.5°E and 37.3°N between Ulleung Island (UI) and Dok Island (DI) were used, as well as by other moorings. All EC1 mooring data are available to the general public, as well as the science community (Noh and Nam, 2018). The volume transport across the KS (V_{obs}) was estimated from the ferry-based ADCP data for the period March 1997–December 2012

(Takikawa et al., 2005; Fukudome et al., 2010; Han et al., 2016) to compare with the HYCOM results. In addition, cross-sectional structures of water temperature and the temporal difference observed during serial hydrographic cruises along one of the zonal lines (37.90ºN) off the east coast of Korea were compared with those given by HYCOM. the deep-moored current-meter data collected at several depths ranging from 1,800–2,600 m in the UB, JB, and YB between 1993 and 2012 and those ranging from 2,000–2,400 m in the UB (Takematsu et al., 1999; Chang et al., 2002; Senjyu et al., 2005; Teague et al., 2005; Chang et al., 2009) were compared with corresponding HYCOM twenty-year mean currents. The EC1 moored meridional current data were spatially averaged from November 1996–December 2012, which were recorded at 1,400- and 2,200 m depths using single-depth current meters attached to the subsurface mooring (Chang et al., 2009) and these data were compared with the HYCOM meridional currents in the western trough of the Ulleung Interplain Gap (UIG) between UI and DI (Figure 4.1).

4.2.2. Methods

Zonal and meridional Ekman transports per unit width, within the surface Ekman layer (VT_{Ek_X} and VT_{Ek_Y}, $\mathrm{m}^2\ \mathrm{s}^{-1}$), were calculated from the meridional and zonal surface wind stresses using $VT_{Ek\_X} = \frac{\tau_y}{f\rho_0}$, $VT_{Ek\_Y} =-\frac{\tau_x}{f\rho_0}$ where τ_x ($\mathrm{N\ m}^{-2}$), τ_y ($\mathrm{N\ m}^{-2}$), $f = 2\Omega\sin\varphi$, Ω ($\approx 7.2921\times10^{-5}$ rad s^{-1}), φ, and ρ_0 ($\approx$ 1,025 $\mathrm{kg\ m}^{-3}$) denote the zonal and meridional wind stress, local Coriolis parameter, constant Earth rotation rate, latitude, and constant surface water density, respectively.

The meridional overturning streamfunction (Ψ) was estimated by zonally and vertically integrating the meridional current in a unit of Sv (1 Sv = 10^6 m^3 s^{-1}) (Cunningham and Marsh, 2010; Kamenkovich and Radko, 2011; Han et al., 2013), such that

$$\Psi(y,z,t) = \int_{z_{bot}(y)}^{z} \int_{x_e(y,z')}^{x_w(y,z')} v(x,y,z',t)\ dx\,dz'. \tag{5}$$

Here, the meridional current v at longitude x, latitude y, depth z, and time t was integrated from the zonal easternmost point x_e to the westernmost point x_w, and from the bottom (z_{bot}) to the corresponding depth (z).

The meridional overturning streamfunction (Ψ) was averaged over the total period (20 years) and the annual mean at a location of shallow maximum temporal variance (1,000 m, 38.48°N, magenta square in Figure 4.5(a)) was used as an ES MOC index because it represents the characteristic of ES MOC. The years of negative (1996–2001 and 2010–2012) and positive (1993, 2002, and 2004–2009) phases of the ES MOC (when the absolute ES MOC index exceeded one-third standard deviation; 0.26) were selected for composite analysis and grouped into "Period I" and "Period II", respectively. The Ψ were averaged for the total 20-year period to estimate the time mean structure and intensity of the ES MOC, and their seasonal climatology with a clear annual cycle. For example, the mean seasonal change in the ES MOC was determined from the climatological mean ES MOC structures for the four seasons (winter: DJF; spring: MAM; summer: JJA; and fall: SON). More important, the ES MOC structures during the two periods (Periods I and II) were determined from the composite based on the ES MOC index. The Ψ were averaged vertically over the two periods and the longitudinal difference was compared at selected zonal sections along latitudes from 37° to 45°N in 1°

increments, and at subsections covering deep troughs and shallow ridges associated with the bathymetry, e.g., UB, JB, YB, Yamato Ridge (YR), and their connections (Figure 4.1).

Horizontal currents (u, v), where u and v denote the zonal and meridional components, respectively, were averaged over the two periods (I and II) and spatially over cross-sections of straits and selected zonal sections to allow a comparison of the ES MOC structures and associated volume transports. The horizontal currents at two different layers (intermediate and deep abyssal) were compared, where the intermediate and deep abyssal layers were defined as depths of 300 to 1,500 m and below 1,500 m, respectively. The reason for choosing these layers was to consider the shallow (~300 m) and deep (~1,500 m) salinity minima and reported vertical boundaries of water masses, namely ESIW, NKCW, CW, DW, and BW (Talley et al., 2003; Kim et al., 2004; Yoon et al., 2018). Note that the ESIW, NKCW, and CW primarily occupy the intermediate layer, whereas DW and BW occupy the deep abyssal layer.

4.3. Results

4.3.1. Validation of HYCOM

The net meridional volume transport in units of Sv (V_{mod}) at 35°N across the KS calculated from the HYCOM meridional current was validated against the net volume transport observed using the ferry-based ADCP (i.e., V_{obs}). The mean values and standard deviations of V_{mod} and V_{obs} over 190 months (March 1997 to December 2012) were consistent with each other at 2.59 ± 0.48 and 2.65 ± 0.47 Sv, respectively, yielding a significantly high (0.84) cross-correlation coefficient (black solid vs. red dashed lines in Figure 4.2). The difference (V_{mod} minus V_{obs}) had a time mean and standard deviation of −0.06 and 0.27 Sv, small enough compared with V_{mod} or V_{obs}, indicating that HYCOM effectively reproduced the net volume transport or inflow into the ES through the KS.

The cross-sectional structures of the water temperature averaged for the period January 1997–December 1999 (corresponding to Period I) and January 2007 to December 2009 (corresponding to Period II) given by HYCOM and obtained through serial hydrographic observations were consistent (although not highly correlated quantitatively). In particular, the temperature difference between two periods (late 2000s minus late 1990s) was also consistent, successfully reproducing shallower onshore and deeper offshore thermoclines during the late 1990s compared with the late 2000s (Figure 4.3). HYCOM successfully reproduced two different water masses observed in this cross-section: 1) cold (< 5 ºC) and fresh (absolute salinity < 34.22 g kg^{-1}) water located below the thermocline, and 2) warm (> 10 ºC) and saline (absolute salinity > 34.30 g kg^{-1}) water occupying the area between the onshore and offshore and around the thermocline. The former is known as the ESIW and is transported southward by the NKCC along the western boundary slope off the Korean Peninsula. The latter corresponds to the TWW, which is transported into the ES through the KS and advected northward by the western branch of the Tsushima Current or the East Korea Warm Current (EKWC) near the western boundary (east coast of the Korean Peninsula).

More interestingly, deep (~2,000 m) horizontal currents in the UB, JB, and YB derived from the HYCOM (black arrows in Figure 4.4a, b) agreed with the subsurface mooring measurements that have been reported previously (red arrows in Figures 4.4a, b; Takematsu et al., 1999; Chang et al., 2002; Senjyu et al., 2005; Teague et al., 2005; Chang et al., 2009). That is, the HYCOM results conformed to general cyclonic circulation in the basins at the deep and abyssal layer, as derived from observations from 1993 to 1996 (Takematsu et al., 1999), from 1999 to 2000 (Chang et al., 2002), from 1999 to 2000 (Senjyu et al., 2005), from 1999 to 2001 (Teague et al., 2005), and from 2002 to 2004 (Chang et al., 2009). The decadal change in the deep abyssal (~2,000 m) currents averaged over the western UIG (deep and abyssal inflow from JB into the UB, Figure 4.4b) derived from the HYCOM generally conformed to the values obtained by the subsurface mooring EC1 observations, indicating a slight intensification of the southward inflow into the UB (Figure 4.4c).

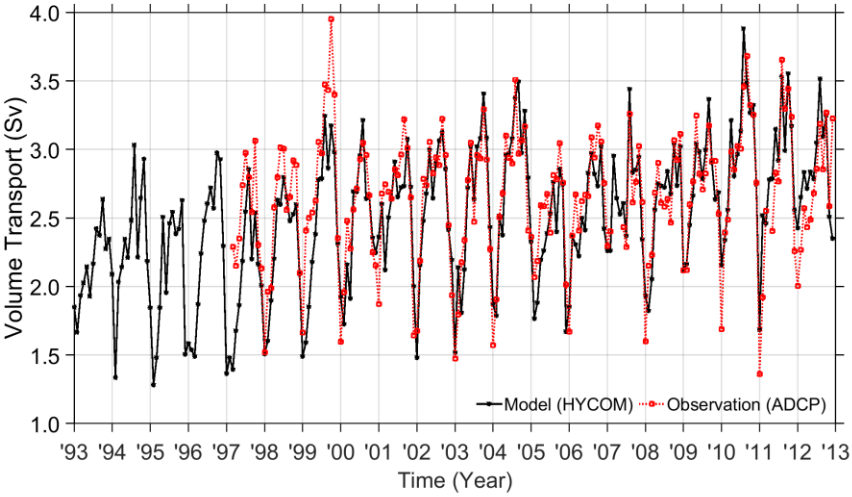

Figure 4.2 Time series of monthly mean volume transport through Korea/Tsushima Strait (KS; positive into ES) from model (black solid line, HYCOM reanalysis, 1993–2012) and observation (red dotted line, ADCP, 1997–2012).

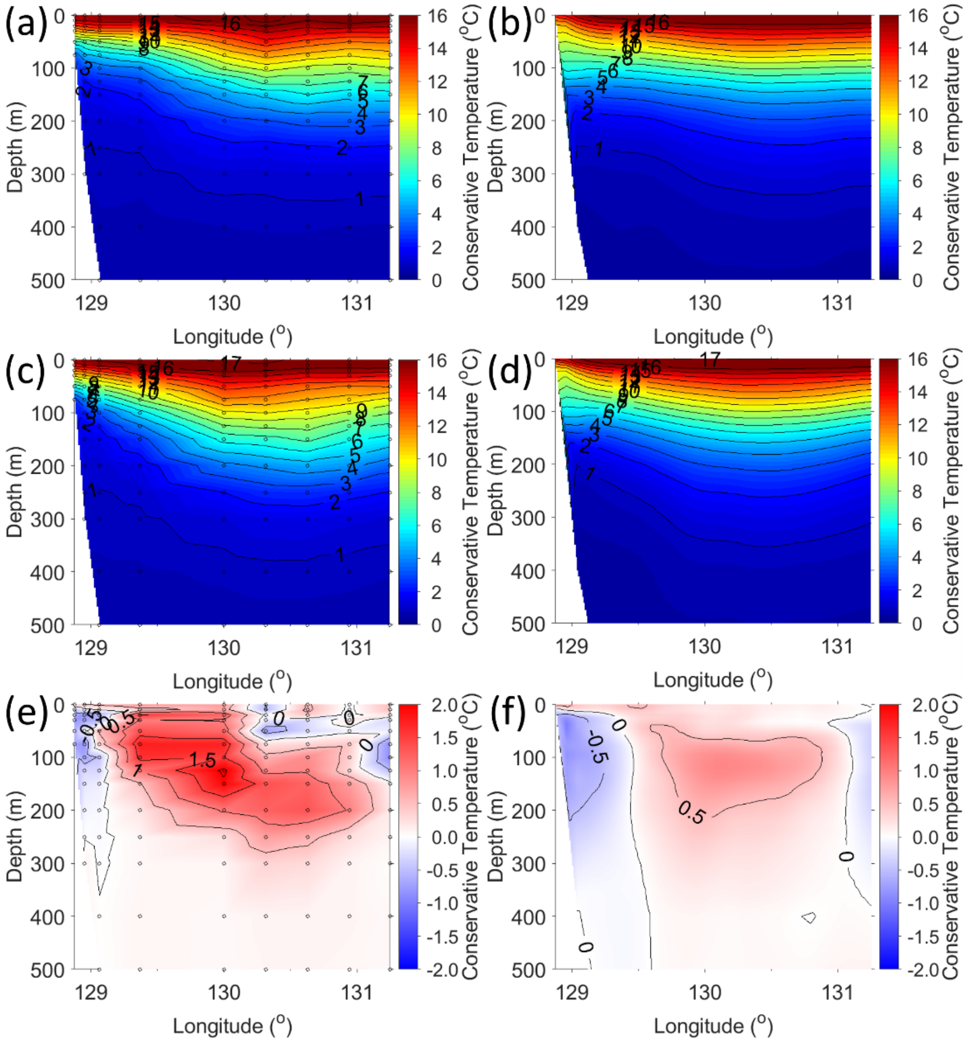

Figure 4.3 Cross-sectional structures of temperature along zonal line at 37.90°N in the southwest ES (contour interval: 1 ºC) averaged (a and b) from 1997 to 1999 in Period I and (c and d) from 2007 to 2009 in Period II, derived from (a and c) serial hydrographic observations and (b and d) HYCOM reanalysis. The differences are shown between the two periods from (e) observation (c-a) and (f) HYCOM (d-b).

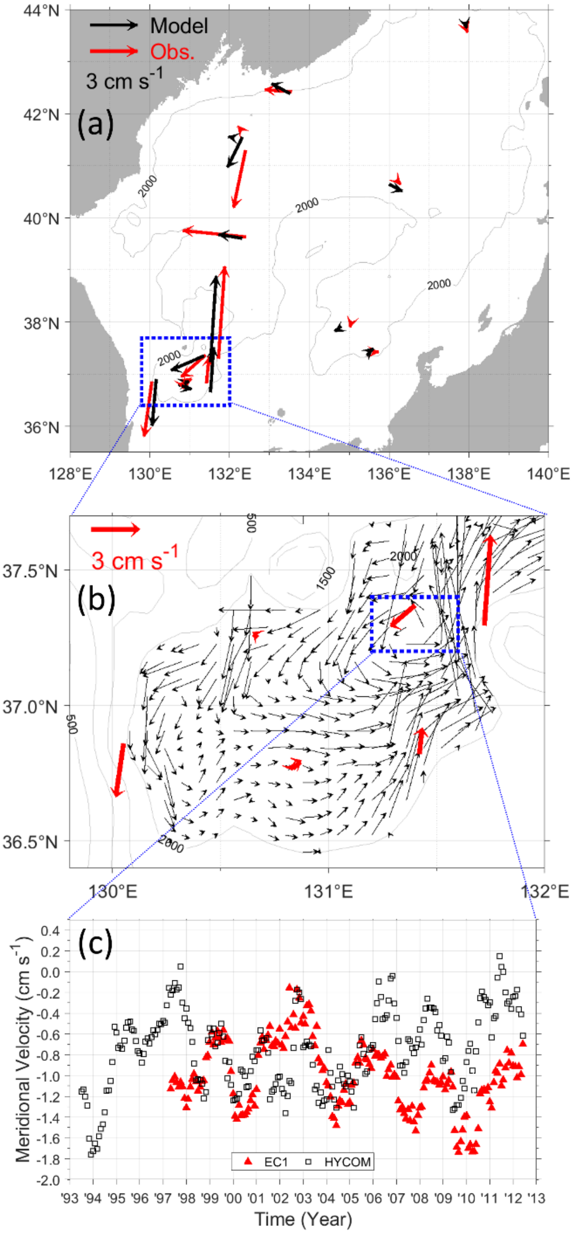

Figure 4.4 Mean horizontal currents derived from HYCOM (black arrows) and moored current-meter observations (red arrows) averaged over depth ranging (a) from 1,800–2,600 m in the ES, and (b) from 2,000–2,400 m in the UB (denoted by blue dotted box in a). The contour intervals for water depth in (a) and (b) are 2,000 and 500 m, respectively. Shown in (c), are the time series of thirteen month moving averaged meridional current derived from HYCOM (black squares) and observed at EC1 (red triangles).

4.3.2. Streamfunction

In the meridional section of the 20-year mean Ψ, anticyclonic overturning circulation occurred with $\Psi > 0$ (up- and downwelling in the south and north, respectively) at depths of < 700 m (upper layer), along with cyclonic overturning circulation with $\Psi < 0$ (down- and upwelling in the south and north, respectively) at depths > 700 m (lower layer) (Figure 4.5a). The minimum of the 20-year average Ψ for the lower layer was –0.29 *Sv* at 1,000 m and 39.28°N, whereas the maximum for the upper layer was 0.64 *Sv* at 400 m and 38.40°N. The two-cell MOC structure was maintained over seasons despite significant seasonal variations. The seasonal Ψ climatology (DJF, MAM, JJA, and SON) indicated that the minima in the lower layer were at 1,100 m with time-varying amplitude and latitude, yielding –0.19 Sv at 38.96°N, –0.45 Sv at 40.16°N, –0.29 Sv at 39.84°N, and –0.40 Sv at 38.96°N for DJF, MAM, JJA, and SON, respectively (not shown). The maxima in the upper layer were 0.71 *Sv* at 500 m and 38.40°N, 0.64 *Sv* at 350 m and 37.44°N, 0.58 *Sv* at 400 m and 38.32°N, and 0.68 *Sv* at 400 m and 38.40°N in DJF, MAM, JJA, and SON, respectively (not shown). The northward flow (meridional volume transport) in the lower layer was largest (0.45 *Sv*) in MAM and smallest (0.19 *Sv*) in DJF, and the net southward flow (meridional volume transport) in the upper layer was largest (0.71 *Sv*) in DJF and smallest (0.58 *Sv*) in JJA. Despite the significant changes in the locations of the maximum and minimum Ψ over the seasons, the basic structure of the 20-year mean ES MOC was maintained with the two counter-rotating cells (not shown).

However, a fundamental change occurred in the ES MOC between Periods I (negative phase of ES MOC index including the late 1990s) and II (positive phase of ES MOC index including the 2000s), as revealed by a comparison of the corresponding Ψ structures (Figure 4.5d–f). During Period I, the two counter-rotating cells were intensified, with an anticyclonic shallow overturning circulation at depths < 700 m (upper cell) and a cyclonic deep overturning circulation at depths > 700 m (lower cell). In contrast, during Period II, anticyclonic overturning circulation prevailed at all depths and latitudes, yielding $\Psi > 0$ everywhere. One maximum Ψ value of +0.70 *Sv* at 400 m and 38.40°N was found, in addition to double-minimum Ψ values of –0.73 *Sv* at 1,100 m and 39.84°N and –0.60 *Sv* at 1,400 m and 41.52°N in the upper and lower layers during Period I (Figure 4.5e). During Period II, double-maximum Ψ values of +0.72 *Sv* at 500 m and 38.16°N and +0.51 *Sv* at 1,200 m and 40.88°N were found in both layers (Figure 4.5f).

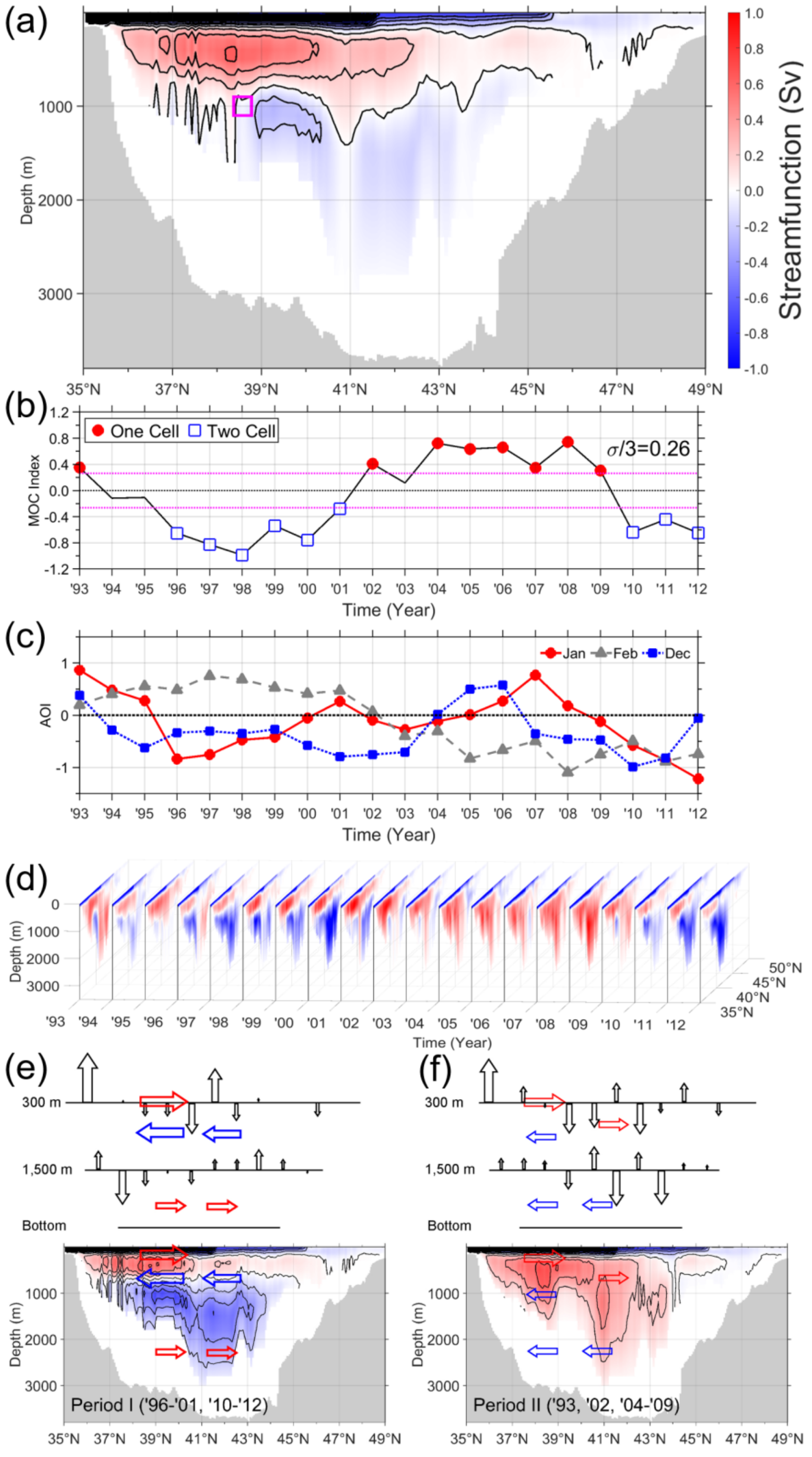
(a)
1000
2000
3000
Depth (m)
35°N
37°N
39°N
41°N
43°N
45°N
47°N
49°N
1.0
0.8
0.6
0.4
0.2
0.0
-0.2
-0.4
-0.6
-0.8
-1.0
Streamfunction (Sv)
(b)
One Cell
Two Cell
σ/3=0.26
MOC Index
1.2
0.8
0.4
0.0
-0.4
-0.8
-1.2
'93
'94
'95
'96
'97
'98
'99
'00
'01
'02
'03
'04
'05
'06
'07
'08
'09
'10
'11
'12
Time (Year)
(c)
Jan
Feb
Dec
AOI
1
0
-1
Time (Year)
(d)
0
1000
2000
3000
Depth (m)
50°N
45°N
40°N
35°N
Time (Year)
(e)
300 m
1,500 m
Bottom
Period I ('96-'01, '10-'12)
(f)
Period II ('93, '02, '04-'09)

Figure 4.5 (a) Twenty-year (1993–2012) mean meridional overturning streamfunction representing the ES MOC structures, as derived from HYCOM reanalysis. (b) ES MOC index from annual mean meridional overturning streamfunction at 1,000 m and 38.48°N (magenta square in (a)). Years of positive (1993, 2002, and 2004-2009, red filled circle) and negative (1996-2001 and 2010-2012, blue open square) phases of the ES MOC are classified as the absolute ES MOC index exceeds one third standard deviation, 0.26 (magenta lines). (c) Five-year moving averaged Arctic Oscillation (AO) Index in January (solid red circle), February (dashed gray triangle), and December (dotted blue square). (d) Time series of annual mean meridional overturning streamfunctions from 1993 to 2012. (e) Nine-year (1996–2001, 2010–2012) and (f) eight-year (1993, 2002, 2004-2009) mean meridional overturning streamfunctions in Periods I and II, respectively. In (e) and (f), the zonally integrated meridional transports are denoted by horizontal arrows, and upwelling/downwelling at two depths of 300 and 1,500 m are marked with vertical arrows, with the sizes of the latter being proportional to the volume transport. In (a), (e), and (f), the contour interval is 0.2 Sv.

4.3.3. Horizontal circulation

The following significant changes occurred between Periods I and II in the horizontal circulation in the intermediate layer (300–1,500 m): 1) A stronger southward current along the western boundary slope off the Korean Peninsula during Period I, i.e., the NKCC, which transports the ESIW (or NKCW) southward from the northwestern to southwestern ES, with amplitudes of the southward current (three blue rectangles such as NK1, 2, and 3 off the Korean Peninsula in Figure 4.6a, b) being 1.70, 2.41, and 2.86 cm s^{-1} during Period I vs. 0.49, 0.50, and 0.24 cm s^{-1} during Period II. 2) A stronger northward current along the Russian coast during Period I, with amplitudes of the northward current (three red rectangles such as RC1, 2, and 3 off the Russian coast in Figure 4.6a, b) being 0.93, 1.35, and 1.85 cm s^{-1} during Period I vs. 0.20, 0.93, and 0.46 cm s^{-1} during Period II. 3) Weaker anticyclonic circulation in the YB during Period I, with amplitudes of the vertical relative vorticity (red rectangle in the YB in Figure 4.6a, b) being 3.91×10^{-5} s^{-1} during Period I vs. 3.37×10^{-4} s^{-1} during Period II). 4) An opposite (cyclonic and anticyclonic circulations during Periods I and II) circulation in the UB (blue rectangle in the UB in Figure 4.6a, b). The most striking feature was that the strong southward-flowing NKCC along the western boundary slope in the intermediate layer during Period I, which roughly followed a 1,000-m isodepth horizontally, was not clear during Period II. This change was connected with markedly weakened or absent zonally integrated southward transport at the intermediate layer during Period II compared with Period I (Figure 4.5e, f).

In addition, the differences were found in the horizontal circulation between Periods I and II in the deep abyssal layer (> 1,500 m). That is, there were stronger cyclonic circulations in 1) UB, 2) JB, and 3) YB (blue rectangles in Figure 4.6c, d), and 4) stronger northward deep abyssal currents in the eastern UIG (previously called the Dokdo Abyssal Current or DAC) and along the eastern slope of the YB (named here the East Yamato Basin Abyssal Current or EYBAC) during Period I (red rectangles such as DA and EY in Figure 4.6c, d). The amplitudes of the vertical relative vorticity in the JB, UB, and YB were 8.47×10^{-4}, 8.67×10^{-4}, and 1.021×10^{-3} s^{-1}, respectively, during Period I vs. 4.43×10^{-4}, 5.09×10^{-4}, and 5.14×10^{-4} s^{-1}, respectively, during Period II (blue rectangles in Figure 4.6c, d). The northward-flowing DAC and EYBAC were stronger during Period I (5.43 and 3.37 cm s^{-1}) than during Period II (2.66 and 1.50 cm s^{-1}). These strong cyclonic circulations within the basins and the stronger northward currents along the eastern slope of the basins in the deep abyssal layer during Period I were much weakened during Period II.

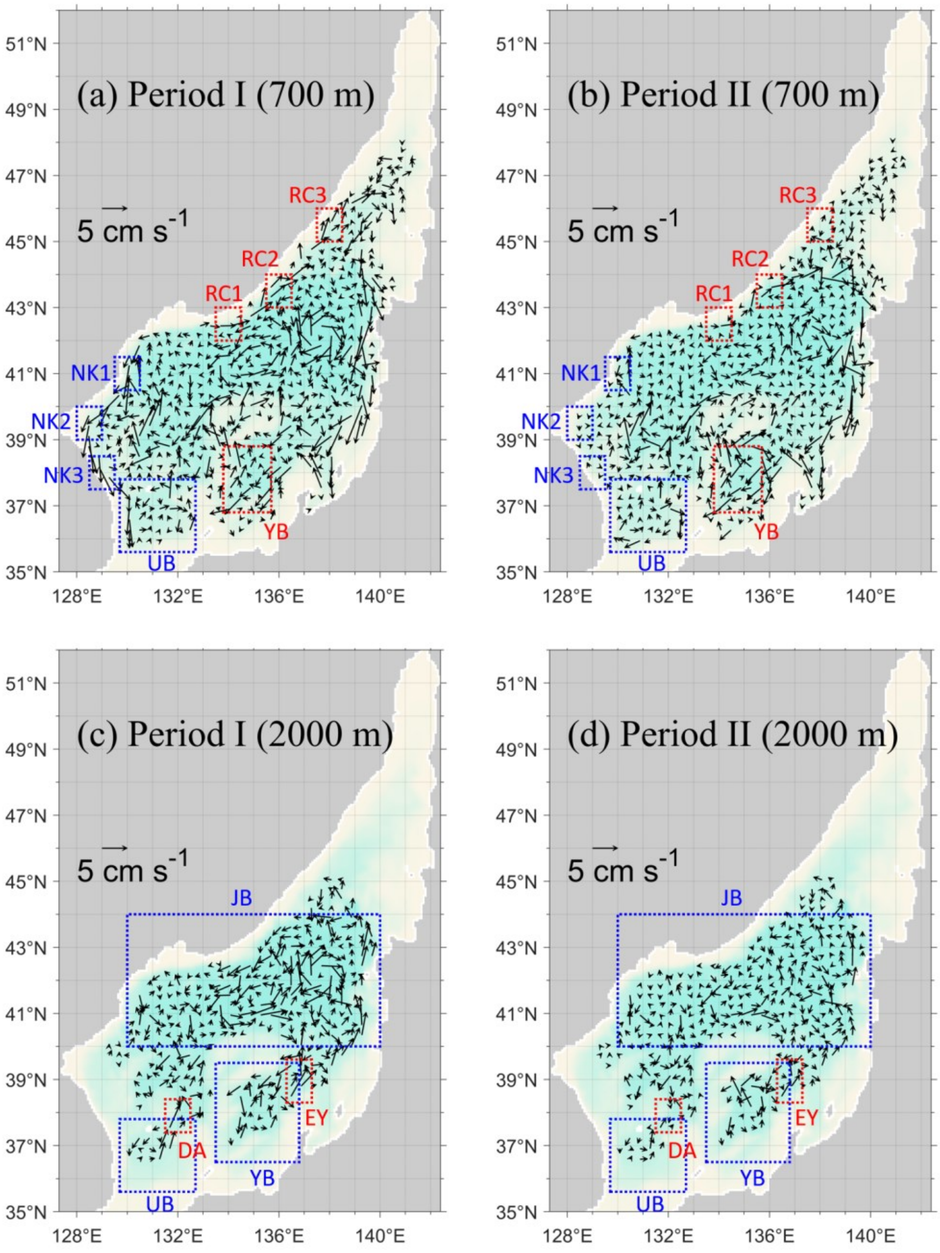

Figure 4.6 Horizontal currents given by HYCOM at (a, b) intermediate layer (700 m) and (c, d) deep abyssal layer (2,000 m), averaged over (a, c) Period I and (b, d) Period II. In (a, b) three sequential small blue (NK1, 2, 3) and red (RC1, 2, 3) dotted boxes represent the boundary current regions, and large blue and red boxes are UB and YB. Blue dotted boxes represent JB, UB, and YB anticlockwise from the top, and small red boxes (DA, EY) are deep abyssal currents such as DAC (left) and EYBAC (right) in (c, d). The pale-green background bathymetry is identical to that of Figure 4.1.

4.3.4. Net meridional and vertical volume transports

The net meridional volume transport in the intermediate layer was southward (negative) at all latitudes from 37° to 45°N during Period I and at latitudes 37°–40°N, 42°N, and 44°–45°N during Period II (Table 1). A significant decrease was found in amplitude or northward shift of the southward (negative) transport at the intermediate layer by 0.21 to 0.80 *Sv* from the difference during the two periods at latitudes 38–44°N (bold in Table 1). In contrast to this northward (positive) shift of meridional transport in the intermediate layer, there was a significant southward (negative) shift of meridional transport in the deep abyssal layer at latitudes 38–43°N from Period I to II (bold in Table 2). The northward vs. southward shifts of the meridional transport in the intermediate vs. deep abyssal layers during the two periods were consistent with the change caused by the two counter-rotating MOC cells during Period I to one MOC cell during Period II (Figure 4.5e vs. f).

Spatially coherent northward (southward) shifts of the intermediate (deep abyssal) transport from Period I to II, e.g., late 1990s vs. 2000s, were confirmed from those across the zonal subsections. In the intermediate layer, the meridional transport was generally negative (southward) at both the western and eastern subsections and positive (northward) in the central subsections, regardless of the period (Figure 4.7a, b). However, strong southward transport, with amplitudes ranging from 0.39–0.76 *Sv* in the western subsections (off the Korean Peninsula) during Period I, were found to be weakened significantly during Period II, having a typical amplitude equal to or less than 0.14 *Sv*. In contrast, those in the eastern subsections, and particularly the northeastern part or eastern JB, converted from southward during Period I to northward in Period II (Figure 4.7a, b). In addition, the down- and upwelling at 1,500 m in the southern (i.e., 37–41°N) and northern (i.e., 41–45°N) subsections, respectively, during Period I were weakened or reversed during Period II, except 42–43°N (symbols in Figure 4.7c, d). Most interestingly, southward shifts of the deep abyssal transport were found from increased southward transports or reversed transports from 38–43°N , i.e., at 38°N, from –0.03 to –0.18 *Sv* across the subsection connecting JB and UB; 39°N, from –0.03 to –0.22 *Sv* across the subsection connecting JB and UB, and from +0.38 to –0.08 *Sv* across the subsection connecting JB and YB; and 40°N, from +0.35 to –0.03 *Sv* and from +0.06 to –0.20 *Sv* (Figure 4.5e, f and Figure 4.7c, d).

Such contrasting northward and southward shifts of the meridional transport at the intermediate and deep abyssal layers from Period I to II were apparent from the annual time series of the three-year moving-averaged winter (JF) net meridional volume transport across the zonal section at 39°N, e.g., late 1990s vs. 2000s (shaded areas in Figure 4.8a). The winter net meridional transport across the zonal section at the intermediate layer remained southward, with only the amplitude decreasing from 1.03 *Sv* during the late 1990s (blue shaded) to 0.31 *Sv* during the 2000s (red shaded). However, the signs of those in the deep abyssal layer changed from positive (northward) to negative (southward) during the same period (Figure 4.8a).

Table 1 Net meridional volume transport in the intermediate layer (300−1,500 m) averaged over Periods I and II, and their differences (Period II−Period I) at 37°−45°N. Negative (southward) values are in italics and values in bold represent significant northward shifts from Period I to II.

300−1,500 m Latitude	Transport (Sv, Period I)	Transport (Sv, Period II)	Difference (Period II−Period I)
45°N	*−0.14*	*−0.20*	*−0.06*
44°N	*−0.25*	+0.11	**+0.36**
43°N	*−0.46*	+0.24	**+0.70**
42°N	*−0.78*	*−0.32*	**+0.46**
41°N	*−0.49*	+0.32	**+0.81**
40°N	*−0.70*	*−0.17*	**+0.53**
39°N	*−0.83*	*−0.30*	**+0.53**
38°N	*−0.80*	*−0.44*	**+0.36**
37°N	*−0.38*	*−0.39*	*−0.01*

Table 2 Similar to Table 1, but the data are for the deep abyssal layer (> 1,500 m). Positive (northward) values are in italics and values in bold represent significant southward shifts from Period I to II.

> 1,500 m Latitude	Transport (Sv, Period I)	Transport (Sv, Period II)	Difference (Period II–Period I)
45°N	–0.02	*+0.05*	*+0.07*
44°N	*+0.09*	*+0.12*	*+0.03*
43°N	*+0.33*	–0.28	**–0.61**
42°N	*+0.45*	–0.08	**–0.53**
41°N	*+0.56*	–0.50	**–1.06**
40°N	*+0.41*	–0.23	**–0.64**
39°N	*+0.37*	–0.30	**–0.67**
38°N	*+0.20*	–0.21	**–0.41**
37°N	–0.21	–0.13	*+0.08*

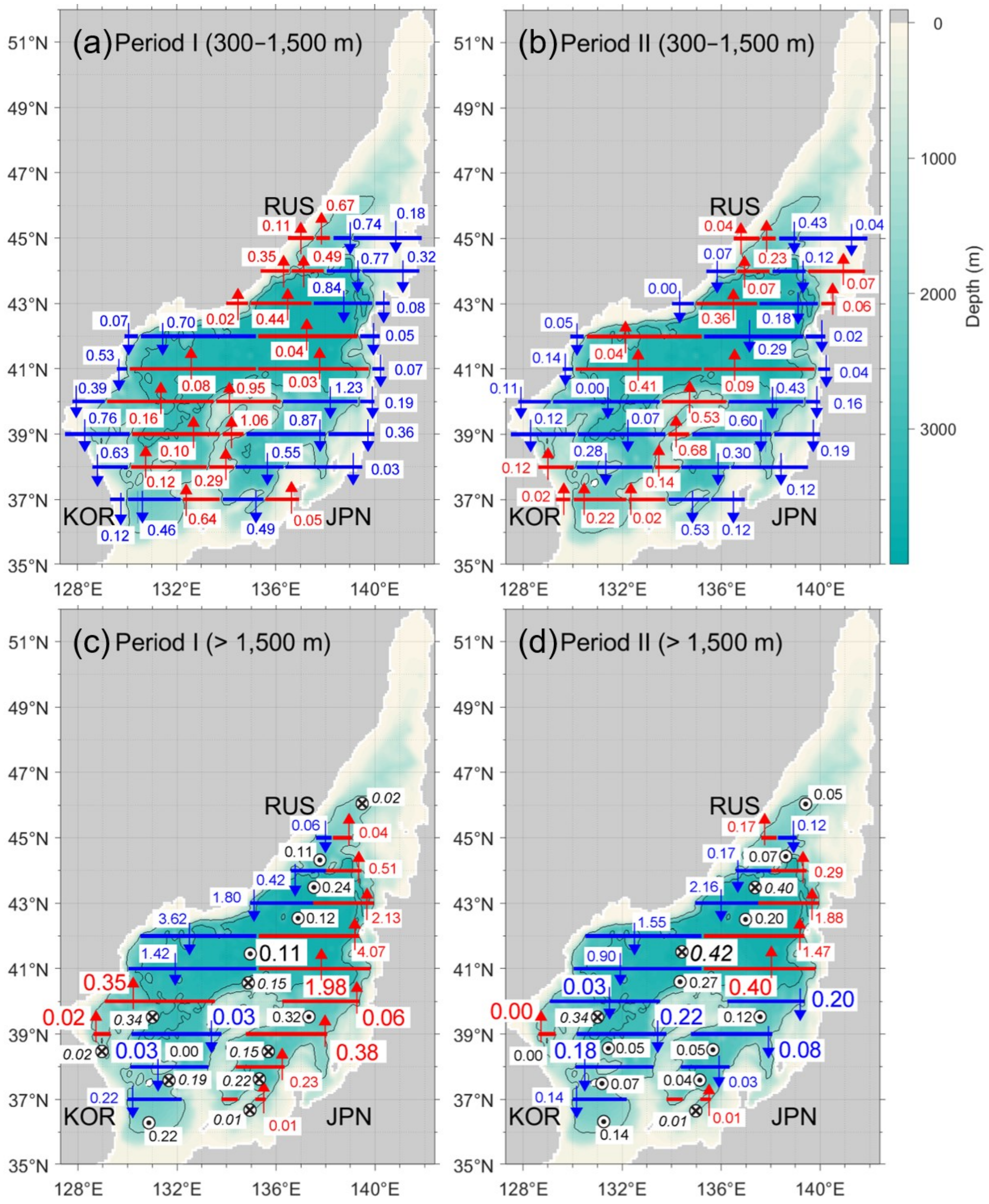
(a) Period I (300–1,500 m)

(b) Period II (300–1,500 m)

(c) Period I (> 1,500 m)

(d) Period II (> 1,500 m)

Figure 4.7 Schematics of meridional circulation (volume transport) in (a, b) intermediate (300–1,500 m), and (c, d) deep abyssal (below 1,500 m) layers in (a, c) Period I and (b, d) Period II. Red (blue) arrows represent northward (southward) transport, and black arrowhead (arrow tail) symbols with normal (italic) numbers denote upwelling (downwelling) at layer top at 1,500 m, respectively. The numbers indicate the net meridional volume transport in units of *Sv*.

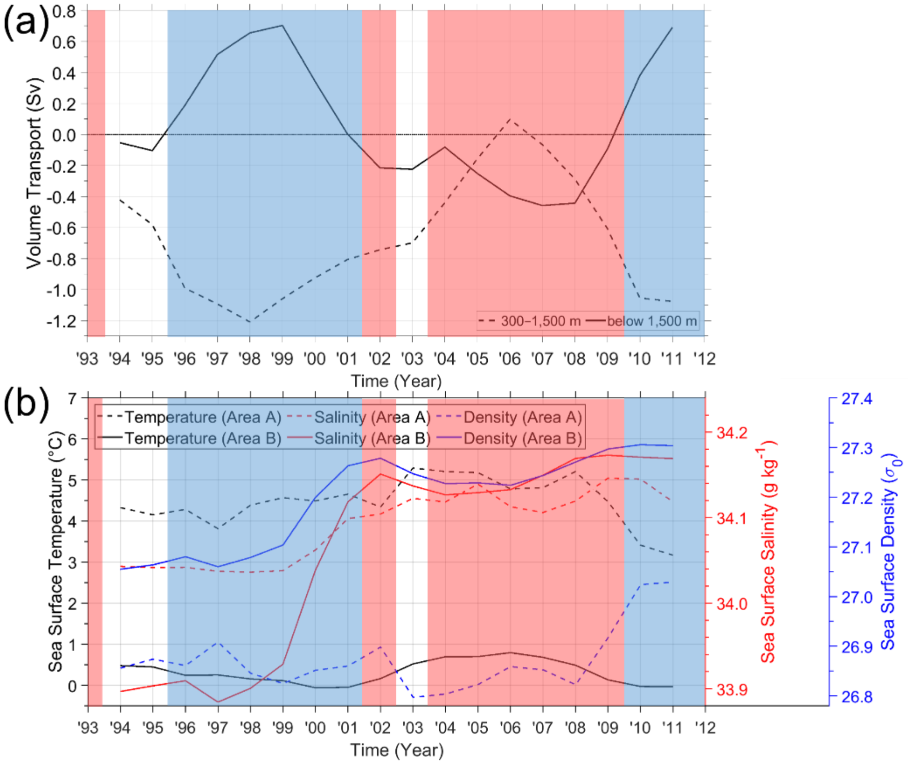

Figure 4.8 (a) Annual time series of three-year moving-averaged winter (JF) net meridional volume transport (*Sv*, positive northward) across zonal section at 39°N in the intermediate layer (between 300–1,500 m, black dashed) and deep abyssal layer (below 1,500 m, black solid) from 1994–2011. (b) Annual time series of three-year moving-averaged winter (JF) mean sea surface conservative temperature (°C, black), sea surface absolute salinity (g kg^{-1}, red), and sea surface potential density (in σ_0, blue) from 1994–2011, averaged over areas A (dashed lines) and B (solid lines) of Figure 4.1. Those in Periods I and II are shaded with light blue and red colors, respectively.

4.4. Discussion

The results of this study presented in the previous section indicated a considerable change in the ES MOC from the 20-year mean structure with two counter-rotating cells, consistent with the 40-year mean ES MOC reported previously (Park et al., 2013). The shallow and deep overturning circulations were intensified in the intermediate and deep abyssal layers during the late 1990s (Period I), yielding the counter-rotating two-cell structure that was closer to the 20-year mean ES MOC structure. Subsequently, the two-cell structure changed significantly to become a single full-depth overturning cell during the 2000s (Period II), which lasted to before the early 2010s, when it reverted to the two-cell structure. I noted that the intermediate and deep abyssal layers at 300–1,500 m and below 1,500 m, respectively, correspond to the shallow and deep salinity minima and known water boundaries (Kim and Chung, 1984; Kim and Kim, 1999; Kim et al., 2004; Talley et al., 2006; Chang et al., 2016; Nam et al., 2016; Yoon et al., 2018). This decadal change in ES MOC accompanied contrasting northward and southward shifts in the net meridional volume transport at the intermediate and deep abyssal layers from the late 1990s (Period I) to the 2000s (Period II), respectively. Although such decadal ES MOC changes have not been examined previously, a number of publications, discussed below, provide further support to our findings.

4.4.1. Intermediate layer (300–1,500 m)

Despite known difficulty in numerically reproducing the shallow salinity minimum in the southwestern ES (salinity minimum in the intermediate layer), HYCOM could successfully reproduce the shallow convection of the low-salinity intermediate water, i.e., ESIW, which has long been recognized from hydrographic observations (Kim and Chung, 1984; Kim and Yoon, 1999; Kim and Kim, 1999; Kim et al., 2004; Talley et al., 2006). In addition, HYCOM could reasonably simulate realistic intermediate circulation in the southwestern ES, yielding, e.g., decadal changes of ESIW properties associated with the AO (Cui and Senjyu, 2010; Tanaka, 2014; Nam et al., 2016). The formation, properties, volume, and distribution of the ESIW vary from year to year and over the decades, being influenced by the upper 500 m ocean circulation in the ES, as well as atmospheric forcing linked to AO (Kim et al., 2004; Teague et al., 2005; Chang et al., 2016; Nam et al., 2016; Park and Nam, 2018). This influence was particularly prominent in the western ES, where water formation processes, such as subduction and the footprint of shallow convection in the northwestern ES (area A in Figure 4.1) have been reported (Chang et al., 2016; Nam et al., 2016; Park and Lim, 2017). These likely had a major impact on the southward western boundary current at the intermediate layer, i.e., NKCC, off the Korean Peninsula and, therefore, the ES MOC. The cyclonic horizontal circulations in the intermediate layer reproduced by HYCOM, particularly during Period I (Figure 4.6a), are consistent with the observations made using Argo float trajectories between 1999 and 2010 (e.g., Figure 5 of Park et al. (2013)) and intermediate circulations derived from Argo float trajectories between 1998 and 2004 in the southwestern ES (e.g., Figure 4 of Park et al. (2004) and Figure 3 of Park et al. (2010)). Here, the results of ES MOC was discussed in relation to internal ES circulation at the intermediate layer and air–sea fluxes of heat, freshwater, buoyancy, and momentum.

The two-cell MOC structures during Period I imply enhanced shallow convection and more active ESIW formation in the northwestern ES (area A) than in Period II, or, in other words, the ESIW formation was likely less active during Period II (Figure 4.5e, f). Area A (centered at 130°E, 41.25°N) falls within an area where the SSS and depth of the salinity minimum layer reach their minima where the ESIW was formed (see Figure 3 of Park and Lim (2017)). In the early 2000s, the SST and SSS averaged over area A increased significantly by 0.76 °C (from 4.10 °C in the late 1990s to 4.86 °C in the 2000s) and 0.05 g kg^{-1} (from 34.07 g kg^{-1} in the late 1990s to 34.12 g kg^{-1} in the 2000s), respectively, yielding a sea surface density (SSD) decrease of 0.05 kg m^{-3} (in σ_0) for the decade from the late 1990s to the 2000s (Figure 4.8b).

Such decrease in surface density could be induced by either buoyancy gain from the atmosphere or changes in wind-driven upper ocean circulation or both. Cross-isopycnal mass flux estimated using the method used in Speer and Tziperman (1992) supported more active formation of the intermediate water (density ranging from 27.0 to 27.4 kg m^{-3}) in area A during Period I than during Period II. This indicates higher transformation primarily because of higher isothermal (rather than isohaline) volume flux and the larger surface area of water having a range of densities corresponding to the intermediate water (Figure 4.9a, b). Indeed, the surface heat flux anomaly averaged over area A changed from a negative phase during Period I to a positive phase during Period II. This resulted in buoyancy gain and a consequent decrease in SSD in the late 2000s primarily because of surface heat gain during the 2000s (Figure 4.9c and Figure 4.10a). The increased heat gain from the atmosphere into the ocean during Period II compared with Period I could be seen in an area wider than area A, with contrasting surface heat flux anomalies over the entire basins during the two periods. In addition to the surface heat flux, surface momentum flux affected the low SSD during the 2000s compared with the late 1990s, showing the increase in northward Ekman transport (vertical bars in Figure 4.10a) in the southwestern ES (UB, bigger rectangles in Figure 4.12c, d) because of stronger westward wind stress (or weaker eastward wind stress) (Figure 4.12c, d). The northward transport anomaly of warm TWW to the northwestern ES during the 2000s favored higher SST in the formation area (area A). Therefore, both air–sea buoyancy exchange and changes in wind-driven upper ocean circulation were responsible for the conditions unfavorable to active subduction and ESIW formation during the 2000s. This resulted in enhanced stratification, with warmer and lower-density surface water overlying colder and higher-density intermediate water in area A (Figure 4.9c).

The strong stratification in area A could stabilize the upper water column and reduce the ESIW formation during the 2000s (Period II), contrasting with active water transformation during the late 1990s (Period I). This behavior could also facilitate the weaker NKCC at the intermediate layer and northward shifts in the meridional transport at the layer during the 2000s (Figure 4.6a vs. b). This decreased the southward intermediate transport across 39°N significantly (0.72 *Sv*) from −1.03 *Sv* in the late 1990s to –0.31 *Sv* in the 2000s (dashed line in Figure 4.8a). It was noted that the NKCC transport at depths, particularly ranging from 300–700 m, near the western boundary decreased markedly by 0.62 *Sv* (from –0.69 *Sv* in the late 1990s to –0.07 *Sv* in the 2000s, not shown), which accounts for most changes in the meridional transport in the intermediate layer.

To date, no results identical to those obtained here have been reported for the decadal changes in ESIW formation in the northwestern ES. However, our findings were consistent with the water properties and transport and their temporal changes reported previously (Kim and Kim, 1999; Kim et al., 2004; Cui and Senjyu, 2010; Tanaka, 2014; Nam et al., 2016). In particular, Nam et al. (2016) suggest that the ESIW properties, volume, and distribution were connected primarily to the winter atmospheric conditions off the Russian coast in the northern ES and AO index over the decadal timescale. The decadal shift in the ES MOC index from the late 1990s to the 2000s covaries with the January AO index (shift from negative to positive phase, Figure 4.5c) among three winter AO indices (December, January, and February). This yielded correlation coefficients of 0.62 and 0.65 between the January AO index and the ES MOC index and between the January AO index and meridional intermediate transport, respectively. However, as also suggested by Nam et al. (2016), the upper ocean circulation in the southwestern ES can play an important role in ESIW formation, properties, volume, and distribution at the interannual timescale. The greater EKWC transport and more volume of TWW transported into the northwestern ES by a weaker westerly wind (westward wind stress anomaly) in the UB combined with reduced ESIW formation could yield warmer (and more saline) ESIW, with reduced southward NKCC transport at the intermediate layer.

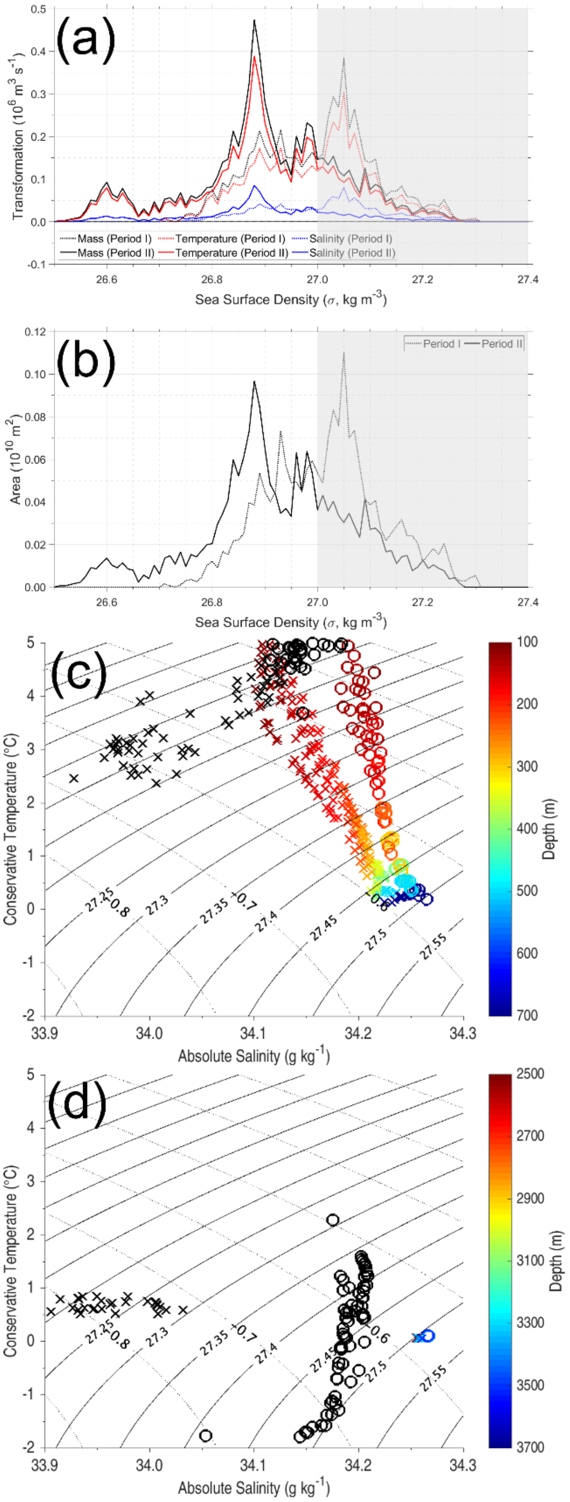
(a)
Transformation (10^6 m^3 s^{-1})
0.5
0.4
0.3
0.2
0.1
0.0
-0.1
Mass (Period I)
Temperature (Period I)
Salinity (Period I)
Mass (Period II)
Temperature (Period II)
Salinity (Period II)
26.6
26.8
27.0
27.2
27.4
Sea Surface Density (σ, kg m^{-3})
(b)
Area (10^{10} m^2)
0.12
0.10
0.08
0.06
0.04
0.02
0.00
Period I
Period II
Sea Surface Density (σ, kg m^{-3})
(c)
Conservative Temperature (°C)
Absolute Salinity (g kg^{-1})
33.9
34.0
34.1
34.2
34.3
27.25
27.3
27.35
27.4
27.45
27.5
27.55
0.8
0.7
Depth (m)
100
200
300
400
500
600
700
(d)
Conservative Temperature (°C)
Absolute Salinity (g kg^{-1})
0.6
Depth (m)
2500
2700
2900
3100
3300
3500
3700

Figure 4.9 (a) Cross-isopycnal mass flux (volume transport, $m^3 s^{-1}$) or transformation as a function of sea surface density (σ, kg m^{-3}) in area A in February (Speer and Tziperman, 1992). Plot of transformation of total (mass, black), thermal (temperature, red), and haline (salinity, blue) fluxes for Periods I (dotted line, two-cell) and II (solid line, one-cell). (b) Areas of each density class (interval of σ is 0.01 kg m^{-3}) in area A in February are plotted for Periods I (dotted line, two-cell) and II (solid line, one-cell). The densities of intermediate water are shaded with light gray in (a, b). TS properties of (c) sea surface water (black symbols) in area A and intermediate water (between 100–700 m, red to blue) in the area west of 128.72°E and at 39.00°N, and (d) sea surface water (black symbols) in area B and deep abyssal water (> 2,500 m, red to blue) in JB for Period I (February 1998; "X" symbols) and Period II (February 2008; "O" symbols), derived from HYCOM.

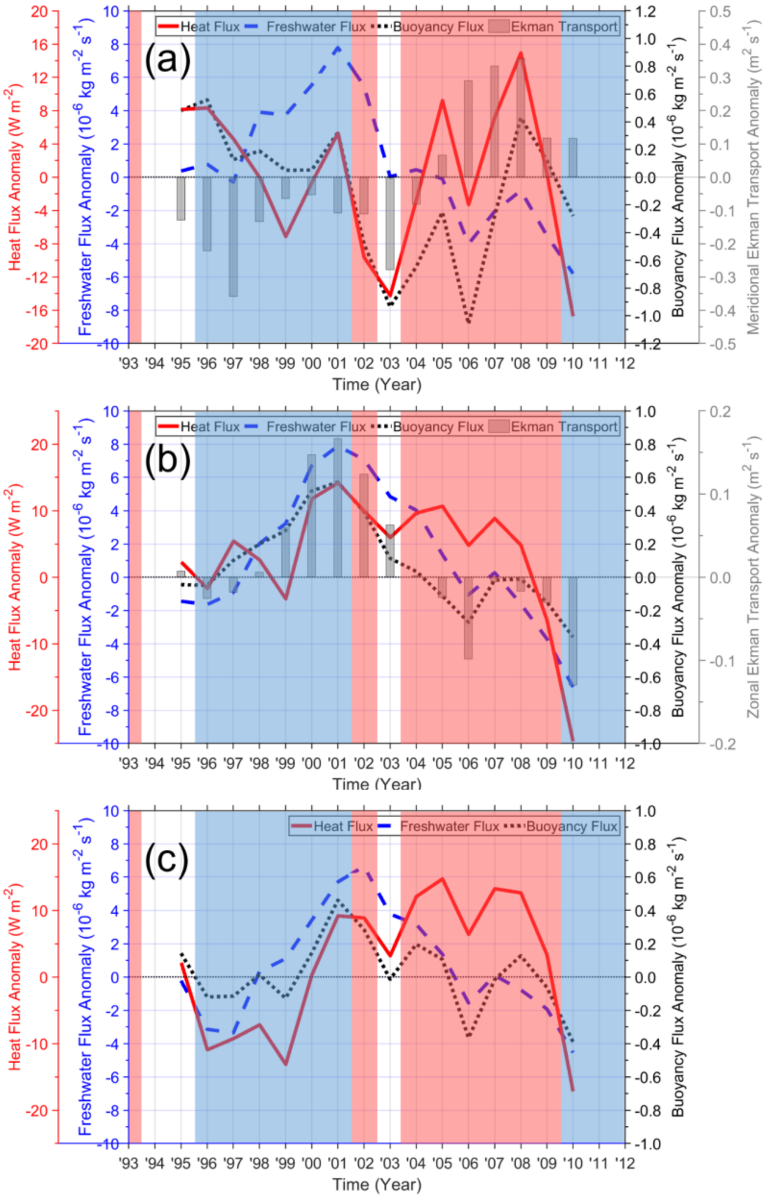

Figure 4.10 Time series of five-year moving averaged January surface net heat flux anomaly (left y-axis (W m^{-2}): a positive sign represents heat gain from the atmosphere into the ocean, red solid line), surface freshwater flux anomaly (left y-axis (kg m^{-2} s^{-1}): precipitation minus evaporation, which means that a positive sign represents freshwater gain from the atmosphere into the ocean, blue dashed line), and surface net buoyancy flux anomaly (right y-axis (kg m^{-2} s^{-1}): a positive sign represents buoyancy gain from the atmosphere into the ocean, black dotted line) in areas (a) A, (b) B, and (c) C, respectively. In (a) and (b), superimposed are (a) meridional and (b) zonal Ekman transport anomalies per unit width in (a) southwestern and (b) northeastern ES (right y-axis (m^{2}s^{-1}): a positive sign represents northward in (a) and eastward in (b), gray bar). Periods I and II are shaded by light blue and red colors, respectively.

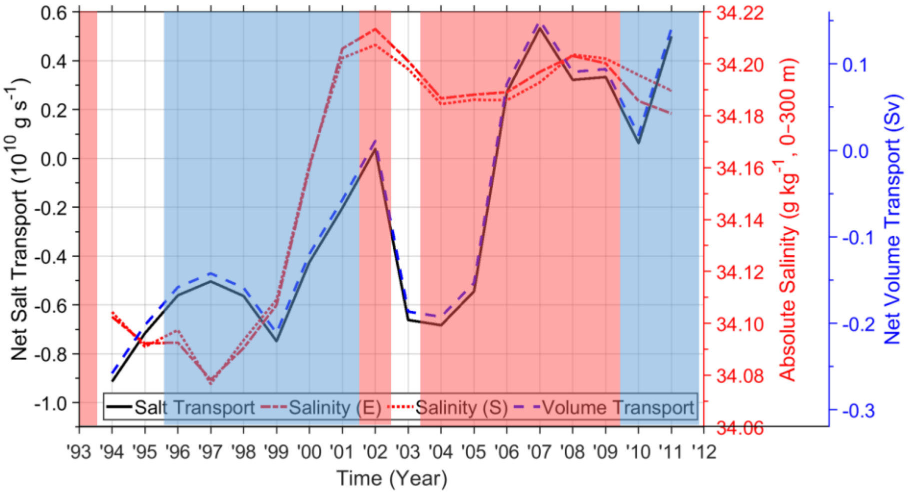

Figure 4.11 Time series of three-year mean January and February (horizontal and vertical) net salt transport (left y-axis (g s^{-1}) black solid line), salinity (right y-axis (g kg^{-1})) at upper 300 m of eastern (red dash dotted line) and southern (red dotted line) boundaries of area B, and net volume convergence into area B (right y-axis (*Sv*): blue dashed line). Periods I and II are shaded by light blue and red colors, respectively.

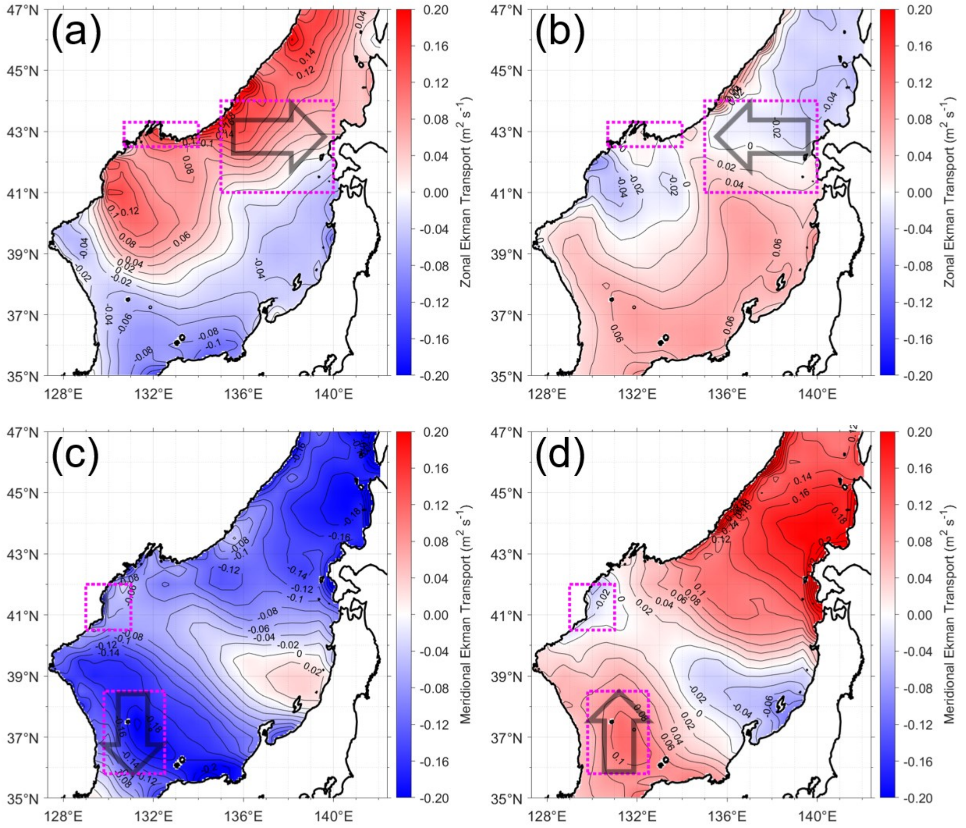

Figure 4.12 January mean (a, b) zonal and (c, d) meridional Ekman transport anomalies per unit width (m^2 s^{-1}: a positive sign represents eastward in (a, b) and northward in (c, d), respectively) for Periods I (a, c) and II (b, d). Area B and area in the northeastern ES for Ekman transport time series shown in Figure 4.10b (a, b), and Area A and area in the southwestern ES for Ekman transport time series shown in Figure 4.10a (c, d) are plotted with magenta lines. Black arrows represent the direction of Ekman transport.

4.4.2. Deep abyssal layer (> 1,500 m)

As regards the deep abyssal layer, it has been reported that the ES was severely ventilated down to the bottom as a result of surface atmospheric and oceanic conditions off the Russian coast in the northern ES (particularly at area B, Figure 4.1). This yields the highest levels of deep dissolved oxygen and lowest deep-water temperature in the Pacific (Kim et al., 2004; Talley et al., 2006). In particular, the BW has been suggested to be formed in area B during winter through deep-slope convection when the SSD (primarily salinity) increases because of brine rejection through sea ice formation, more evaporation minus precipitation, and more TWW transport into the formation area or area B (Noh and Jang, 1999; Kang et al., 2003; Talley et al., 2003; Kim et al., 2004; Cui and Senjyu, 2010; Yoon et al., 2018). Most recently, Yoon et al. (2018) have suggested that the formation of the deep water masses (CW, DW, and BW) and ventilation of the ES had experienced significant decadal changes in the early 2000s in relation to contrasting surface conditions off the Russian coast between the 1990s and 2000s. Such changes in deep ventilation could link to deep abyssal circulation and ES MOC, although these have not been reported despite several researchers suggesting dominant cyclonic abyssal circulations in JB, UB, and YB because of topographic control (Seung and Yoon, 1995; Chang et al., 2002; Senjyu et al., 2005; Seung, 2005; Yoon et al., 2005; Kim et al., 2008; Chang et al., 2016). Here, the results of decadal change in the ES MOC were discussed in relation to deep ventilation and deep abyssal circulation.

The ES MOC structures imply more BW formation through active deep-slope convection during Period II than during Period I in area B. The winter (JF) temperature, salinity, and density at the sea surface in area B increased by 0.07 °C from 0.45 to 0.52 °C, 0.14 g kg^{-1} from 34.01 to 34.15 g kg^{-1}, and 0.08 kg m^{-3} from 27.17 to 27.25 kg m^{-3}, respectively, during the early 2000s (Figure 4.8b, solid lines). This increase in the SSD primarily because of salinity increase (Figure 4.9d) is associated with both local atmospheric forcing and upper ocean circulation. More loss of surface buoyancy from ocean to atmosphere was found because of more evaporation minus precipitation during Period II in area B (Figure 4.10b, c). Therefore, the results indicated the importance of the regional air–sea freshwater (buoyancy) exchange on the BW formation, as also suggested previously (Kim et al., 2002; Talley et al., 2003; Yoon et al., 2018). Furthermore, horizontal salt convergence primarily because of volume convergence at the upper 300 m into area B increased from both the southern and the eastern cross-sections by 0.88×10^7 kg s^{-1} (-0.56×10^7 kg s^{-1} in the late 1990s to 0.32×10^7 kg s^{-1} in the 2000s), further supporting the increase in SSS and SSD in area B (Figure 4.11). This increased horizontal salt convergence into area B is related closely to the recirculation of saline TWW partly driven by westward Ekman transport (vertical bars in Figure 4.10b) because of the southward wind stress anomaly in the northeastern ES (bigger rectangles in Figure 4.12a, b).

These factors supported surface conditions that were favorable to more active deep-slope convection to activate the BW formation during Period II, yielding the SSD in area B as high (~27.5 g kg^{-1}) as that corresponding to the bottom water density (Figure 4.9d). In turn, this facilitated the weaker northward abyssal currents along the eastern slope boundaries of the UB and YB (DAC and EYBAC, respectively) that occurred during the 2000s or Period II (Figure 4.6c, d). Weaker northward abyssal currents linked to a southward shift from northward to southward transport over the decade from Period I to II were found in the deep abyssal layer across 39°N (Figure 4.8a, solid line). This shift can be explained mainly by considering the weakening of the two northward abyssal currents (DAC and EYBAC) that occurred during Period II (Figure 4.6c, d). The southward shift of the net meridional transport in the deep abyssal layer contributed to the ES MOC shift from two (shallow and deep) counter-rotating overturning cells during the late 1990s (Period I) to a single full-depth cell during the 2000s (Period II), along with the northward shift in the intermediate layer (Figure 4.5e, f). The more active deep-slope convection and enhanced BW formation because of increased SSS and SSD in area B during the 2000s were consistent with the southward shift in deep abyssal transport and the weakened DAC and EYBAC.

These decadal changes in BW formation in the northern ES have not been fully addressed to date, but some features on abyssal circulation and decadal changes in BW formation were consistent with previous findings (Yoshikawa et al., 1999; Kang et al., 2003; Talley et al., 2003; Kim et al., 2004; Senjyu et al., 2005; Cui and Senjyu, 2010; Yoon et al., 2018). Cyclonic abyssal circulations in the JB, UB, and YB, previously derived from moored current-meter observations, were consistent with the findings of the present study (Takematsu et al., 1999; Chang et al., 2004; Senjyu et al., 2005; Teague et al., 2005; Yoon et al., 2018). It was noted that a recent study by Yoon et al. (2018) came to similar conclusions with regard to the importance of both horizontal salt convergence at the upper ocean and air–sea freshwater exchange in modifying deep ES ventilation. Previous studies using hydrographic observations over the period 1969–1996 and a moving-boundary box model revealed markedly weakened ES ventilation from BW to CW, with reduced BW formation through deep-slope convection and greater CW formation through open-ocean convection in the mid-1990s (Kim et al., 2004). However, by incorporating hydrographic data collected over the recent decade, Yoon et al. (2018) revealed a slowdown in the deepening of the DW–BW boundary since the 2000s, which was associated with the re-initiation of BW formation through deep-slope convection in area B. Finally, the important role of local air–sea freshwater flux and horizontal salt convergence into area B in relation to the re-initiation of BW formation in the 2000s were also highlighted by Yoon et al. (2018), consistent with the results in this study.

4.5. Summary and Conclusion

Significant decadal changes have been shown in the strength and structure of the ES MOC using the 20-year HYCOM reanalysis data validated against in-situ observations of 1) net volume transport across the KS, 2) zonal cross-sectional structures of the water temperature off the western boundary, 3) deep abyssal circulation patterns, and 4) decadal changes in the deep meridional currents flowing from JB into UB. The results of the zonally integrated meridional volume transport indicate a 20-year-mean ES MOC structure having two counter-rotating overturning cells that consist of shallow-anticyclonic and deep-cyclonic overturning circulations, with upwelling in the south and downwelling in the north at the intermediate layer and vice versa in the deep abyssal layer, respectively (Figure 4.13 and Figure 4.14). More interestingly, significant decadal shifts in the ES MOC were found to discern two-cell and one-cell years (Period I, late 1990s vs. Period II, 2000s). That is, e.g., the ES MOC changed in the early 2000s from two counter-rotating cells (late 1990s) to a single full-depth cell (2000s) associated with a weakened southward NKCC (northward shift in net meridional volume transport) in the intermediate layer and weakened northward DAC and EYBAC (southward shift in net meridional volume transport) in the deep abyssal layer (Figure 4.14a vs. b). Further analysis suggested that the weakening of southward-flowing NKCC (northward-flowing DAC and EYBAC) and the northward (southward) shift in the net meridional volume transport in the intermediate (deep abyssal) layer during Period II were driven primarily by reduced ESIW (more BW) formation, with increased SST (increased SSS) in area A (area B) in the northwestern ES.

In conclusion, our results suggested that the ES MOC responded to both external atmospheric forcing and internal ES processes. The dominant internal forcing mechanism for the decadal ES MOC shift was wind-driven northward Ekman transport in the southwestern ES and horizontal salt convergence in the northwestern ES, associated with wind-driven westward Ekman transport and recirculation of TWW at the upper ocean in the northeastern ES. These factors provided a condition unfavorable to ESIW formation and favorable to BW formation during Period II. Such internal process could be enhanced further by water mass transformation and buoyancy gain from atmosphere to ocean (from ocean to atmosphere) at the surface in area A (area B) in the northwestern ES during Period II. This implies that area A (area B) was facilitated primarily by heat gain from (freshwater loss to) the atmosphere during Period II linked to the January AO. External forcing by the westward (southward) surface wind stress anomaly and the resultant northward (westward) anomaly in Ekman transport in the southwestern (northeastern) ES likely reinforced the upper ocean convergence of warm and saline TWW in the northwestern ES.

In this study, it has been shown that the ES MOC, horizontal recirculation of TWW, formations of intermediate and bottom waters in the northwestern ES, transport at the upper, intermediate, and deep abyssal layers in the ES, and air–sea fluxes of heat, freshwater, buoyancy, and momentum covary at a decadal timescale. However, our study did not allow determining which drives which, or whether other processes drive these. Given the importance of the ES MOC for transport of heat, salt, and volume, it is likely that feedback occurs between the external atmospheric forcing and internal circulation. Therefore, future numerical modeling study is necessary to address the feedback mechanisms, if any. Understanding how such feedbacks affect the decadal variability of the ES MOC has implications for the response of other marginal seas and the global ocean to future climate change.

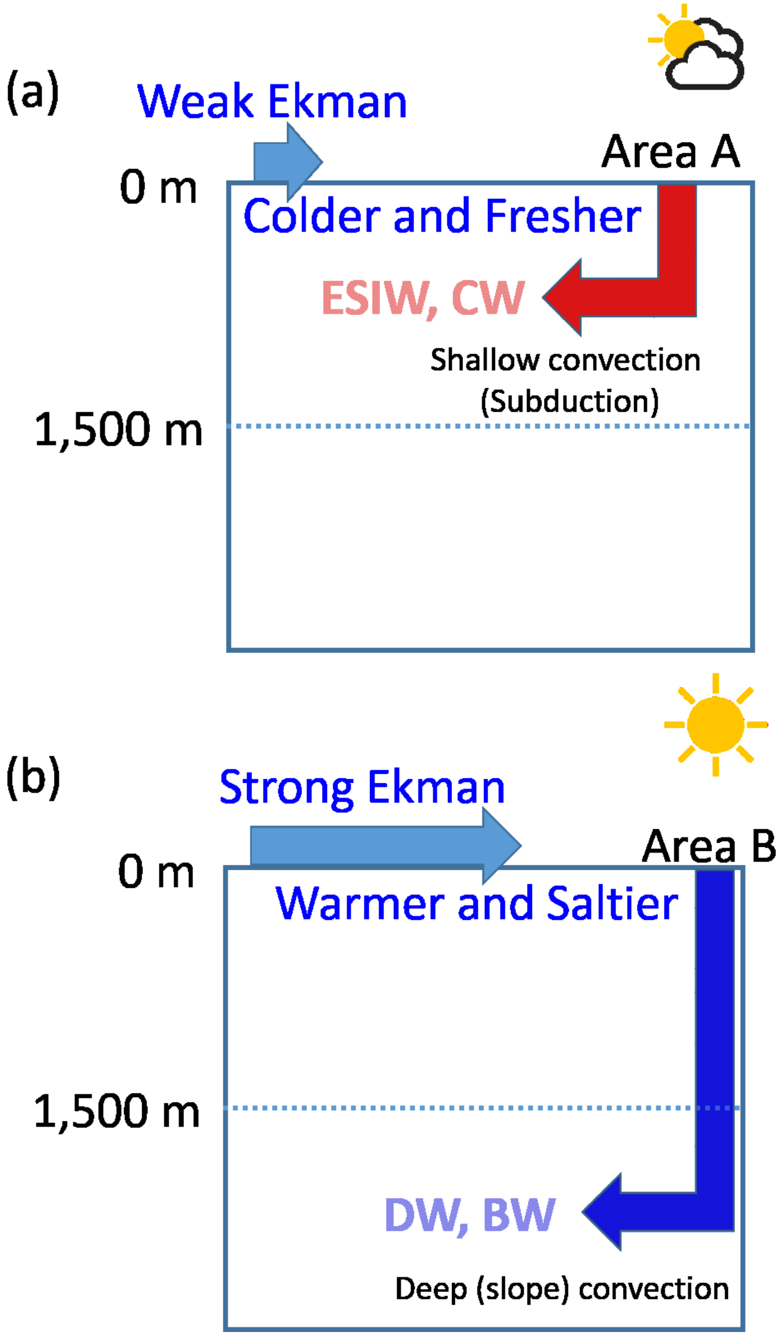

Figure 4.13 Schematic of ES MOC for (a) shallow convection (subduction) in Period I (two-cell years, late 1990s) and (b) deep (slope) convection in Period II (one-cell years, 2000s). (a) There were less evaporation minus precipitation and weak Ekman transport from the KS, TS, and/or SS and it made shallow convection (ESIW and CW) in Period I. (b) There were more evaporation minus precipitation and strong Ekman transport from the KS, TS, and/or SS and it made deep convection (DW and BW) in Period II.

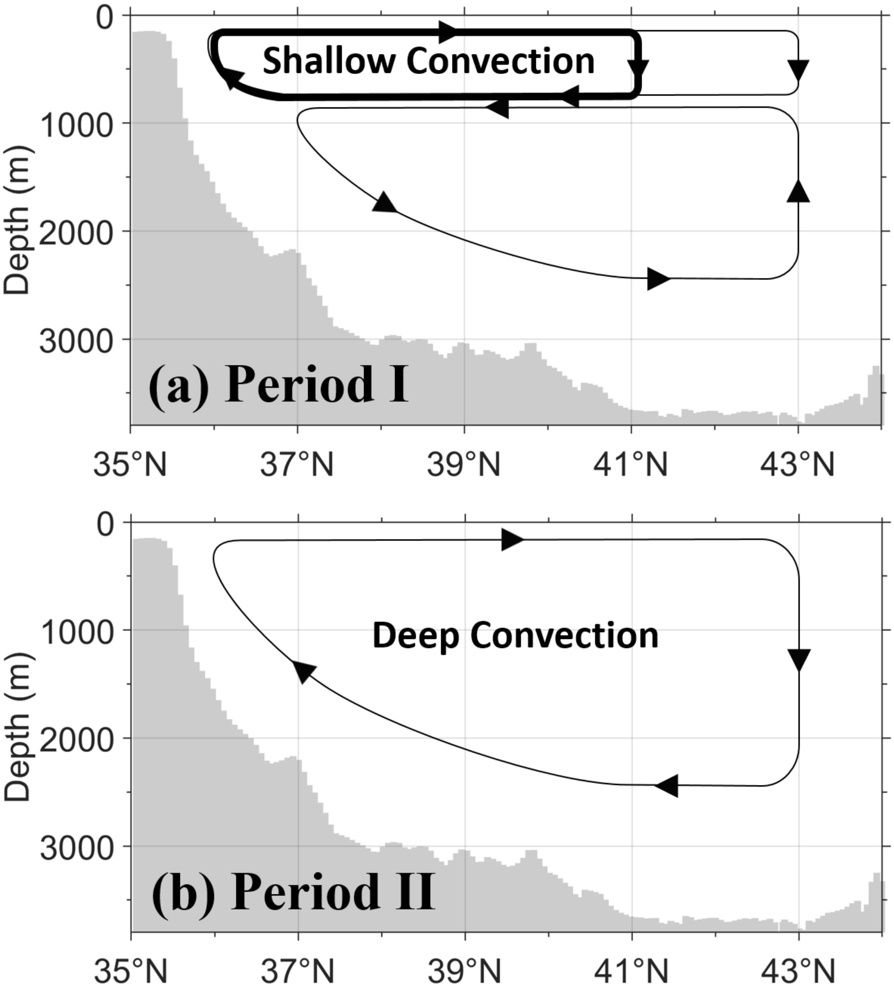

Figure 4.14 Schematic of ES MOC for (a) shallow convection (subduction) in Period I (two-cell years, late 1990s) and (b) deep (slope) convection in Period II (one-cell years, 2000s).

5. Discussion

Time series of four-year high pass filtered annual sea level anomaly and ES MOC index were plotted to examine the relationship between sea level and ES MOC. The correlation coefficient between four-year high pass filtered annual sea level anomaly and ES MOC index was -0.32 (p = 0.17) which is statistically insignificant (Figure 5.1). It might be assumed that shallow convection (subduction, negative ES MOC index) of relatively lower temperature and lower density (higher volume) water at area A compared to that at area B could increase sea level in the ES (Figure 5.1), even though the correlation coefficient is insignificant. The correlation coefficients between monthly mean sea level and monthly ES MOC index were -0.44 (p-value = 0.05) and -0.51 (p = 0.02) in March and August, respectively(Figure 5.2). The correlation coefficients between monthly mean sea level and monthly ES MOC index were insignificant in other months except March and August with 5% significance level. The variations of ES MOC and sea level are dominant in decadal and interannual variations, respectively. The relationships between the monthly ES MOC and the monthly sea level anomaly should be investigated more.

Time series of annual sea level anomaly and ES MOC index were compared to examine the relationship between them (Figure 5.3). The correlation coefficient between them (Figure 5.3a) was low (0.26, p-value = 0.27). However, the correlation between annual sea level anomaly and five-year lagged ES MOC index (Figure 5.3b) was significant with correlation coefficient (0.79, p-value < 0.01), although the data were not long enough. There may be a similar decadal variability between annual sea level anomaly and five-year lagged ES MOC. More northward volume transport with saltier water may induce high sea level in the same year and deep convection in 5 years. This assumption was analysed by calculating the correlation coefficient between annual sea level anomaly and volume transport anomaly in the KS. The correlation coefficients of annual sea level anomaly with volume transport of model (HYCOM) and observation (ADCP data) in the KS were 0.52 (p-value = 0.02) and 0.48 (p-value = 0.07), respectively (Figure 5.3c).

Consequently, the less northward volume transport with warmer water in the KS may result in the lower the sea level in the same year. Also, the less warm water in the northwest ES (area A) due to decrease of volume transport in the KS causes active shallow convection and negative ES MOC index with less surface net heat flux from the atmosphere to the ocean in 5 years (Figure 5.4a). On the contrary, the more northward volume transport in the KS may result in the higher the sea level. Also, more saline water advected by recirculation in the northwest ES (area B) due to increase of volume transport in the KS could cause deep convection and positive ES MOC index with more evaporation minus precipitation in 5 years (Figure 5.4b).

Yoon et al. (2018) analysed winter (DJF) heat and freshwater flux anomalies to investigate deep convection change in the ES. The heat and freshwater flux anomalies were negative in 1990s, which means more heat and freshwater from the atmosphere and the ocean. That could make warmer and fresher water in the northern ES, which was different to heat flux and similar to freshwater flux in area A in this study. The heat and freshwater flux anomalies were positive in 2000s, which means less heat and freshwater from the atmosphere and the ocean. That could make colder and saltier water in the northern ES, which was different to heat flux and similar to freshwater flux in area B in this study. SST and SSS were not observed SST and SSS, but estimated by heat and freshwater flux anomalies from the relationship with one-month flux-lead regression (Speer and Tziperman, 1992). The result was similar to the result above such as warmer and fresher water in the northern ES in 1990s and colder and saltier water in 2000s. Even though the results of heat flux of Yoon et al. (2018) were different to that in this study, the surface buoyancy flux and SSS in their study were similar to that in area B in this study such as less dense water in 1990s and denser water in 2000s. This difference could result from the uncertainty of the data based on the regression which they used.

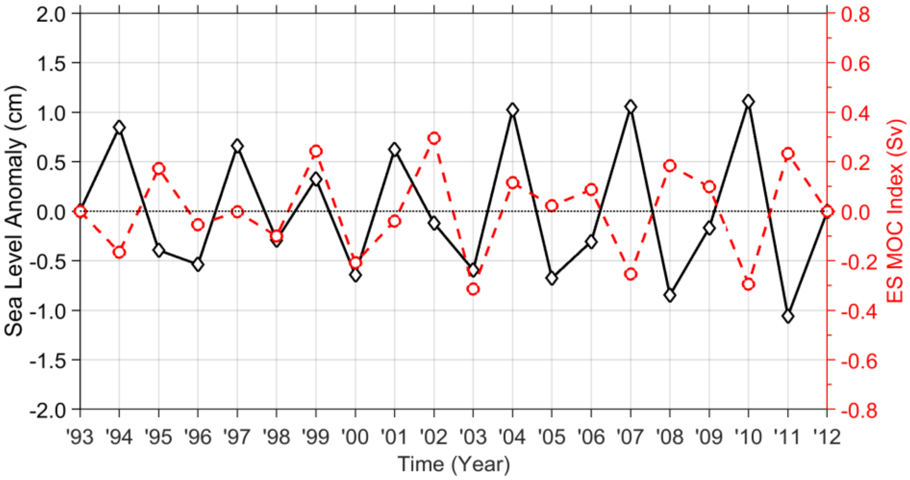

Figure 5.1 Time series of four-year high pass filtered annual sea level anomaly (black, left Y-axis) and four-year high pass filtered annual ES MOC index (red, right Y-axis). The correlation coefficient between them is -0.32 (p = 0.17).

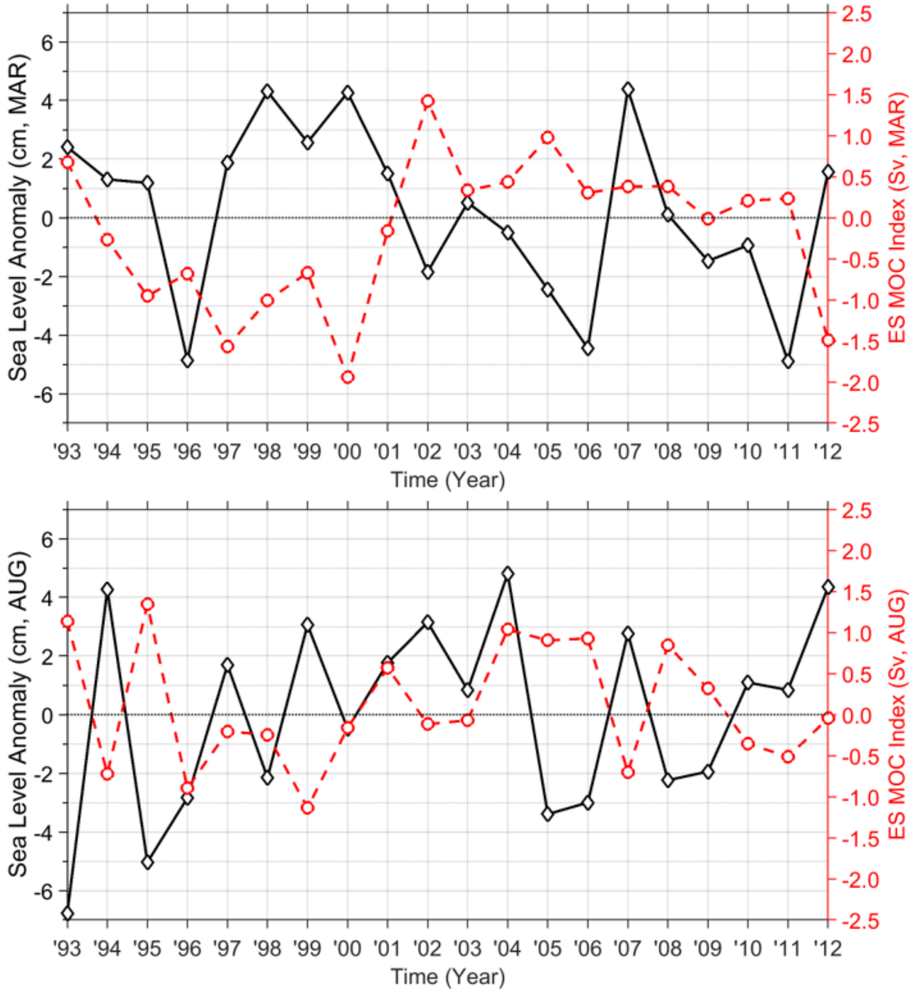

Figure 5.2 Time series of monthly sea level anomaly (black, left Y-axis) and monthly ES MOC index (red, right Y-axis) in (a) March and (b) August. The correlation coefficients between them are -0.44 (p-value = 0.05) and -0.51 (p = 0.02). The correlation coefficients between them in other months except March and August are insignificant with 5% significance level.

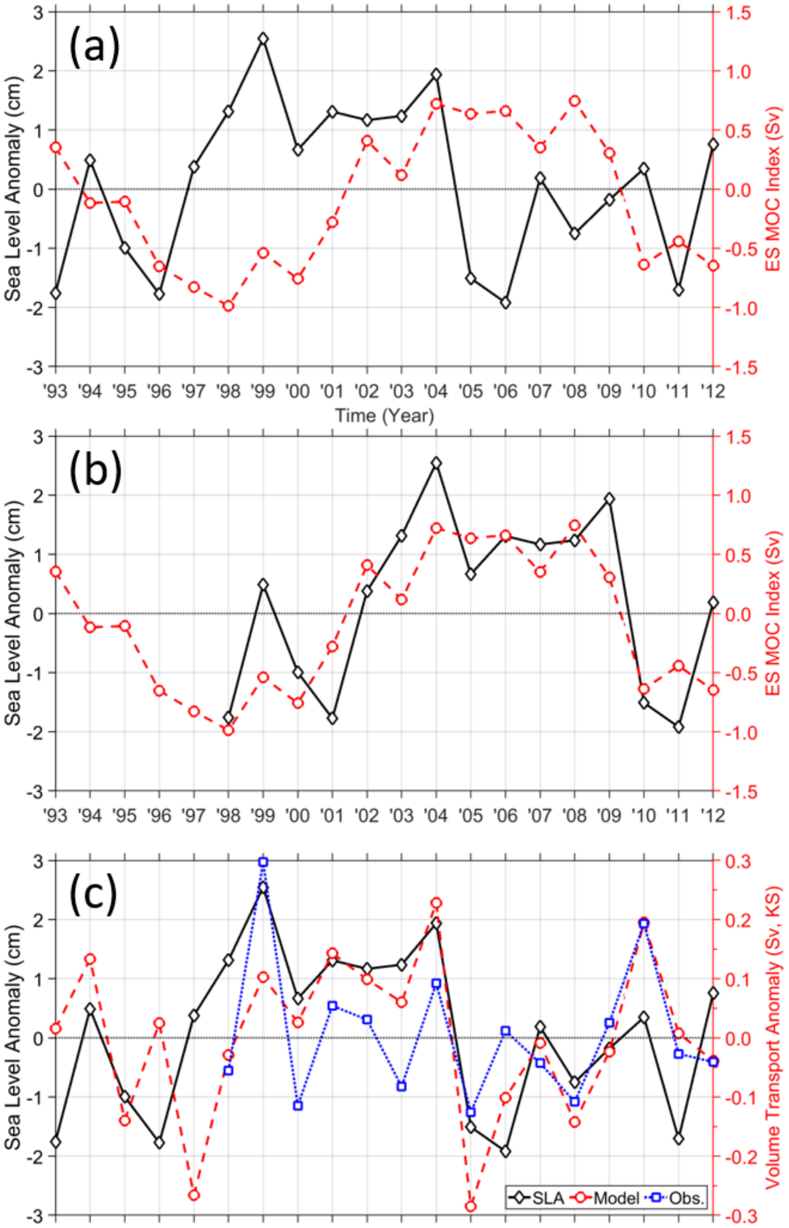

Figure 5.3 Time series of (a) annual sea level anomaly (black, left Y-axis), ES MOC index (red, right Y-axis), (b) five year delayed annual sea level anomaly (black, left Y-axis), ES MOC index (red, right Y-axis), (c) annual sea level anomaly (black, left Y-axis), and volume transport anomalies (Figure 4.2) of model (red, HYCOM, right Y-axis) and observation (blue, ADCP, right Y-axis) in the KS. The correlation coefficients between (a) annual sea level anomaly and ES MOC index, (b) five year delayed annual sea level anomaly and ES MOC index, and (c) annual sea level anomaly and volume transport anomalies of model and observation are -0.26 (p = 0.27), 0.79 (p < 0.01), 0.52 (p = 0.02), and 0.48 (p = 0.07).

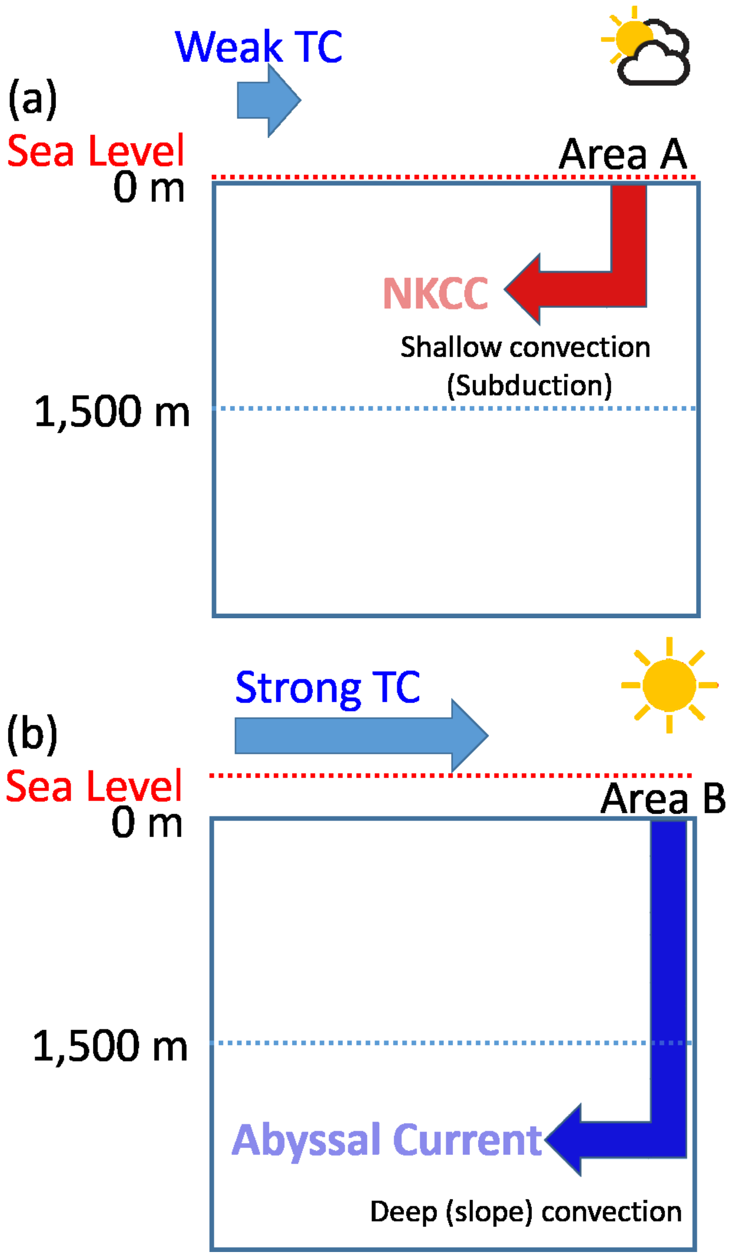

Figure 5.4 Schematics of sea level and MOC in the ES. (a) Shallow convection (subduction) makes NKCC and low sea level occurs when there are weak Tsushima Current (TC) from the KS, weak recirculation of TC from the TS and/or SS, and less surface net heat flux from the atmosphere to the ocean in area A. (b) Deep (slope) convection makes abyssal current and high sea level occurs when there are strong TC from the KS, strong recirculation of TC from the TS and/or SS, and more evaporation minus precipitation in area B. Sun and cloud in the figure are from Korea Meteorological Administration (https://www.weather.go.kr).

6. Summary and Conclusion

The variability of interannual sea level and the decadal change of ES MOC were investigated using satellite altimetry, tide-gauge, and reanalysis data in the ES. The sea level anomalies in summer (August) and winter (November and December) had good correlations with the Ekman transport driven by the wind stress. The decadal variability of ES MOC depended on atmospheric forcing and oceanic process in the northwest ES in winter.

Summer sea level from tide-gauge observation in the ES had an annual maximum for 26 years (1993-2018). The summer sea level from satellite altimetry data had larger rising rate than annual mean rate for 26 years (1993-2018). Its interannual variation was dominated by the wind stress in the south of ES which was caused by the atmospheric pressure gradient between KE and around Taiwan. The summer sea level in the ES was higher when the atmospheric pressure gradients were large, and it was lower when they were small. Thus, the summer sea level in the ES could be estimated using SESI which is the difference of atmospheric pressure anomalies between KE and around Taiwan.

The monthly mean wind stress from reanalysis data in the ES had a maximum in winter. The sea level anomaly from satellite altimetry data in winter had a maximum in 2016 and minimum in 2017 for 26 years from 1993 to 2018. The sea level in the ES could be explained by horizontal water convergence and divergence due to monsoonal wind-induced Ekman transport in winter. In high sea level years, the outflow decreases in the northeast ES but the inflow increases in the southern ES due to increased south-westward Ekman transport linked to enhanced south-eastward wind stress in the southern OS, and vice versa in the southern ES in low sea level years. Thus, the winter sea level in the ES also could be estimated using WESI which is defined by the difference of atmospheric pressure anomalies between the SS and east of Taiwan.

The distribution of atmospheric pressure could affect the number of Typhoons passed through the ES in summer, and it might affect the sea level in the ES also. The global climate disturbances such as the El Niño and La Niña, the eastward shift of atmospheric pressure distribution, and sea level change of open ocean near marginal seas could change the estimative skills of local index. Although the effects of the wind stress and atmospheric pressure on sea level were focused, other factors to change the marginal sea levels should be studied in the near future.

There were significant decadal changes in the strength and structure of the ES MOC for 20 years (1993–2012) from two counter-rotating overturning cells in the late 1990s to one full-depth anti-cyclonic overturning cell in the 2000s with reanalysis data. These ES MOC changes made northward shift of southward flow in the intermediate layer and southward shift of northward flow in the deep abyssal layer from the late 1990s to 2000s. Two overturning cells were made by shallow convection in the northwest ES due to colder SST in the late 1990s and one overturning cell was made by deep convection in the farther northwest ES with saltier SSS in 2000s. The atmospheric buoyancy (heat and freshwater) flux and Ekman transport by atmospheric momentum flux made these shallow and deep convections in the northwest ES along with northward surface flow in the south ES and westward ocean recirculation in the north ES.

In decadal interaction between sea level and ES MOC, less northward volume transport in the KS may cause lower sea level and colder SST in the northwest ES. On the contrary, more northward volume transport in the KS may generate higher sea level and saltier SSS in the farther northwest ES. The changes of the annual volume transport in the KS and the sea level in the ES were not in phase, but there was 5-year lag between them.

In this study, it has been shown that the variability of the ES such as sea level and MOC in the ES. Summer and winter sea level changes due to the Ekman transport by the wind stress in the south and north of the ES, respectively. ES MOC changed from two overturning cells to one full-depth cell because of atmospheric and oceanic processes. The decadal variability of volume transport in the KS could affect the decadal variability of sea level and ES MOC. Further investigations on the variability of sea level and the ES MOC changes as well as atmospheric, mass, and steric effects are necessary for better understanding of the ES system as a marginal sea and a miniature of ocean to future sea level rise and climate change.

References

Amiruddin, A., I. Haigh, M. Tsimplis, F. Calafat, and S. Dangendorf, 2015: The seasonal cycle and variability of sea level in the South China S ea. *Journal of Geophysical Research: Oceans*, **120,** 5490-5513, https://doi.org/10.1002/2015JC010923.

Baude, M., A. Colin, J. Duvernoy, A. Foussard, and C. Vailles, 2019: Key figures on climate. France, Europe and Worldwide.

Chang, K.-I., N. G. Hogg, M.-S. Suk, S.-K. Byun, Y.-G. Kim, and K. Kim, 2002: Mean flow and variability in the southwestern East Sea. *Deep Sea Research Part I: Oceanographic Research Papers*, **49,** 2261-2279, https://doi.org/10.1016/S0967-0637(02)00120-6.

Chang, K.-I., K. Kim, Y.-B. Kim, W. J. Teague, J. C. Lee, and J.-H. Lee, 2009: Deep flow and transport through the Ulleung Interplain Gap in the southwestern East/Japan Sea. *Deep Sea Research Part I: Oceanographic Research Papers*, **56,** 61-72, https://doi.org/10.1016/j.dsr.2008.07.015.

Chang, K.-I., C.-I. Zhang, C. Park, D.-J. Kang, S.-J. Ju, S.-H. Lee, and M. Wimbush, 2016: *Oceanography of the East Sea (Japan Sea).* Springer International Publishing.

Chang, K.-I., and Coauthors, 2004: Circulation and currents in the southwestern East/Japan Sea: Overview and review. *Progress in Oceanography*, **61,** 105-156, https://doi.org/10.1016/j.pocean.2004.06.005.

Cheney, R., L. Miller, R. Agreen, N. Doyle, and J. Lillibridge, 1994: TOPEX/POSEIDON: The 2-cm solution. *Journal of Geophysical Research: Oceans*, **99,** 24555-24563, https://doi.org/10.1029/94JC02050.

Cho, Y. K., and K. Kim, 1998: Structure of the Korea Strait Bottom Cold Water and its seasonal variation in 1991. *Continental Shelf Research*, **18,** 791-804, https://doi.org/10.1016/S0278-4343(98)00013-2.

Cho, Y. K., G. H. Seo, B. J. Choi, S. Kim, Y. G. Kim, Y. H. Youn, and E. P. Dever, 2009: Connectivity among straits of the northwest Pacific marginal seas. *Journal of Geophysical Research: Oceans*, **114**, https://doi.org/10.1029/2008JC005218.

Choi, B.-J., D. B. Haidvogel, and Y.-K. Cho, 2009: Interannual variation of the Polar Front in the Japan/East Sea from summertime hydrography and sea level data. *Journal of Marine Systems*, **78,** 351-362, https://doi.org/10.1016/j.jmarsys.2008.11.021.

CMEMS, 2020a: Copernicus Marine Environment Monitoring Service, Available at: http://marine.copernicus.eu [Cited 6th March 2020].

CMEMS, 2020b: Global ocean gridded L4 sea surface heights and derived variables reprocessed (1993-ongoing), Available at: http://marine.copernicus.eu/services-portfolio/access-to-products/?option=com_csw&view=details&product_id=SEALEVEL_GLO_PHY_L4_REP_OBSERVATIONS_008_047 [Cited 6th March 2020].

CMEMS_FTP, 2020: Availble online: ftp://my.cmems-du.eu/Core/SEALEVEL_GLO_PHY_L4_REP_OBSERVATIONS_008_047 (accessed on 04 March 2020).

CMEMS_portal, 2020: Availble online: http://marine.copernicus.eu/services-portfolio/access-to-products/?option=com_csw&view=details&product_id=SEALEVEL_GLO_PHY_L4_REP_OBSERVATIONS_008_047 (accessed on 04 March 2020).

CNES-CLS18, M., 2020: Availble online: https://www.aviso.altimetry.fr/en/data/products/auxiliary-products/mdt.html (accessed on 04 March 2020).

Cui, Y. L., and T. Senjyu, 2010: Interdecadal Oscillations in the Japan Sea Proper Water Related to the Arctic Oscillation. *Journal of Oceanography*, **66,** 337-348, https://doi.org/10.1007/s10872-010-0030-z.

Cunningham, S. A., and R. Marsh, 2010: Observing and modeling changes in the Atlantic MOC. *Wiley Interdisciplinary Reviews: Climate Change*, **1,** 180-191, https://doi.org/10.1002/wcc.22.

Fecher, T., R. Pail, T. Gruber, and G. Consortium, 2017: GOCO05c: a new combined gravity field model based on full normal equations and regionally varying weighting. *Surveys in geophysics*, **38,** 571-590, https://doi.org/10.1007/s10712-016-9406-y.

Fukudome, K., J. H. Yoon, A. Ostrovskii, T. Takikawa, and I. S. Han, 2010: Seasonal Volume Transport Variation in the Tsushima Warm Current through the Tsushima Straits from 10 Years of ADCP Observations. *Journal of Oceanography*, **66,** 539-551, https://doi.org/10.1007/s10872-010-0045-5.

Han, M., I. Kamenkovich, T. Radko, and W. E. Johns, 2013: Relationship between Air–Sea Density Flux and Isopycnal Meridional Overturning Circulation in a Warming Climate. *Journal of Climate*, **26,** 2683-2699, https://doi.org/10.1175/JCLI-D-11-00682.1.

Han, S., N. Hirose, N. Usui, and Y. Miyazawa, 2016: Multi-model ensemble estimation of volume transport through the straits of the East/Japan Sea. *Ocean Dynam*, **66,** 59-76, https://doi.org/10.1007/s10236-015-0896-9.

Holgate, S. J., and Coauthors, 2013: New data systems and products at the permanent service for mean sea level. *Journal of Coastal Research*, **29,** 493-504, https://doi.org/10.2112/JCOASTRES-D-12-00175.1.

Ichiye, T., 1984: Some problems of circulation and hydrography of the Japan Sea and the Tsushima Current. *Elsevier oceanography series*, Elsevier, 15-54.

Isobe, A., 1999: The Taiwan-Tsushima Warm Current System: Its path and the transformation of the water mass in the East China Sea. *Journal of oceanography*, **55,** 185-195, https://doi.org/10.1023/A:1007837912348.

Jhun, J.-G., and E.-J. Lee, 2004: A new East Asian winter monsoon index and associated characteristics of the winter monsoon. *Journal of Climate*, **17,** 711-726, https://doi.org/10.1175/1520-0442(2004)017<0711:ANEAWM>2.0.CO;2.

Kamenkovich, I., and T. Radko, 2011: Role of the Southern Ocean in setting the Atlantic stratification and meridional overturning circulation. *Journal of Marine Research*, **69,** 277-308, https://doi.org/10.1357/002224011798765286.

Kang, D. J., S. Park, Y. G. Kim, K. Kim, and K. R. Kim, 2003: A moving-boundary box model (MBBM) for oceans in change: An application to the East/Japan Sea. *Geophysical Research Letters*, **30**, https://doi.org/10.1029/2002GL016486.

Kang, S. K., J. Cherniawsky, M. Foreman, H. S. Min, C. H. Kim, and H. W. Kang, 2005: Patterns of recent sea level rise in the East/Japan Sea from satellite altimetry and in situ data. *Journal of Geophysical Research: Oceans*, **110**, https://doi.org/10.1029/2004JC002565.

Kim, C.-H., and J.-H. Yoon, 1999: A numerical modeling of the upper and the intermediate layer circulation in the East Sea. *Journal of Oceanography*, **55,** 327-345, https://doi.org/10.1023/A:1007837212219.

Kim, K., and J. Chung, 1984: On the salinity-minimum and dissolved oxygen-maximum layer in the East Sea (Sea of Japan). *Elsevier oceanography series*, Elsevier, 55-65.

Kim, K., K.-I. Chang, D.-J. Kang, Y. H. Kim, and J.-H. Lee, 2008: Review of recent findings on the water masses and circulation in the East Sea (Sea of Japan). *Journal of oceanography*, **64,** 721-735, https://doi.org/10.1007/s10872-008-0061-x.

Kim, K., K. R. Kim, Y. G. Kim, Y. K. Cho, D. J. Kang, M. Takematsu, and Y. Volkov, 2004: Water masses and decadal variability in the East Sea (Sea of Japan). *Progress in Oceanography*, **61,** 157-174, https://doi.org/10.1016/j.pocean.2004.06.003.

Kim, K. R., G. Kim, K. Kim, V. Lobanov, V. Ponomarev, and A. Salyuk, 2002: A sudden bottom-water formation during the severe winter 2000–2001: The case of the East/Japan Sea. *Geophysical Research Letters*, **29,** 75-71-75-74, https://doi.org/10.1029/2001GL014498.

Kim, Y.-G., and K. Kim, 1999: Intermediate waters in the East/Japan Sea. *Journal of Oceanography*, **55,** 123-132, https://doi.org/10.1023/A:1007877610531.

Kim, Y. H., Y. B. Kim, K. Kim, K. I. Chang, S. J. Lyu, Y. K. Cho, and W. J. Teague, 2006:

Seasonal variation of the Korea Strait Bottom Cold Water and its relation to the bottom current. *Geophysical Research Letters*, **33**, https://doi.org/10.1029/2006gl027625.

Kim, Y. S., C. J. Jang, and S.-W. Yeh, 2018: Recent surface cooling in the Yellow and East China Seas and the associated North Pacific climate regime shift. *Continental Shelf Research*, **156,** 43-54, https://doi.org/10.1016/j.csr.2018.01.009.

Li, Y., J. Zuo, Q. Lu, H. Zhang, and M. Chen, 2016: Impacts of wind forcing on sea level variations in the East China Sea: Local and remote effects. *Journal of Marine Systems*, **154,** 172-180, https://doi.org/10.1016/j.jmarsys.2015.10.009.

Liu, X., Y. Liu, L. Guo, Z. Rong, Y. Gu, and Y. Liu, 2010: Interannual changes of sea level in the two regions of East China Sea and different responses to ENSO. *Global and Planetary Change*, **72,** 215-226, https://doi.org/10.1016/j.gloplacha.2010.04.009.

Lyu, S. J., and K. Kim, 2005: Subinertial to interannual transport variations in the Korea Strait and their possible mechanisms. *Journal of Geophysical Research: Oceans*, **110**, https://doi.org/10.1029/2004JC002651.

Lyu, S. J., K. Kim, and H. T. Perkins, 2002: Atmospheric pressure-forced subinertial variations in the transport through the Korea Strait. *Geophysical Research Letters*, **29,** 8-1-8-4, https://doi.org/10.1029/2001GL014366.

Mangiarotti, S., and F. Lyard, 2008: Surface pressure and wind stress effects on sea level change estimations from TOPEX/Poseidon satellite altimetry in the Mediterranean Sea. *Journal of Atmospheric and Oceanic Technology*, **25,** 464-474, https://doi.org/10.1175/2006JTECHO419.1.

Marcos, M., M. N. Tsimplis, and F. M. Calafat, 2012: Inter-annual and decadal sea level variations in the north-western Pacific marginal seas. *Progress in oceanography*, **105,** 4-21.

Mayer-Guerr, T., and GOCO_Team, 2015: The combined satellite gravity field model GOCO05s. *EGU general assembly conference abstracts*.

Min, H. S., and C.-H. Kim, 2006: Water mass formation variability in the intermediate layer of the East Sea. *Ocean Science Journal*, **41,** 255-260, https://doi.org/10.1007/BF03020629.

Miyazaki, M., 1953: On the water masses of the Japan Sea. *Bull. Hokkaido Reg. Fish. Res. Lab.*, **7,** 1-65.

Moriyasu, S., 1972: The Tsushima Current. *Kuroshio: Its physical Aspects*, H. Stommel, K. Yoshida, Ed., University of Tokyo Press, 353-369.

Munk, W., 2003: Ocean freshening, sea level rising. *Science*, **300,** 2041-2043.

Nam, S., S. T. Yoon, J. H. Park, Y. H. Kim, and K. I. Chang, 2016: Distinct characteristics of the intermediate water observed off the east coast of Korea during two contrasting years. *J Geophys Res-Oceans*, **121,** 5050-5068, https://doi.org/10.1002/2015jc011593.

Nam, S. H., S. J. Lyu, Y. H. Kim, K. Kim, J. H. Park, and D. R. Watts, 2004: Correction of TOPEX/POSEIDON altimeter data for nonisostatic sea level response to atmospheric pressure in the Japan/East Sea. *Geophysical research letters*, **31**, https://doi.org/10.1029/2003GL018487.

Noh, S., and S. Nam, 2018: EC1, mooring time-series since 1996. *SEANOE*, https://doi.org/10.17882/58134.

Noh, Y., and C. Jang, 1999: Large eddy simulation of open ocean deep convection with application to the deep water formation in the East Sea (Japan Sea). *Journal of oceanography*, **55,** 347-367, https://doi.org/10.1023/A:1007889229058.

Noone, K. J., U. R. Sumaila, and R. J. Diaz, 2013: *Managing ocean environments in a changing climate: sustainability and economic perspectives.* Elsevier.

Ohshima, K. I., D. Simizu, N. Ebuchi, S. Morishima, and H. Kashiwase, 2017: Volume, heat, and salt transports through the Soya Strait and their seasonal and interannual variations. *Journal of Physical Oceanography*, **47,** 999-1019, https://doi.org/10.1175/JPO-D-16-0210.1.

Park, J., and B. Lim, 2017: A new perspective on origin of the East Sea Intermediate Water: Observations of Argo floats. *Progress in Oceanography*, https://doi.org/10.1016/j.pocean.2017.10.015.

Park, J., and S. Nam, 2018: Interannual variability of winter precipitation linked to upper ocean heat content off the east coast of Korea. *International Journal of Climatology*, **38,** e1266-e1273, https://doi.org/10.1002/joc.5354.

Park, Y. G., K. H. Oh, K. I. Chang, and M. S. Suk, 2004: Intermediate level circulation of the southwestern part of the East/Japan Sea estimated from autonomous isobaric profiling floats. *Geophysical research letters*, **31,** L13213, https://doi.org/10.1029/2004GL020424.

Park, Y. G., J. H. Park, H. J. Lee, H. S. Min, and S. D. Kim, 2013: The effects of geothermal heating on the East/Japan Sea circulation. *J Geophys Res-Oceans*, **118,** 1893-1905, https://doi.org/10.1002/jgrc.20161.

Park, Y. G., A. Choi, Y. H. Kim, H. S. Min, J. H. Hwang, and S. H. Choi, 2010: Direct flows from the Ulleung Basin into the Yamato Basin in the East/Japan Sea. *Deep-Sea Res Pt I*, **57,** 731-738, https://doi.org/10.1016/j.dsr.2010.03.006.

Park, Y. H., and Coauthors, 2019: Observations of the Antarctic Circumpolar Current over the Udintsev Fracture Zone, the narrowest choke point in the Southern Ocean.

Journal of Geophysical Research: Oceans, **124,** 4511-4528, https://doi.org/10.1029/2019JC015024.

Pinardi, N., A. Bonaduce, A. Navarra, S. Dobricic, and P. Oddo, 2014: The mean sea level equation and its application to the Mediterranean Sea. *Journal of Climate*, **27,** 442-447, https://doi.org/doi.org/10.1175/JCLI-D-13-00139.1.

PSMSL, 2020: Permanent Service for Mean Sea Level Tide Gauge Data, Retrieved 20 Jan 2020 from http://www.psmsl.org/data/obtaining/.

Pujol, M. I., P. Schaeffer, Y. Faugère, M. Raynal, G. Dibarboure, and N. Picot, 2018: Gauging the improvement of recent mean sea surface models: a new approach for identifying and quantifying their errors. *Journal of Geophysical Research: Oceans*, **123,** 5889-5911, https://doi.org/10.1029/2017JC013503.

Rio, M., S. Guinehut, and G. Larnicol, 2011: New CNES-CLS09 global mean dynamic topography computed from the combination of GRACE data, altimetry, and in situ measurements. *Journal of Geophysical Research: Oceans*, **116**, https://doi.org/10.1029/2010JC006505.

Senjyu, T., H. R. Shin, J. H. Yoon, Z. Nagano, H. S. An, S. K. Byun, and C. K. Lee, 2005: Deep flow field in the Japan/East Sea as deduced from direct current measurements. *Deep-Sea Res Pt Ii*, **52,** 1726-1741, https://doi.org/10.1016/j.dsr2.2003.10.013.

Seung, Y.-H., and J.-H. Yoon, 1995: Some features of winter convection in the Japan Sea. *Journal of Oceanography*, **51,** 61-73, https://doi.org/10.1007/BF02235936.

Seung, Y. H., 2005: Abyssal currents driven by a local wind forcing through deep mixed layer: implication to the East Sea. *Ocean Science Journal*, **40,** 101, https://doi.org/10.1007/BF03028590.

Speer, K., and E. Tziperman, 1992: Rates of water mass formation in the North Atlantic Ocean. *Journal of Physical Oceanography*, **22,** 93-104, https://doi.org/10.1175/1520-0485(1992)022<0093:ROWMFI>2.0.CO;2.

Stouffer, R. J., and Coauthors, 2006: Investigating the causes of the response of the thermohaline circulation to past and future climate changes. *Journal of Climate*, **19,** 1365-1387, https://doi.org/10.1175/JCLI3689.1.

Taburet, G., and M.-I. Pujol: Sea Level TAC-DUACS products. [Available online at https://resources.marine.copernicus.eu/documents/QUID/CMEMS-SL-QUID-008-032-062.pdf.]

Takematsu, M., Z. Nagano, A. G. Ostrovski, K. Kim, and Y. Volkov, 1999: Direct measurements of deep currents in the northern Japan Sea. *Journal of Oceanography*, **55,** 207-216, https://doi.org/10.1023/A:1007842013257.

Takikawa, T., J. H. Yoon, and K. D. Cho, 2005: The Tsushima warm current through

Tsushima Straits estimated from ferryboat ADCP data. *Journal of Physical Oceanography*, **35,** 1154-1168, https://doi.org/10.1175/Jpo2742.1.

Talley, L., and Coauthors, 2006: Japan/East Sea Water Masses and Their Relation to the Sea's Circulation. *Oceanography* **19,** 32-49, https://doi.org/10.5670/oceanog.2006.42.

Talley, L. D., V. Lobanov, V. Ponomarev, A. Salyuk, P. Tishchenko, I. Zhabin, and S. Riser, 2003: Deep convection and brine rejection in the Japan Sea. *Geophysical Research Letters*, **30**, https://doi.org/10.1029/2002gl016451.

Tanaka, K., 2014: Formation of bottom water and its variability in the northwestern part of the Sea of Japan. *J Geophys Res-Oceans*, **119,** 2081-2094, https://doi.org/10.1002/2013jc009456.

Teague, W., and Coauthors, 2005: Observed deep circulation in the Ulleung Basin. *Deep Sea Research Part II: Topical Studies in Oceanography*, **52,** 1802-1826, https://doi.org/10.1016/j.dsr2.2003.10.014.

Thompson, B., P. Tkalich, and P. Malanotte-Rizzoli, 2017: Regime shift of the South China Sea SST in the late 1990s. *Climate dynamics*, **48,** 1873-1882, https://doi.org/10.1007/s00382-016-3178-4.

Wunsch, C., 2002: What is the thermohaline circulation? *Science*, **298,** 1179-1181, https://doi.org/10.1126/science.1079329.

Yoon, J.-H., K. Abe, T. Ogata, and Y. Wakamatsu, 2005: The effects of wind-stress curl on the Japan/East Sea circulation. *Deep Sea Research Part II: Topical Studies in Oceanography*, **52,** 1827-1844, https://doi.org/10.1016/j.dsr2.2004.03.004.

Yoon, S. T., and Coauthors, 2018: Re-initiation of bottom water formation in the East Sea (Japan Sea) in a warming world. *Sci Rep*, **8,** 1576, https://doi.org/10.1038/s41598-018-19952-4.

Yoshikawa, Y., T. Awaji, and K. Akitomo, 1999: Formation and circulation processes of intermediate water in the Japan Sea. *Journal of Physical Oceanography*, **29,** 1701-1722, https://doi.org/10.1175/1520-0485(1999)029<1701:Facpoi>2.0.Co;2.

Yu, K., H. Liu, Y. Chen, C. Dong, J. Dong, Y. Yan, and D. Wang, 2019: Impacts of the mid-latitude westerlies anomaly on the decadal sea level variability east of China. *Climate Dynamics*, 1-14, https://doi.org/10.1007/s00382-019-04909-8.

Yun, J. Y., L. Magaard, K. Kim, C. W. Shin, C. Kim, and S. K. Byun, 2004: Spatial and temporal variability of the North Korean Cold Water leading to the near-bottom cold water intrusion in Korea Strait. *Progress in Oceanography*, **60,** 99-131, https://doi.org/10.1016/j.pocean.2003.11.004.

Zhang, S., L. Du, H. Wang, and H. Jiang, 2014: Regional sea level variation on interannual timescale in the East China Sea. *International Journal of Geosciences*, **5,** 1405, https://doi.org/10.4236/ijg.2014.512114.

Zuo, J.-c., Q.-q. He, C.-l. Chen, M.-x. Chen, and Q. Xu, 2012: Sea level variability in East China Sea and its response to ENSO. *Water Science and Engineering*, **5,** 164-174, https://doi.org/10.3882/j.issn.1674-2370.2012.02.005.

Abstract (in Korean)

동해 해수면의 경년 및 자오면 순환의 십여 년 변동성을 위성 고도계, 조위, 및 재분석장 자료를 이용하여 분석하였다. 지구 온난화에 의한 해수면 상승의 가속에 의해 동해에 인접한 국가들에게 해수면의 경년 변동은 많은 관심의 대상이 되고 있다. 여름(8월)의 동해는 해수면이 최대치를 나타내고, 많은 태풍에 의해 영향을 받는다. 겨울(11월 및 12월)의 동해는 바람 응력과 해수면의 표준편차가 최대치를 나타낸다. 다른 한편으로, 동해와 같은 반폐쇄성 주변해에서의 자오면 순환은 열, 염, 및 용존 물질의 분포에 필수적인 역할을 하지만, 동해에서 이에 대한 연구는 지금까지 거의 없었다. 따라서, 이 연구의 목적은 해수면의 경년 변동과 함께 동해 자오면 순환을 외부 대기와 내부 해양의 작용을 통해 이해하는 것이다.

26년간(1993년-2018년)의 조위 관측소로부터 구한 월평균 해수면 자료는 여름(8월)에 동해 해수면이 연중 최고치를 보여준다. 26년간(1993년-2018년) 위성자료로부터 구한 여름(8월) 동해의 해수면 상승률은 연평균 해수면 상승률보다 높다. 여름 해수면의 경년 변동은 쿠로시오 확장역과 대만 사이의 대기압 경도력에 의한 에크만 수송의 강약에 의해 좌우된다. 동해 남쪽에서 대기압 경도력이 커질 때, 북북동 방향의 에크만 수송도 커져 동해의 해수면을 높이고, 그 대기압 경도력이 작아지면 에크만 수송도 줄어들어 동해의 해수면을 낮추게 된다. 따라서,

여름의 동해 해수면은 쿠로시오 확장역과 대만 사이의 대기압 차이를 가지고 예측할 수 있다.

동해에서 26년간(1993년-2018년)의 재분석장을 이용해 구한 바람 응력은 겨울철(11월과 12월)에 연중 최고치를 가지고, 겨울철 해수면은 위성자료에서 2016년에는 최대치, 2017년에는 최소치를 나타냈다. 겨울철 동해 해수면은 겨울철 몬순에 의한 에크만 수송에 의한 수평적 해수의 수렴과 발산에 의해 설명된다. 해수면이 높은 해에는 오호츠크해 남단에 강한 북서풍이 불어서 남서쪽으로 흐르는 강한 에크만 수송을 야기하고, 이것이 동해에서 태평양과 오호츠크해로 빠져나오는 해수 수송을 방해하게 된다. 이에 따라, 동해의 해수면이 높아진다. 반대로, 해수면이 낮은 해에는 동해 남부해역에 강한 북서풍이 불고, 이로 인해 남서쪽으로 흐르는 강한 에크만 수송을 야기하고, 이것이 태평양 및 동중국해에서 동해로 유입되는 해수 수송을 방해하게 된다. 따라서, 동해로의 해수 유입이 감소하여 해수면이 낮아진다. 이러한 바람에 의한 에크만 수송의 변화는 대기압 경도에 의해 좌우되기 때문에, 겨울철 동해 해수면은 쏘야해협과 대만 동쪽의 대기압 경도 차이를 이용해서 예측할 수 있다.

20년(1993년-2012년)간 재분석장 자료를 이용해서, 동해 자오면 순환의 강도와 구조를 살펴보고, 이중 순환에서 단일 순환으로 바뀌는 중요한 변화를 찾아냈다. 이 자오면 순환의 변화는 1990년대 후반에서

2000년대로 가면서 중층에서 남향류를 북향류로 바꾸고, 심층에서 북향류를 남향류로 바꾸었다. 동해 자오면 순환이 1990년대 후반에 동해 북서쪽의 차가운 해표면 수온에 의해 얕은 대류(침강)에 의해 이중순환의 형태를 나타내던 것이, 2000년대에 이보다 좀 더 북쪽에서 높은 해표면 염분에 의해 깊은 대류에 의해 단일순환의 형태로 바뀌었다. 이러한 얕은 대류와 깊은 대류는 대기의 부력속(열속과 담수속), 대기의 운동량속에 의한 에크만 수송, 및 해양의 표층 북향류와 서향류 재순환에 의해 좌우된다.

이 연구는 동해 해수면의 경년 변동은 에크만 수송에 의해, 그리고, 동해 자오면 순환의 십여 년 변화는 대기와 해양의 작용에 의해 많은 부분이 설명된다는 것을 보여주었다. 이번에 규명된 현상과 더불어, 작은 대양으로 불리우는 동해에서 해수면의 경년 및 자오면 순환의 십여 년 변화가 기후변화에 따른 대양의 반응을 이해하는데 있어서 많은 단초(실마리)를 제시할 수 있기 때문에, 앞으로도 지속저인 연구가 필요하다.

주요어: 동해, 해수면, 동해 자오면 순환, 에크만 수송, 대기압 경도, 대기해양 상호작용, 경년 변동, 십여 년 변화

Acknowledgement (in Korean)

박사학위 준비하면서 내내 많은 조언과 지도를 아낌없이 해주셨던 지도교수이신 조양기 교수님을 비롯해 논문에 대한 조언과 격려를 아끼지 않았던 남성현 교수님, 나한나 교수님, 강현우 박사님, 박재훈 교수님께 감사드립니다. 박사과정 동안 힘이 되어 준 친구들과 서울대 동료 및 선후배분들께도 감사드립니다.

아버지(韓基協), 어머니(朴貞玉), 누님 가족(惠英, Will, Bill), 여동생 가족(恩英, 우대경, 지용)에게도 감사를 드립니다. 그리고, 미래의 나의 아내와 자녀들도 머지않아 만나길 바랍니다. 세계 평화를 위해 애쓰시는 池田大作 SGI 회장님을 비롯한 한국과 미국 및 전 세계 192개국 SGI 동지들과도 이 기쁨을 나누고 싶고, 전 인류, 생물, 및 무생물에까지 이 논문이 조그마한 도움이 되었으면 합니다.

“또 이는 물결 · 부는 바람 · 만물(萬物)에 대해서 본적(本迹)을 나누고 승렬(勝劣)을 분별(分別)할지니라(御書 869쪽)”에 따라 부는 바람과 이는 물결을 비롯한 해양학, 기상학, 기후학, 및 지구과학이 생물 및 무생물에 끼치는 영향에 관해서 연구하고, 지구 생태계 및 인류 평화에 평생 이바지하도록 노력하겠습니다.

Acknowledgement

I deeply appreciate the advice and guidance given to me by my advisor, Prof. Yang-Ki Cho, while preparing my dissertation. Also, I appreciate the advice and encouragement given from my committee members, Prof. SungHyun Nam, Prof. Hanna Na, Dr. Hyoun-Woo Kang, and Prof. Jae-Hun Park. I would like to thank classmates and junior and senior members of Seoul National University, and my friends.

I greatly appreciate the love and support of my father, mother, older and younger sisters, and their families. Also, I am looking forward to meeting my future wife and children soon. I fully appreciate the effort and devotion of SGI president, Daisaku Ikeda, and SGI members for world peace in 192 countries and territories including Korea and the United States.

According to the passage, “One must distinguish essential and theoretical, superior and inferior, in all things, even the swelling waves and the blowing wind.” (One Hundred and Six Comparisons, 御書全集 (Writings of Nichiren Daishonin) p. 869), I will devote myself to global ecosystems and world peace based on the Lotus Sutra and Nichiren Buddhism. I will investigate the relationship between wave (ocean) and wind (atmosphere), and the effect of them on the living and inanimate beings in Oceanography, Meteorology, Climatology, and Earth Science for the rest of my life.